Influence of Ultrafast Carrier Dynamics on Semiconductor Absorption Spectra

Henni Ouerdane

INFLUENCE OF ULTRAFAST CARRIER DYNAMICS ON SEMICONDUCTOR ABSORPTION SPECTRA

Henni Ouerdane

Submitted for the Degree of
Doctor of Philosophy
at Heriot-Watt University
on completion of research in the
Department of Physics
November 2001.

I hereby declare that the work presented in this thesis was carried out by myself at Heriot-Watt University, Edinburgh, except where due acknowledgement is made, and has not been submitted for any other degree.

Henni Ouerdane (Candidate)

Dr. Ian Galbraith (Supervisor)

Date

I yemma Ouiza,

tameṭṭut ur nelli am tiyiḍ.

Contents

Acknowledgements

It is a great pleasure for me to be at this point of my work when I have the opportunity to acknowledge and thank all the people who helped me, in one way or another, in preparing my PhD thesis during these three years in Edinburgh.

First of all, I wish to thank Dr Ian Galbraith for his excellent supervision during my time at Heriot-Watt University. I have greatly benefited from his thorough knowledge and expertise in semiconductor and computational physics. The countless discussions we have had and the explanations and original ideas he gave me were an invaluable contribution to this PhD thesis. In particular, I am most grateful for his assistance when I was writing the SBE codes. Being French made the work a little bit more challenging for both of us, but Ian always managed to put me at ease which helped overcome the barrier of languages. I have also appreciated his kind support and good advice for matters beyond my PhD work.

Dr Misha Portnoi and Dr Toni Lee's help at the beginning of my PhD is also gratefully acknowledged. Toni's expertise in UNIX and semiconductor physics was very useful in giving me a good start. Misha allowed me to use and modify some of his own computer codes to calculate the 2D excitonic wavefunctions in a screened Coulomb potential. Part of the work in chapter 6 was completed thanks to his help. I thank Mr George Papageorgiou for the guided tour of his lab and for giving me detailed information on the experimental setup as well as the experimental data used in chapter 5. I also thank Dr Chris Dent for proofreading the manuscript of this thesis and making useful suggestions.

Financial assistance through the Departmental Scholarship and additional funding at the end of my PhD for which I thank Dr Ian Galbraith and Professor Brian Wherrett, are gratefully acknowledged.

I also want to thank my fellow PhD student and best friend, Brian Fleming. His solid friendship and support during these three years mean a lot to me. In particular, Brian's ability to fix the numerous wee bugs I had to deal with still impresses me.

My wee brother Djamel always made himself available for patient explanations when I needed to know more about UNIX and Fortran, and when I learned C. Thanks to him, I could quickly cope with the computational part of my work. I wish these two geniuses great success with their own PhDs and all the best.

These past three years, I was extremely busy with my work, but I also managed to enjoy life in Scotland. Very many people contributed to the quality of my life here in Edinburgh. My mate Sean Kudesia taught me enough lingo to cope with everyday Scottish life, very useful to communicate with the lads in the pubs. Members of University staff (secretaries, cleaning ladies, shop assistants and refectory staff) were people with whom I had some of the most interesting and funniest chats. I had great time sharing a flat (and bills!) with my flatmates and friends Bruno Zettor and Sylvain Néelz. I also had the privilege to share a bit of the life of two Scottish families and I want to thank them for all the good things they did for me. Lesley and Iain Maciver always considered me as a member of their family and I had great time in Balerno, appreciating Lesley's delicious cuisine. The Saturday afternoons spent playing with James Ross are a source of great memories for me, and I thank Julie and Kenny Ross for their trust in letting me help them cope with James' autistic condition as much as I could.

There is a lively contingent of foreign postgrads and RAs in the Physics Department, which create a very pleasant atmosphere. In particular, the Mediterranean connection composed of Spanish and Italian folks (David, Andrea, Manuela and Francesco) made me somewhat feel at home when we were speaking about the good things in life: food, olive oil and sun.

On a more personal basis, I would like to thank my fiancée Ioulia for her love, support and all the happiness she brings in my life. I also want to thank my family: my mother Ouiza, my sister Kahina, my brothers Djamel and Hacène, and my aunts Khalti Chabha and Khalti Ghenima for all the good they brought and are still bringing to my life.

Finally, and most importantly, this thesis is dedicated to my mother Ouiza, the

exceptional lady *i yid yessekren.*

Abstract

In this thesis, we present a theoretical description of the many-body effects in semiconductor quantum wells and the role they play in the absorption phenomenon. The optical properties of semiconductors and their connections to the thermodynamic properties of the quasi-2D electron-hole plasma are studied in both nonequilibrium and equilibrium regimes. This work was motivated by a series of pump and probe experiments with spin-selective excitation that were performed at Heriot-Watt. The interpretation of the experimental results is non-trivial given the substantial influence of Coulomb and many-body effects which give rise to a rich variety of broadening and energy renormalizations, and hence places heavy demands on the modeling.

We constructed a simple model to describe the nonequilibrium thermodynamics of the hot electron/hole plasma. We accounted for various dynamical processes such as: relaxation of the carrier distributions, thermalization, plasma cooling, carrier spin-flip, recombination (radiative and nonradiative) and light hole scattering into heavy holes. A full microscopic treatment of the many-body problem being computationally prohibitive, we focused on a phenomenological approach using rate equations and the associated characteristic times for each of the dynamical process included in our analysis. We computed the time dependent energy renormalization and bleaching of the excitonic resonances by solving the semiconductor Bloch equations together with the set of coupled rate equations. We obtained a good qualitative agreement with experiments and further insight into the interplay between the various dynamical processes by varying the phenomenological parameters entering the rate equations. In particular we found that the carrier spin-flip occurs on a relatively long time scale (several tens of picoseconds) compared to the carrier distributions relaxation and thermalization (a picosecond or less). We also could monitor the time evolution of the plasma density, energy, temperature and screening.

In this thesis, we also studied the photoluminescence in II−VI quantum wells at room temperature. We built a mathematical model to account for Coulomb

correlations that are expected to strongly influence the spontaneous emission rate in these materials. We assumed the $1s$ exciton-free electron scattering to be the main process leading an exciton to the photon line before recombination. The excitonic wavefunctions in a 2D screened Coulomb potential were calculated using the variable phase method. The scattering matrix elements computed, we used Fermi's golden rule to evaluate the contribution of the $1s$ exciton-free electron scattering to the spontaneous emission rate. PL spectra at room temperature were calculated for various densities, for wide-gap $ZnSe$ and mid-gap $GaAs$ to compare between II−VI and III−V materials. The $ZnSe$ PL spectra exhibit an exciton resonance below the band edge that is not observed in the case of $GaAs$.

Chapter 1

Introduction

In this thesis, we study the many-body effects in semiconductor quantum wells and the role they play in the absorption phenomenon. A semiconductor quantum well is an artificially grown structure in which the electron motion is confined in one spatial dimension, along the growth direction usually referred to as the z axis, and remains free in the xy plane. For example, it is possible to grow alternatively, on top of each other, layers of $ZnSe$ with layers of $Cd_xZn_{1-x}Se$. In quantum wells, the kinetic energy of the charge carriers is quantized because of the confinement of their motion along the z axis; however, in the xy plane the motion of the carriers being not restricted, their kinetic energy may take continuous values. When excited, an electron leaves the valence band to go into the conduction band. This creates an empty valence-band state referred to as a hole that can be modeled as a quasi-particle with an effective mass, a spin and a momentum. To describe the excited electrons and holes trapped in a semiconductor quantum well, one usually makes use of the quasi-two-dimensional electron/hole plasma model [1]. This plasma may be neutral or not, depending on the excitation conditions achieved by optical pumping or carrier injection.

The electrons and holes interact through the infinite-range Coulomb interaction. A direct consequence is that their motion is correlated. Numerous experimental and theoretical studies have shown that Coulomb correlations between quasi-particles influence the optical response of semiconductors [2, 3, 4]. For instance, excitons that are electron-hole bound states dominate the linear optical properties of semiconductors near the electronic bandgap. Another extremely important property of the carriers is related to their half-integer spin: electrons and holes are Fermions that obey the Pauli exclusion principle. The Fermionic nature of the carriers strongly

influences the electronic, thermodynamic and optical properties of the electron/hole plasma (see chapters 2 and 3). In particular, when electrons are already occupying conduction band states, one cannot observe any optical transition leading a valence band electron to one of these occupied states. One refers to this as phase-space filling.

Modeling the properties of excited semiconductors can be tackled by studying separately the intraband interactions which influence the time evolution of the carrier distributions, and the interband transitions to which the optical properties are mostly related. In order to describe and understand both types of phenomena a many-body treatment of the problem is required. The many-body effects are essentially due to the Coulomb interaction and carrier-phonon scattering. The transport properties connected with the intraband kinetics of electrons and/or holes are due to carrier-carrier interactions within the same band [5]. The consequences of such carrier-carrier interactions are the rapid equilibration (typically less than a picosecond [6]) of the electrons and holes into quasi-equilibrium Fermi-Dirac distributions, and the plasma screening which is the carrier density dependent weakening of the Coulomb interaction potential due to the presence of background charge carriers, i.e. the range of the Coulomb interaction decreases with increasing the carrier density. The spectral properties linked with the interband kinetics are due to the many-body interactions within the electron-hole plasma leading to the renormalization of the energy states. Thus, carrier-carrier scattering and carrier-phonon scattering[1] are the main contributers to the optical dephasing (the decay of the polarization of the medium) and influences both the shape (broadening) and the spectral location (energy shifts) of the absorption and refractive index spectra.

The study of the interplay between the Coulombic forces within the electron-hole plasma and the Fermionic nature of the charge carriers is a long standing problem that is still the object of intensive research (an excellent review paper [7] shows the importance of Coulomb correlations and other many-body interactions in the

[1] At room temperature.

physics of semiconductors). Theoretical and experimental work complement each other to provide information and further insight into the properties of semiconductors. Absorption experiments are often used to study the optical properties of semiconductors. In particular, ultrafast pump and probe experiments are a controllable way of investigating the absorption properties of photoexcited semiconductors (see for instance [6, 8, 9, 10, 11, 12] and references therein). The main idea of the pump and probe beam technique is to excite the sample with an intense and spectrally narrow femtosecond laser beam and to probe changes in the absorption spectra with a weak[2], spectrally broad probe beam. These changes are monitored by comparing the spectra with the absorption spectrum obtained without the presence of the pump pulse (linear absorption spectrum). Pump and probe pulse can be delayed with respect to each other to obtain femtosecond time resolution by measuring the absorption spectra as a function of the time delay. To understand these experiments a mean-field formalism has been developed: the semiconductor Bloch equations (SBE) [11, 13] are particularly appropriate to describe the density and temperature dependence of the light absorption in a semiconductor.

A semiconductor photoexcited by an ultrashort pulse passes through several regimes before it returns to thermodynamic equilibrium. The initial wavevector of the electron and of the hole is the same since the photon momentum is negligible. Thus an initial correlation exists between the electron and the hole. There is also a coherence between the carriers and the radiation field. This coherence is quickly broken by carrier-carrier scattering. The amount of time for the loss of coherence is called the dephasing time. If this time is faster than any other relaxation process, the carrier distribution functions are nonthermal even after the photo-excited states have lost their coherence. The appropriate formulation of the carrier dynamics for the time immediately after the generation of an electron-hole pair, when the photo-excited carrier states are still driven by their mutual coherence and their

[2]A crucial point for the pump and probe technique is the weak intensity of the probe beam: it must be low enough to induce no changes of the optical properties, but it also has to be not too weak to give a reasonable signal-to-noise ratio.

coherence with the electromagnetic field, is based on quantum-mechanical many-body techniques [14, 15, 16].

Coherent effects can be studied using pump-probe spectroscopy with femtoseconds pulses. Indeed, probing the response of a semiconductor with ultrashort laser pulses yields information on processes occuring faster than the fast equilibration time of the excited electron/hole system. In this case, the optical properties of direct-gap semiconductors exhibit some similarities to that of atomic systems. A coherent effect in semiconductors that has been extensively studied is the excitonic optical Stark effect (OSE). The OSE in atoms is a well-known phenomenon [11, 17, 18, 19], but its study in semiconductors has only been done with the possibility of performing ultrafast optical experiments, as the dephasing time in semiconductors is much shorter than in atoms. The OSE process in semiconductors corresponds to a coupling of the energy levels with a below-gap light beam: there is a coherent modification of the energy levels in the electric field of the light field. The light is not absorbed, implying no real creation of quasi-particles in the semiconductor, therefore insuring an ultrafast response time [20]. The effect of the OSE is to shift the exciton absorption line during a laser pulse whose photon energy is below the absorption edge. The OSE in semiconductors has been the object of extensive experimental [21, 22, 23, 24] and theoretical [11, 14, 25, 26, 27, 28] investigations.

Of particular interest are also the effects of high-order correlations on the optical properties of wide-gap semiconductors (WGSC), where Coulomb correlations are important because of the large exciton and biexciton binding energies, comparable to the room temperature thermal energy. For non-resonant (below exciton) excitation a red-shift of the exciton line arising from the influence of virtual transitions to a bound biexcitonic state has been predicted [27, 29] and observed [30, 31]. For a gas initially comprised from a bath of free carriers, no spectral shift of the exciton line is seen [8]. As the carrier motions are increasingly correlated by the Coulomb interaction, creating bound excitons, the exciton resonance energy blueshifts due to exciton-exciton correlations [8]. For resonant excitation, the energy renormal-

izations due to the biexcitons are still unknown: one needs an accurate knowledge of the nature of the interacting electron-hole plasma to describe and explain both the magnitude and sign (blue- or red-shift) of these energy renormalizations. In materials such as $ZnSe/ZnCdSe$ quantum-well, the high exciton binding energy ($\approx$ 35 meV) allows resonant ultrafast optical excitation of excitons with negligible free carrier excitation. Recent experimental results obtained at Heriot-Watt [32] suggest that the interband recombination in WGSC (molecular-beam-epitaxially grown $ZnSe/(Zn,Cd)Se/ZnSe$ multiple quantum well) at 4K is preceded by a phase dominated by biexcitons which induce a finite blue-shift of the exciton resonance. The experimental technique involved measuring the transmission of an extremely stable white-light continuum probe-pulse which was delayed with respect to the 100 fs-long tunable pump pulse. Using circularly-polarized pump pulses resonant with the heavy hole exciton, a spin-polarized exciton population was generated. Measuring the transmission spectrum of an oppositely polarized probe, the biexciton absorption feature was directly detected.

Interpreting the experimental spectra is very difficult since it is non-trivial to estimate both the relative importance of the different contributions once they are clearly identified and the time-scale of the processes. Based on the interpretation one has then to build a model in which assumptions and approximations have at least to lead to results which reflect the qualitative behaviour of the physical quantities of interest. In fact, most of the theoretical treatments neglect the high-order correlations within the electron gas and they are still lagging the experimental results. Nevertheless, as an improved level of the microscopic analysis of the Coulomb-induced many-body correlations is obviously required, efforts have been made to go beyond the time-dependent Hartree-Fock (TDHF) approximation. Indeed, some model studies [33, 34] in one dimension show clearly characteristic signatures of carrier-correlation effects on the excitonic differential absorption spectra. The analysis is done in both coherent [33] and incoherent [34] regimes.

Microscopic calculations including higher-order correlations are very numerically

demanding. Therefore, most of such theoretical investigations were performed in the coherent limit [33, 35, 36]. But, due to dephasing processes occuring after some time when the excited system relaxes, the coherent limit is not valid. Then, both the pair occupations N and the exciton to two-exciton transitions, described by the six-particle correlation Z (involving three electron-hole pairs) [37, 38] have to be taken into account as they have finite values in this case. From an experimental point of view, N can be seen as the result of optical excitation at an earlier time, such that all coherences have decayed before the system is probed. Denoting p the optical interband polarization, one can obtain the coupled differential equation of motion for p and Z from the Heisenberg equation. But, the complete numerical solutions of these equations are currently not feasible in two dimensions and even for the one-dimensional systems one has to restrict oneself to small lattices and simplified Coulomb potential (tight-binding model with no screening).

To obtain further insight into the properties of the electron/hole plasma, it is possible to perform a series of pump-probe experiments introducing a variable delay between the two pulses. In particular, ultrafast nonlinear optical experiments allow one to probe highly nonequilibrium regimes and the possibility of non-degenerate pump and probe and spin-selective excitations makes the technique very powerful: one not only investigates the temperature and density dependence of the absorption spectra in the quasi-equilibrium regime but also tackles the challenging problem of the time evolution of the hot electron-hole plasma taking into account the spin-states of the carriers. Treating the full many-body problem is not feasible as it is computationally prohibitive: as we shall see in the next chapters, the equations involved become extremely complicated very quickly when one builds a rigorous model from first principles, and the singular behaviour of terms such as the Coulomb matrix elements makes the numerical work very challenging (see Chapter 3 and Appendix C).

In this thesis, we are concerned with ultrafast optical experiments. Interesting dynamical effects can arise as a result of coherent processes in the interaction of

the probe pulse with the relaxing electron/hole plasma, producing additional signals that are not a direct result of carrier occupation functions. This complicates significantly the interpretation of experimental results. To avoid this type of complication, we neglect coherent polarization nonlinearities, considering above bandgap pumping and time scales longer than the dephasing time only. Similar work has already been done for $GaAs$ quantum wells at room temperature [39], but here, we account for various dynamical processes which lead the electron/hole plasma to quasi-equilibrium, at low temperature, and we also investigate the light hole exciton dynamics. For an in-depth discussion of the nonequilibrium problem see Ref. [6]. In chapter 4, we build a phenomenological model that includes the relaxation of the carrier distributions, the thermalization of the carriers, the plasma cooling, the carrier spin-flip, the recombination (radiative and nonradiative) and the light hole scattering into heavy holes. Solving a system of coupled rate equations, we monitor the time evolution of the plasma density, energy, temperature and screening. The time scale for the carrier spin-flip process is poorly known, but by comparing the computed exciton peaks dynamics with available experimental data in chapter 5, we aim to extract an order of magnitude. We also explore various possibilities for the phenomenological times to study the interplay between the dynamical processes and their influence on the optical spectra.

The work in this thesis is mostly concerned with the absorption phenomenon. However, in chapter 6, we also investigate the spontaneous emission process in II−VI quantum-wells where the Coulomb interaction is important. The study of narrow semiconductor quantum-wells can be tackled by using a model of the 2D electron-hole plasma [1]. In wide-gap semiconductors at room temperature, the bare exciton binding energy is of the order of k_BT, and the equilibrium in the plasma consists of an almost equal mixture of correlated electron-hole pairs and uncorrelated free carriers. Hence, a significant excitonic contribution in the emission mechanisms is expected as the strong scattering of particles within the plasma plays a crucial role in its properties. More specifically, we study the effect of Coulomb correlations on

the photoluminescence and in particular the $1s$ exciton-free electron scattering. Our model is an extension of the calculations that were presented about twenty years ago in Ref. [40] and were used to calculate the bulk gain spectra from photoluminescence experiments [40, 41].

1.1 Thesis layout

The thesis layout with a brief summary for each chapter is as follows:

- **Chapter 2** We begin this chapter by studying the electronic and thermodynamic properties of the quasi-2D electron/hole plasma. In particular, we address problems arising in realistic systems, considering the finite well-width of the quantum wells and the presence of light holes. The connection to the optical properties is made by introducing the coupling of the electronic system with a radiation field in the electron/hole Hamiltonian. Then, using the Heisenberg equation, we derive a set of equations (SBE) that will be solved in the next chapters.

- **Chapter 3** In this chapter, we are concerned with the numerical solutions of the SBE for quasi-2D electron/hole plasma in quasi-equilibrium. We give a detailed description of the numerical problems we address. We solve the SBE for two types of materials: $GaAs$ and $ZnSe$-based semiconductor quantum wells and compare the numerical results, discussing the interplay between the Coulomb interaction and the Fermionic nature of the carriers which influences the shape of the absorption spectra. We highlight numerical problems that, in particular, occur when solving the SBE with $ZnSe$ parameters in the case of a highly degenerate electron/hole plasma. We also have a preliminary discussion on the limitations of the static plasmon-pole approximation.

- **Chapter 4** To move beyond the quasi-equilibrium situation, we construct a simple model to describe the time evolution of an initially hot electron/hole plasma produced by spin-selective optical pumping in the absorption contin-

uum. We include various dynamical processes which eventually lead to a quasi-equilibrium. A microscopic treatment accounting for these many-body effects is computationally prohibitive. Instead, we use a phenomenological approach to account for the nonequilibrium processes. We obtain the time evolution of the density, energy and temperature for each spin-polarized carrier gas solving a set of coupled rate equations. We also show that we can use the equilibrium formulas to evaluate the plasma screening in the long wavelength limit.

- **Chapter 5** In this chapter, we make use of the results of the previous chapters to compute the absorption spectra for various pump-probe polarization configurations and delays. The numerical results are compared to available experimental data that are also presented. This allows an in-depth discussion of the dynamical processes that influence the time evolution of the electron/hole plasma and hence the dynamics of the absorption spectra. We give an estimate for the time scale of each of these nonequilibrium processes and we also discuss various scenarios obtained by varying the scattering rates to explore further the interplay between the dynamical processes. In particular, we investigate short and long time regimes for the spin-flip, the plasma cooling and the light holes scattering into heavy holes.

- **Chapter 6** In this chapter, we are concerned with the spontaneous emission rate in narrow II−VI quantum wells where the Coulomb interaction remains dominant even at room temperature. A significant excitonic contribution in the emission mechanism is expected. The application of the variable phase method to a 2D screened Coulomb potential permits scattering and bound states to be treated on the same footing, so we use it to obtain the expression of the excitonic wavefunctions in a screened potential. We assume the $1s$ exciton-free electron scattering to be the main process leading an exciton to the photon line before recombination. The exciton-free carrier scattering matrix elements are calculated to evaluate its contribution to the spontaneous emission rate using Fermi's golden rule. In this way, the photoluminescence (PL) spectrum

is obtained by adding the excitonic contribution to the free-carrier plasma spectrum. PL spectra at room temperature are computed for various densities, for two materials: wide-gap $ZnSe$ and mid-gap $GaAs$. The $ZnSe$ PL spectra exhibit an exciton resonance below the band edge that we do not observe in the case of $GaAs$.

- **Chapter 7** We conclude this thesis with a summary of the main results and suggest directions for possible further work.

Mathematical detail omitted in the main text can be found in a series of appendices that are included at the end of this thesis.

We make use of the parabolic band dispersion in the effective mass approximation throughout this thesis. The light hole mass, m_{lh}, is taken to be equal to the electron mass m_e for both $GaAs$ and $ZnSe$. We take the following values for $GaAs$: $m_{lh}^{GaAs} = m_e^{GaAs} = 0.0665\ m_0$, and $m_{hh}^{GaAs} = 0.457\ m_0$. For $ZnSe$, the effective masses are $m_{lh}^{ZnSe} = m_e^{ZnSe} = 0.13\ m_0$, and $m_{hh}^{ZnSe} = 0.57\ m_0$. m_0 is the mass of the free electron. In particular, in chapter 5, we shall use the above values of the effective masses for $ZnSe$ to model the exciton dynamics in $ZnSe/ZnCdSe$ multiple quantum well. The dielectric constants are $\epsilon = 13.7$ for $GaAs$, and $\epsilon = 8.8$ for $ZnSe$. The 3D excitonic Bohr radii are: $a_B^{GaAs} = 125$ Å, and $a_B^{ZnSe} = 39$ Å. The 3D excitonic Rydbergs are $R_y^{GaAs} = 4.2$ meV, and $R_y^{ZnSe} = 21$ meV. The values of $GaAs$ parameters are taken from Ref. [42] and those of $ZnSe$ from Ref. [43]. Unless specified, the S.I. units are used throughout this thesis.

Chapter 2

Microscopic theory of polarization in semiconductor quantum-wells

2.1 Introduction

The microscopic description of the absorption and refractive index spectra requires the knowledge of the polarization P which is the expectation value of the electric dipole moment $e\mathbf{r}$ per unit volume [11]. As we shall see in section 2.3, the derivation of the polarization yields $P = d_{cv} \sum_{\mathbf{k}} p_{\mathbf{k}}$, where $p_{\mathbf{k}}$ is the interband polarization describing the optically-induced coherence between a hole in the valence band v and an electron in the conduction band c, and the dipole matrix element d_{cv}, the strength of the optical transition between the two bands. The theoretical study of the optical dipole transitions in excited semiconductors can be achieved within the framework of the density matrix theory [44]. Because of the collisions and the recombination processes in the electron-hole plasma, it is not possible to have a precise knowledge of the state vector of the system. In other words, electrons and holes in the plasma are not in pure states described by wavefunctions but rather in mixed states best described by a density operator. Moreover, so as to have a realistic analysis of high quality semiconductor samples, the computation of the interband polarization has to take into account the Coulomb interaction in the definition of the Hamiltonian of the electron-hole system: the coupled equations of motion for the carriers distributions $n_{e\mathbf{k}}$ and $n_{h\mathbf{k}}$, and the interband polarization $p_{\mathbf{k}}$ defined as expectation values of products of two particle field operators are derived using the Heisenberg equation and the many-body Hamiltonian.

Details of the calculations can be found later in this chapter, but we can already point out that because of the nature of the problem, solving the Heisenberg

equation is equivalent to solving the many-body Schrödinger equation or an infinite hierarchy of equations of motion for products of an ever increasing number of field operators. This is clearly not a solvable problem if one does not make approximations which consist of a truncation procedure[1]. The simplest situation is when one does the truncation at the lowest level of the hierarchy: only the expectation values of products of two particle field operators are kept. The fourth-order expectation values are factorized into products of two second-order expectation values, using the Random Phase Approximation (RPA) method. The three equations for $p_{\mathbf{k}}$, $n_{e\mathbf{k}}$ and $n_{h\mathbf{k}}$ obtained are called the Hartree-Fock equations [11, 13]. They contain important Coulomb effects such as the bandgap renormalization and the interband Coulomb enhancement that will be discussed later in this chapter. If one wants to go beyond the RPA, the truncation procedure can be applied to the next level of the hierarchy which describes the plasma screening[2] and higher order correlations [44]. Then, the equations for $p_{\mathbf{k}}$, $n_{e\mathbf{k}}$ and $n_{h\mathbf{k}}$ combined with the collision and screening contributions form a set of equation referred to as the semiconductor Bloch equations (SBE) [11, 13, 44].

In this chapter we are mainly concerned with the electronic and thermodynamic properties of the electron-hole plasma and their connection to the optical properties of semiconductor quantum-wells. This chapter aims at introducing the framework in which we shall build our model for the time-dependent absorption spectra in chapter 5. We shall give preliminary results to explain and illustrate the nature of the problems we address and assess the limit of validity of our approximations. It is organised as follows: the object of section 2.2 is to give a brief overview of the properties of the interacting electron gas in a solid. To keep our model as simple as possible, we make use of the jellium model: the discrete lattice structure of the ions in the solid is neglected and the positive charges are treated as a smooth background. The case of the confined electron gas in a semiconductor quantum well is discussed

[1] This is typical of the many-body problem, but not just in quantum mechanics: the classical Liouville equation can be solved using a truncation scheme which leads to the BBGKY hierarchy.

[2] In this case one has to be careful with the inclusion of an *ad hoc* screened Coulomb potential as the plasma screening may be overestimated.

(specific modifications of the Hamiltonian of the 2D interacting electron system and effects of the finite well width on the strength of the Coulombic forces). Section 2.3 is devoted to the derivation of the SBE after having introduced the definition of the interband polarization $p_{\mathbf{k}}$ and the carrier distributions, $n_{e,\mathbf{k}}$ and $n_{h,\mathbf{k}}$, in terms of expectation values of field operator products. Calculations are first presented in the two-band approximation, but the inclusion of the light hole band is also addressed. In this chapter we discuss the properties of the SBE, but we leave the numerical treatment and the discussion of the numerical results to the next chapter.

2.2 Electrons in semiconductor quantum wells

The Hamiltonian of an interacting electron system in a solid is the sum of its kinetic and Coulomb interaction energies (electron-electron and electron-ion). If one neglects the interaction energy part, the system behaves like an ideal Fermi gas whose properties are based on the kinetic energy term only. But, as discussed in the Introduction, one needs to take into account the Coulombic effects so as to study a wealth of phenomena leading to energy shifts and broadening of the semiconductor absorption spectra. Obviously this adds substantially to the complexity of the problem. A convenient way to deal with the difficulty of the calculations is to use the field quantization formalism as a framework. Indeed all the observables of interest polarization, P, density, N... can be expressed in terms of field operators which contain the quantum statistical properties of the particles.

2.2.1 Physics of the 2D interacting electron gas

Hamiltonian of interacting electron system

The electron gas Hamiltonian can be expressed as follows [11]:

$$\mathcal{H}_e = \sum_{\mathbf{k}} \sum_{s} E_{\mathbf{k}} a^{\dagger}_{\mathbf{k},s} a_{\mathbf{k},s} + \frac{1}{2} \sum_{\mathbf{k},\mathbf{k}'} \sum_{\mathbf{q}\neq\vec{0}} \sum_{s,s'} V_q \; a^{\dagger}_{\mathbf{k}+\mathbf{q},s} a^{\dagger}_{\mathbf{k}'-\mathbf{q},s'} a_{\mathbf{k}',s'} a_{\mathbf{k},s} \; . \tag{2.1}$$

The term with $\mathbf{q} = \vec{0}$ vanishes as a consequence of the cancellation between the

attractive interaction energy between the electrons and the ions of the lattice and the negative interaction energy between the electrons and between the ions. The operators $a^{\dagger}_{\mathbf{k},s}$ and $a_{\mathbf{k},s}$ are the creation and annihilation operators for an electron in a state $\mathbf{k}$ with a spin s; the kinetic energy is given by the usual expression: $E_k = \hbar^2 k^2/2m$, and the Coulomb potential energy V_q depends on the dimensionality of the system, even though it always takes the same form in real space[3]:

$$V(r) = \frac{e^2}{4\pi\epsilon r}, \tag{2.2}$$

in MKSA units, ϵ being the dielectric constant. For a three-dimensional system, the Fourier transform of Eq. (2.2) is

$$V_q^{3D} = \frac{e^2}{\epsilon\mathcal{V}}\,\frac{1}{q^2}, \tag{2.3}$$

where $\mathcal{V}$ is the volume of the 3D system. For a two-dimensional system,

$$V_q^{2D} = \frac{e^2}{2\epsilon\mathcal{A}}\,\frac{1}{q}, \tag{2.4}$$

where $\mathcal{A}$ is the area of the 2D system.

A qualitative difference between both potential energies is due to their q dependence, but both exhibit a radial symmetry in the Fourier space. In this thesis, we study light absorption in semiconductor quantum-wells. Hence, attention is focused on 2D systems for which the effective strength of the Coulombic interaction is greater than in 3D because of the confinement of the motion of the electrons.

Based on the Hamiltonian given by Eq. (2.1) one can evaluate the consequences of the Coulombic effects on the energy states of the interacting electron system.

[3]Even for low dimensional systems like semiconductor quantum wells, wires and dots the Coulomb potential behaves like $1/r$ since the electric field lines between two charges are not confined within these structures: they also pass through the surrounding material.

The exchange energy in the Hartree-Fock approximation

At $T = 0$, all particles are in states below the Fermi level: $|\mathbf{k}| \leq k_F$. The ground-state wavefunction can be written as:

$$|0\rangle_{HF} = \prod_{k_i \leq k_F, \sigma_i} a^{\dagger}_{\mathbf{k}_i,\sigma_i}|0\rangle, \tag{2.5}$$

where $|0\rangle$ is the vacuum state and σ_i the spin-states. As the quantities of interest are those which are a direct consequence of the Coulomb interaction, attention is focused on the evaluation of the potential energy only [11]:

$$E^{HF}_{pot} = \frac{1}{2} \sum_{\mathbf{k},\mathbf{k}'} \sum_{\mathbf{q}\neq\vec{0}} \sum_{\sigma,\sigma'} V_q \; {}_{HF}\langle 0|a^{\dagger}_{\mathbf{k}+\mathbf{q},\sigma} a^{\dagger}_{\mathbf{k}'-\mathbf{q},\sigma'} a_{\mathbf{k}',\sigma'} a_{\mathbf{k},\sigma}|0\rangle_{HF} = -\frac{e^2\mathcal{A}^2}{12\pi^2\epsilon} \, \mathcal{C} \, (2\pi N)^{3/2}, \tag{2.6}$$

where

$$\mathcal{C} = \sum_{l=2p} \frac{2}{l+2} \left(\frac{1}{2l} \, C^l_{l/2}\right)^2, \qquad p = 0, 1, 2 \ldots \tag{2.7}$$

is a numerical constant and N is the 2D density: $N = \mathcal{N}/\mathcal{A}$.

Eq. (2.6) shows that the magnitude of the Hartree-Fock potential energy in the electron gas is a monotonically decreasing function of the 2D density N; and, as E^{HF}_{pot} is negative, this quantity represents an energy reduction of the whole interacting electron system which is a consequence of the exchange effects between the electrons. The inclusion of the spin in the definition of the ground state[4] in Eq. (2.5) also leads to a finite contribution to the total energy of the electron system[5] and further enhances the electron-electron repulsion because of the Pauli blocking. One can see this effect by evaluating the correlation function of two electrons in the ground state respectively defined by their position and spin: $(\mathbf{r}, s)$ and $(\mathbf{r}', s')$. This is the conditional probability to find an electron at $\mathbf{r}'$ with a spin s' knowing that there is

[4] As mentionned above, the field operators contain the quantum statistical properties of the particles.

[5] The Pauli principle requires the antisymmetry of the wavefunction of the system. This is the simplest generalization of the Hartree approximation.

an electron at $\mathbf{r}$ with a spin s. It is possible to show that this correlation function depends only on the separation of both electrons $|\mathbf{r}-\mathbf{r}'|$. Precisely, it takes the following form in 2D [11]:

$$F_{\sigma,\sigma'}(\mathbf{r},\mathbf{r}') = \frac{N^2}{4} - N^2\delta_{\sigma,\sigma'} \times \left[\frac{J_1(k_F|\mathbf{r}-\mathbf{r}'|)}{k_F|\mathbf{r}-\mathbf{r}'|}\right]^2 , \tag{2.8}$$

where J_1 is the first order Bessel function of the first kind.

As shown in Fig. 2.1, if the spins σ and σ' are different, the correlation function is a constant; but if the spins σ and σ' are equal, the correlation function is an increasing function of the separation $|\mathbf{r}-\mathbf{r}'|$ which is zero when $\mathbf{r}=\mathbf{r}'$: the mean separation between electrons with equal spins is larger than it is with different spins. In other words, the electrons with equal spins avoid each other as a consequence of the Pauli blocking[6]. Thus, the spin of the electron provokes a further repulsion on top of the Coulombic repulsion, and each electron is surrounded by a finite area (in 2D) which is called the exchange hole. This hole acts as a net positive charge distribution whose attractive interaction with the electron reduces the total energy. This is the origin of the exchange hole energy term: $E_{exc} = E_{pot}^{HF}$.

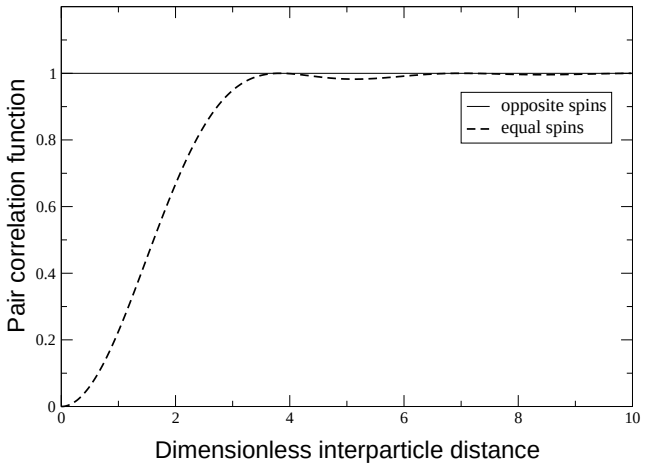

Figure 2.1: Pair correlation function for the two-dimensional electron plasma as a function of the dimensionless interparticle distance $k_F|\mathbf{r}-\mathbf{r}'|$.

The Hartree-Fock theory does not include Coulomb correlations which give rise

[6]This results is also correct for the ideal Fermi gas.

to the screening effect within the electron gas. These correlations lead to the so-called Coulomb hole which, as we shall see later in this chapter, has to be taken into account in the calculations. To treat these Coulomb correlation effects one has to go beyond the Hartree-Fock theory, using for instance the screened Hartree-Fock theory as we shall do.

Screened Coulomb potential

The phenomenon of screening is one of the most important manifestations of the many-body interactions in the electron plasma. The effect of the screening is to reduce the interaction range of the Coulomb potential as the plasma density increases. More specifically, the collective excitations in the electron plasma, also called plasmons, effectively reduce the strength of the Coulomb interaction, by increasing the value of the dielectric function with an increasing plasma density at a given temperature.

Using the RPA and Poisson's equation (see Appendix A), it is possible to show that the screened Coulomb potential seen by a test charge can be expressed as follows:

$$V_q^s = \frac{V_q}{\epsilon_q(\omega)}, \tag{2.9}$$

$\epsilon_q(\omega)$ being the dynamic dielectric function given by the Lindhard formula[7]:

$$\epsilon_q(\omega) = 1 - V_q \sum_{\mathbf{k}} \frac{n_{\mathbf{k}-\mathbf{q}} - n_{\mathbf{k}}}{\hbar(\omega - i\delta + \varepsilon_{k-q} - \varepsilon_k)}, \tag{2.10}$$

where $\hbar\varepsilon_k$ is the kinetic energy of an electron in a state $\mathbf{k}$. The test charge has been assumed to be small enough so as to treat its effect on the plasma as a negligible perturbation; so, the quantity δ appearing in Eq. (2.10) indicates that this perturbation has been switched on adiabatically: the electron plasma was in a homogeneous state and its quasi-thermal equilibrium has always been maintained.

[7] In the electron hole picture, one needs to make explicit both the electron and the hole contributions.

Eq. (2.10) describes the spatial and spectral dispersions of the dielectric function which is a complex and retarded function: the poles are in the lower complex frequency plane. The Lindhard formula is valid both in three and two dimensions (no assumptions on the dimension of the potential have been made) and can describe both equilibrium and nonequilibrium situations[8]. Nevertheless, one needs to make approximations to the Lindhard formula to obtain a simpler treatment of the plasma screening. One of the simplest situation which yields analytical results is when one uses the 2D static screening where $\omega - i\delta \longrightarrow 0$. Then one can modify the Lindhard formula using the static plasmon-pole approximation as shown in Appendix A (see also Refs. [45, 46, 11, 44], so as to obtain:

$$\frac{1}{\epsilon_q} = 1 - \frac{\omega_{pl}^2(q)}{\omega_q^2}. \tag{2.11}$$

The quantities entering Eq. (2.11) are $\omega_{pl}(q)$, the 2D plasma frequency[9]:

$$\omega_{pl}(q) = \sqrt{\frac{e^2 n}{2\epsilon m}\ q} = \sqrt{\frac{8\pi n R_y^2 a_B^3}{\hbar^2}\ q}, \tag{2.12}$$

R_y and a_B being the excitonic Rydberg energy and Bohr radius and ω_q, the 2D effective plasmon frequency given by:

$$\omega_q^2 = \omega_{pl}^2(q)\left(1 + \frac{q}{\kappa}\right) + \nu_q^2. \tag{2.13}$$

In Eq. (2.13) the parameter κ is the 2D screening wavenumber which at equilibrium is given by:

$$\kappa = \frac{me^2}{2\pi\epsilon\hbar^2}\ n_{k=0}\ = \frac{me^2}{2\pi\epsilon\hbar^2}\ \left(1 - e^{-\hbar^2\beta\pi N/m}\right) \tag{2.14}$$

and $\nu_q^2 = C\hbar^2 q^4/16m^2$ is an additional term which simulates the contribution of the pair continuum; C being a numerical constant usually taken between 1 and 4

[8]For a thermal plasma, the particle density operator $n_{\mathbf{k}}$ follows the Fermi-Dirac distribution.

[9]The plasma frequency is the eigenfrequency of the electron plasma density oscillations around the position of the ions in the lattice.

[11, 45]. For our purposes we shall always use the same value: $C = 4$.

As mentioned earlier, the excitations in the electron plasma are responsible for the screening effect. This is reflected in Eqs. (2.9), (2.11), (2.12), (2.13) , and (2.14), showing that the strength of the Coulomb interaction within the electron gas heavily depends on its temperature and density.

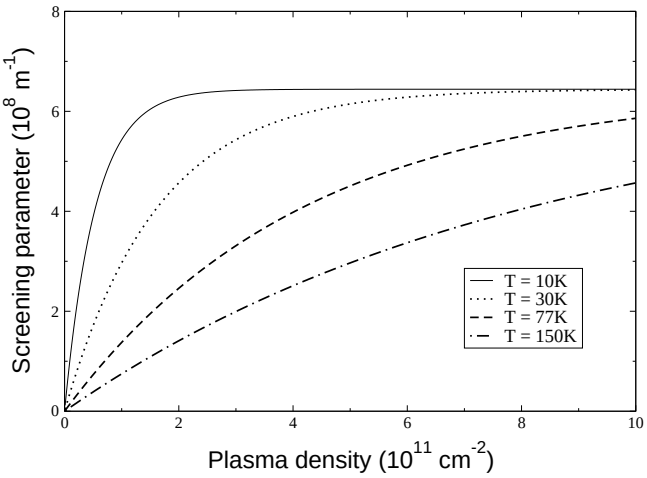

Figure 2.2: Screening parameter κ as function of plasma density, for various plasma temperatures, in a 2D $ZnSe$ electron gas.

For a given temperature, the screening parameter κ, shown in Fig. 2.2 is an increasing function of the density n: the more electrons are present in the plasma, the less effective the Coulomb interaction between two charges is. However, for a given density, increasing the plasma temperature, weakens the screening effect. Considering Eq. (2.14), the interplay between the carrier density and the plasma temperature becomes clearer if one regards the thermal wavelength, $\lambda = 2\pi\hbar^2/mk_BT$, as the relevant physical quantity to discuss the plasma screening, as it gives a measure of the average spatial extent of the wave packets that represent the electrons in the plasma.

The 2D plasma frequency, as shown in Fig. 2.3, is a monotonically increasing function of the wavenumber q. From Eq. (2.12), one can also see the square root dependence of $\omega_{pl}(q)$ on the plasma density. The higher the density, the faster the plasma density oscillates. From Eq. (2.13), one can see that for small values of q,

the 2D effective plasmon frequency and the 2D plasma frequency exhibit a similar behaviour, i.e. a square root dependence on q. But as the wavenumber increases the continuum pair contributions becomes significant and ω_q behaves like q^2. With increasing plasma density N, the parameter κ becomes larger, but that has a small effect on the density dependence of ω_q as it is more influenced by the plasma frequency ω_{pl}.

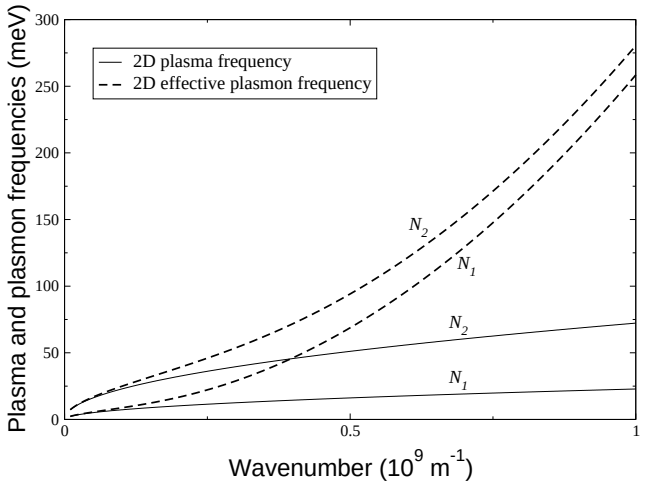

Figure 2.3: Comparison of the 2D plasma frequency and the 2D effective plasmon frequency for two plasma densities, $N_1 = 10^{11}$ cm^{-2} and $N_2 = 10^{12}$ cm^{-2}, in a 2D $ZnSe$ electron gas. The plasma temperature is $T = 77$ K.

2.2.2 Interacting electrons in a semiconductor quantum well

The above analysis of the properties of the electron gas will be helpful in describing those of semiconductor media in the Hartree-Fock approximation. But, as here one needs to take into account the specific band structure of these materials, the Hamiltonian of the interacting electron gas in Eq. (2.1) has to be modified: a band index is introduced and it is assumed that the excitation is achieved by optical pumping. Moreover, the finite well width of the quantum wells has a non-negligible effect on the optical spectra; so, modifications of the Coulomb potential will also be considered by introducing a form factor.

Semiconductor quantum wells

The need to improve the performance of the first semiconductor lasers (homostructure devices) led to the design of semiconductor heterostructures which can be obtained with growth techniques such as molecular beam epitaxy with crystals that have sufficiently similar lattices. The reduced dimensionality leads to a more efficient population inversion of the confined electrons[10] as the allowed electronic energy states and density of states are modified. With such type of structures the threshold current densities are lowered and one can obtain gain at room temperature and lasers operating cw.

As there is no quantum confinement in the xy plane one can define the total electron wavefunction $\psi_{n,\mathbf{k}_{||}}(\mathbf{r})$ as the product of the two-dimensional free particle eigenfunction $\phi_{\mathbf{k}_{||}}(\mathbf{r}_{||})$ and $\zeta_n(z)$, solution of the Schrödinger equation including the confinement potential $V_{conf}(z)$. The vector $\mathbf{r}$ is defined by its transverse component $\mathbf{r}_{||}(x,y)$ and the z component[11], and the function $\phi_{\mathbf{k}_{||}}(\mathbf{r}_{||})$ is given by:

$$\phi_{\mathbf{k}_{||}}(\mathbf{r}_{||}) = \frac{1}{\sqrt{\mathcal{A}}}\, e^{(\pm i\mathbf{k}.\mathbf{r}_{||})}. \tag{2.15}$$

The energy of the in plane motion is simply:

$$E_{xy} = \frac{\hbar^2 \mathbf{k}_{||}^2}{2m_{||}}. \tag{2.16}$$

We obtain then a simple parabolic band structure. With w denoting the quantum well width, one can define the confinement potential as follows:

$$V_{conf}(z) = \begin{cases} 0 & |z| < w/2 \\ V_c & |z| > w/2 \end{cases}. \tag{2.17}$$

In this case the $\zeta_n(z)$ is solution of the Schrödinger equation

[10] But the strength of the Coulomb interaction increases with lower dimensionality and affects the efficiency of the population inversion process.

[11] In the same way one can distinguish between the effective masses $m_{||}$ and m_z.

$$\left[-\hbar^2 \frac{d}{dz}\ \frac{1}{m_z}\ \frac{d}{dz} + V_{conf}(z)\right]\ \zeta_n(z) = E_n \zeta_n(z). \tag{2.18}$$

Expression of the Hamiltonian in the two-band approximation

In general, semiconductors are characterized by a band structure consisting of one conduction band and several valence bands. These bands have asymmetric shapes and sometimes several energy extrema. The simplest model considers just two parabolic bands which most of the time is sufficient to describe some of the basic behaviour of these materials as other completely filled bands do not contribute directly to the optical transitions of interest (visible region). In this chapter, we focuse our attention first on such a two-band model before introducing the degenerate valence band. Furthermore, the following calculations are always based on parabolic band structures which is a good approximation as we consider only optical transitions with frequencies in the visible. These transitions are direct[12] and therefore we only need to consider a small region of the band structure around the bandgap minimum where they are most likely to occur and where the dispersion can be taken as parabolic.

The Hamiltonian of the electron gas in a semiconductor interacting with a radiation field $\vec{\mathcal{E}}(\mathbf{r}, t)$ can be written as follows [11]:

$$\mathcal{H} = \mathcal{H}_e + \mathcal{H}_I \tag{2.19}$$

where

$$\mathcal{H}_e = \sum_{\lambda} \sum_{\mathbf{k}} E_{\lambda,\mathbf{k}} a^{\dagger}_{\lambda,\mathbf{k}} a_{\lambda,\mathbf{k}} + \frac{1}{2} \sum_{\lambda,\lambda'} \sum_{\mathbf{k},\mathbf{k}'} \sum_{\mathbf{q}\neq\vec{0}} V_q\ a^{\dagger}_{\lambda,\mathbf{k}+\mathbf{q}} a^{\dagger}_{\lambda',\mathbf{k}'-\mathbf{q}} a_{\lambda',\mathbf{k}'} a_{\lambda,\mathbf{k}} \tag{2.20}$$

describes the dynamics of the electrons within the semiconductor, and

[12]The photon momentum is so small compared to the electron momenta involved in the optical transition that its value does not affect significantly the momentum conservation requirement.

$$\mathcal{H}_I = -\sum_{\lambda,\lambda'}\sum_{\mathbf{k}} \mathcal{E}(t)\left(d_{\lambda\lambda',\mathbf{k}}\; a^{\dagger}_{\lambda,\mathbf{k}} a_{\lambda',\mathbf{k}} + h.c.\right) \tag{2.21}$$

describes the interband dipole coupling to the light field $\vec{\mathcal{E}}(\mathbf{r},t)$, $d_{\lambda\lambda',\mathbf{k}}$ being the projection of the dipole moment $\mathbf{d}_{\lambda\lambda',\mathbf{k}}$ in the field direction $\vec{\mathcal{E}}/\mathcal{E}$, and $h.c.$ the Hermitian conjugate. The wavevector $\mathbf{k}$ contains the spin index: $(\mathbf{k},\sigma) \equiv \mathbf{k}$, unless otherwise stated. Apart from the inclusion of the interaction with the light field $\vec{\mathcal{E}}(\mathbf{r},t)$, the main difference with the expression of the Hamiltonian given in Eq. (2.1) is the presence of the band index λ.

In the two-band approximation one deals with one conduction band $\lambda = c$ and one valence band $\lambda' = v$. These bands are taken as parabolic so $d_{\lambda\lambda',\mathbf{k}}$ does not depend on the wavevector $\mathbf{k}$. Thus, Eqs. (2.20) and (2.21) become:

$$\mathcal{H}_e = \sum_{\mathbf{k}} \left(E_{c,\mathbf{k}} a^{\dagger}_{c,\mathbf{k}} a_{c,\mathbf{k}} + E_{v,\mathbf{k}} a^{\dagger}_{v,\mathbf{k}} a_{v,\mathbf{k}}\right)$$

$$+\frac{1}{2}\sum_{\mathbf{k},\mathbf{k}'}\sum_{\mathbf{q}\neq\vec{0}} V_q \left(a^{\dagger}_{c,\mathbf{k}+\mathbf{q}} a^{\dagger}_{c,\mathbf{k}'-\mathbf{q}} a_{c,\mathbf{k}'} a_{c,\mathbf{k}} + a^{\dagger}_{v,\mathbf{k}+\mathbf{q}} a^{\dagger}_{v,\mathbf{k}'-\mathbf{q}} a_{v,\mathbf{k}'} a_{v,\mathbf{k}} + 2a^{\dagger}_{c,\mathbf{k}+\mathbf{q}} a^{\dagger}_{v,\mathbf{k}'-\mathbf{q}} a_{v,\mathbf{k}'} a_{c,\mathbf{k}}\right)$$

$$-\sum_{\mathbf{k}} \mathcal{E}(t)\left(d_{cv}\; a^{\dagger}_{c,\mathbf{k}} a_{v,\mathbf{k}} + h.c.\right) \tag{2.22}$$

Denoting E_g the unrenormalized bandgap (absence of excited electrons), the conduction and valence band energies are given by:

$$E_{c,k} = \hbar\epsilon_{c,k} = E_g + \hbar^2 k^2/2m_c, \tag{2.23}$$

and

$$E_{v,k} = \hbar\epsilon_{v,k} = \hbar^2 k^2/2m_v, \tag{2.24}$$

using the single particle energies in the effective mass approximation. The effective masses are defined by the reciprocal of the band curvatures:

$$\frac{1}{m_i} = \frac{1}{\hbar^2} \left. \frac{d^2 E_{i,k}}{dk^2} \right|_{k=0}, \qquad i = c, v. \tag{2.25}$$

The valence band having a negative dispersion, the effective mass as defined in Eq. (2.25) is negative.

Effects of a finite well width

As mentioned earlier, the attention is mainly focused on 2D systems. However, real quantum wells have a finite width w and one has to deal with quasi-2D systems which still do not behave like 3D systems. It has been seen earlier that the dimensionality of the interacting electron gas has an effect on the strength of the Coulomb interaction: the confinement of the motion of the electron gas to a 2D space makes the Coulomb interaction stronger. The form factor f_q characterizes the well-width-dependent deviations from the ideal 2D systems of V_q^{2D} [44]:

$$V_q = f_q \, \frac{e^2}{2\epsilon \mathcal{A}} \, \frac{1}{q}. \tag{2.26}$$

The definition of the form factor f_q and the calculations detailed in Appendix B give:

$$f_q = \frac{2}{w} \left[\frac{1}{q} + \frac{1}{2} \, \frac{qw^2}{q^2 w^2 + 4n^2\pi^2} + (e^{-qw} - 1) \frac{1}{w} \left(\frac{1}{q} - \frac{qw^2}{q^2 w^2 + 4n^2\pi^2} \right)^2 \right]. \tag{2.27}$$

The form factor f_q is a finite, positive and monotonically decreasing function of q. For $q = 0$ $f_q = 1$, and $\lim_{w \to 0} f_q = 1$, which means that there is no alteration of the 2D potential for a zero well width: one deals with the ideal 2D system.

With increasing the plasma density at a given temperature, the screening effect becomes important and we saw how we can quantify this effect in the section 2.1.3. But, at this stage, we did not deal with the more realistic situation of a finite well width. In the case of a screened Coulomb potential in a quasi-2D system, one has to alter the expression of the 2D plasma frequency and the 2D effective plasmon

frequency in Eqs. (2.12) and (2.13) so as to take into account the effect of the finite well width on the dielectric function, Eq. (2.11).

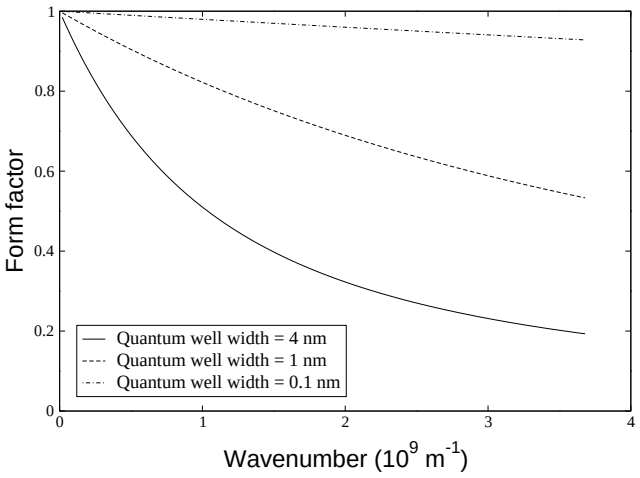

Figure 2.4: Form factor as a function of the wavenumber q for various well widths.

Using the calculations detailed in Appendix A together with the above definition of the Coulomb potential in a quantum-well, Eq. (2.26), yields:

$$\omega_{pl}(q) = \sqrt{\frac{e^2 n}{2\epsilon m}\ f_q\ q}, \tag{2.28}$$

for the quasi-2D plasma frequency, and

$$\omega_q^2 = \omega_{pl}^2(q)\left(1 + \frac{q}{f_q\ \kappa}\right) + \nu_q^2, \tag{2.29}$$

for the quasi-2D effective plasmon frequency. The screening parameter κ is defined by Eq. (2.14).

With a finite well width the electrons are not strictly confined in an ideal 2D space. A direct effect is that the plasma density oscillations are slowed down for a given density. In other words, the 2D plasma frequency decreases with increasing the well width, which is coherent with Eq. (2.28) and the definition of the form factor.

The screened Coulomb potential in a quantum-well is given by:

$$V_q^s = f_q V_q^{2D} \left(1 - \frac{\omega_{pl}^2(q)}{\omega_q^2}\right), \tag{2.30}$$

in the static plasmon-pole approximation, with the quasi-2D plasma and effective plasmon frequencies defined as in Eqs. (2.28) and (2.29).

Quasi-Fermi levels in a semiconductor quantum well

When electrons in a semiconductor are excited, the fast carrier-carrier scattering drives the electron and hole nonthermal distributions into Fermi-Dirac distributions. As already briefly discussed in the Introduction this scattering mostly involves intraband interactions. So, the equilibrium is only established within the bands and not amongst them: one does not deal with a proper thermodynamic equilibrium. Indeed, even if the time scale for quasi-equilibration is much longer than the intraband carrier-carrier scattering time, it typically remains much shorter than the interband relaxation time. Nevertheless, one can define Fermi-Dirac distributions for each band characterized by a quasi-Fermi level, or chemical potential, μ. Obviously, as long as the electron system as a whole has not reached the thermodynamic equilibrium, these quasi-Fermi levels, evaluated with the same temperature and carrier density provided that the semiconductor is not doped, are not equal.

The Fermi-Dirac distribution is given by:

$$f_{\mathbf{k}} = \frac{1}{e^{\beta\ (E_k - \mu)} + 1}, \tag{2.31}$$

where E_k is the energy in the state $\mathbf{k}$, and μ the chemical potential of the system. The total number of carriers, given by:

$$\mathcal{N} = \sum_{\mathbf{k},\sigma} f_k, \tag{2.32}$$

determines the chemical potential at a given temperature T. To evaluate the above expression we approximate the discrete sum by an integral. This requires the knowl-

edge of the free-particle density of states[13], $D(E)$. For quasi-2D systems like semiconductor quantum wells one can assume that taking the ideal 2D density of states is a good approximation, so Eq. (2.32) becomes:

$$N = \frac{\mathcal{N}}{\mathcal{A}} = \frac{1}{2\pi}\left(\frac{2m}{\hbar^2\beta}\right) \int_0^\infty dE \; \frac{1}{e^{\beta(E-\mu)}+1}, \tag{2.33}$$

After the evaluation of the integral in Eq. (2.33) one finds the expression of the 2D Fermion chemical potential as a function of the 2D carrier density N and the temperature T:

$$\mu(N,T) = \frac{1}{\beta} \; \ln\left(e^{\hbar^2\beta\pi N/m} - 1\right). \tag{2.34}$$

This will be taken as the expression of the electron and heavy hole quasi-Fermi levels μ_e and μ_{hh} whose values also depend on the effective mass of the carrier m_e and m_{hh}.

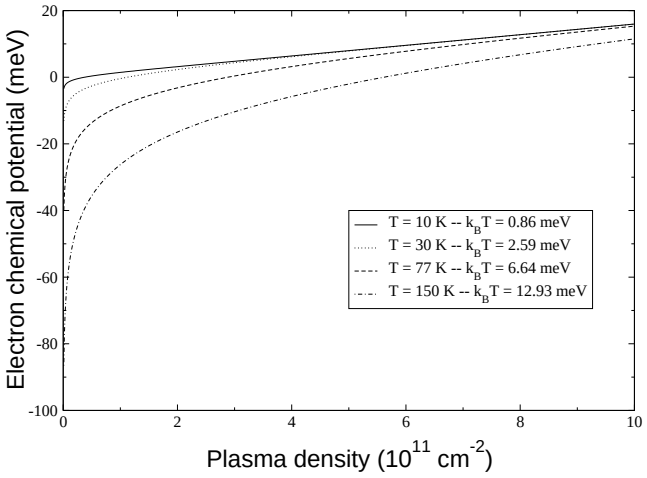

Figure 2.5: Electron chemical potential as a function of plasma density for various temperatures.

The electron and heavy hole chemical potentials are an increasing function of the plasma density (see Fig. 2.5 for the electron chemical potential), but for a given density the higher the temperature is the lower the chemical potentials are. For a

[13]Even though we deal with an interacting electron gas, we assume that the free-carrier approximation is good enough to calculate the quasi-equilibrium chemical potential.

given density and temperature, the heavy hole chemical potential is smaller than the electron chemical potential as $m_{hh} > m_e$. In the nondegenerate limit, i.e. low density and high temperature, the chemical potential diverges towards $-\infty$.

2.3 The Semiconductor Bloch Equations

In very low excitation regimes, the Coulomb attraction between the conduction band electrons and the valence band holes is very important; however, no interactions between different electron-hole pairs have to be considered as the plasma density is low. But when the excitations become important, one has to deal with finite densities of carriers which are coupled dynamically to the interband polarization. The SBE give a realistic description of this coupling.

2.3.1 Hamiltonian equations

Definition of the interband polarization

The polarization $\mathbf{P}(t)$ is defined as the expectation value of the electric dipole $e\mathbf{r}$ [11]:

$$\mathbf{P}(t) = \sum_{\sigma} \int d^3\mathbf{r} \; \langle \hat{\psi}^{\dagger}_{\sigma}(\mathbf{r},t) \; e\mathbf{r} \; \hat{\psi}_{\sigma}(\mathbf{r},t) \rangle = \sum_{\sigma} \int d^3\mathbf{r} \; \mathrm{Tr} \left(\rho_0 \hat{\psi}^{\dagger}_{\sigma}(\mathbf{r},t) \; e\mathbf{r} \; \hat{\psi}_{\sigma}(\mathbf{r},t) \right). \tag{2.35}$$

In Eq. (2.35):

- ρ_0 is the density operator describing the system at the initial time before the field was switched on.
- $\hat{\psi}_{\sigma}(\mathbf{r},t)$ is the electron field operator defined as:

$$\hat{\psi}_{\sigma}(\mathbf{r},t) = \sum_{\lambda} \sum_{\mathbf{k}} \; a_{\lambda,\mathbf{k},\sigma}(t) \; \phi_{\lambda,\mathbf{k},\sigma}(\mathbf{r}), \tag{2.36}$$

where $\phi_{\lambda,\mathbf{k},\sigma}(\mathbf{r})$ is the single-particle eigenfunction for an electron in the semiconductor in the state specified by the band index λ, the momentum $\mathbf{k}$ and the spin

σ. In the case of spatially homogeneous system the eigenfunctions $\phi_{\lambda,\mathbf{k},\sigma}(\mathbf{r})$ are the Bloch functions as one is dealing with delocalized electrons. The operator $a_{\lambda,\mathbf{k},\sigma}(t)$ is the annihilation operator for the electron in that state. The notation $\langle\hat{\mathcal{O}}\rangle$ stands for the expectation value of the operator $\hat{\mathcal{O}}$ calculated as:

$$\langle\hat{\mathcal{O}}\rangle = \text{Tr } \left(\rho_0\hat{\mathcal{O}}\right). \tag{2.37}$$

Inserting Eq. (2.36) into Eq. (2.35) yields:

$$\mathbf{P}(t) = \sum_{\sigma}\sum_{\lambda,\lambda'}\sum_{\mathbf{k},\mathbf{k}'} \langle a^{\dagger}_{\lambda,\mathbf{k},\sigma}(t)\ a_{\lambda',\mathbf{k}',\sigma}(t)\rangle \int d^3\mathbf{r}\ \phi^{\dagger}_{\lambda,\mathbf{k},\sigma}(\mathbf{r})\ e\mathbf{r}\ \phi_{\lambda',\mathbf{k}',\sigma}(\mathbf{r}). \tag{2.38}$$

And writing the dipole matrix elements as:

$$\int d^3\mathbf{r}\ \phi^{\dagger}_{\lambda,\mathbf{k},\sigma}(\mathbf{r})\ e\mathbf{r}\ \phi_{\lambda',\mathbf{k}',\sigma}(\mathbf{r}) = \delta_{\mathbf{k}\mathbf{k}'}\ \mathbf{d}_{\lambda\lambda'}, \tag{2.39}$$

with $\lambda \neq \lambda'$, yields:

$$\mathbf{P}(t) = \sum_{\sigma}\sum_{\lambda,\lambda'}\sum_{\mathbf{k}} \langle a^{\dagger}_{\lambda,\mathbf{k},\sigma}(t)\ a_{\lambda',\mathbf{k},\sigma}(t)\rangle\ \mathbf{d}_{\lambda,\lambda'} = \sum_{\sigma}\sum_{\lambda,\lambda'}\sum_{\mathbf{k}} P_{\lambda\lambda',\mathbf{k},\sigma}(t)\ \mathbf{d}_{\lambda,\lambda'}. \tag{2.40}$$

This defines the interband polarization as:

$$P_{\lambda\lambda',\mathbf{k},\sigma}(t) = \langle a^{\dagger}_{\lambda,\mathbf{k},\sigma}(t)\ a_{\lambda',\mathbf{k},\sigma}(t)\rangle. \tag{2.41}$$

The function $P_{\lambda\lambda'}$ as defined in Eq. (2.41) would be zero in an equilibrium system without a permanent dipole moment. However, the presence of the light field induces optical transitions between the bands; therefore, the interband polarization $P_{\lambda\lambda'}$ in such an externally driven system is finite.

Hamiltonian in the electron-hole representation

Another possible representation of the problem is the electron-hole picture which is equivalent to the previous one provided that one defines the field operators for the electrons and the holes as follows [11, 44]:

$$\begin{cases} \beta^{\dagger}_{-\mathbf{k}} = a_{v,\mathbf{k}} \\ \alpha^{\dagger}_{\mathbf{k}} = a^{\dagger}_{c,\mathbf{k}} \end{cases} \tag{2.42}$$

Inserting the operators defined in Eq. (2.42) into Eq. (2.22) leads to the following expression for the Hamiltonian of the electron-hole gas interacting with a light field in the two-band approximation:

$$\mathcal{H} = \sum_{\mathbf{k}} \left(E_{e,k} \alpha^{\dagger}_{\mathbf{k}} \alpha_{\mathbf{k}} + E_{h,k} \beta^{\dagger}_{-\mathbf{k}} \beta_{-\mathbf{k}} \right)$$

$$+ \frac{1}{2} \sum_{\mathbf{k},\mathbf{k}'} \sum_{\mathbf{q} \neq \vec{0}} V_q \left(\alpha^{\dagger}_{\mathbf{k}+\mathbf{q}} \alpha^{\dagger}_{\mathbf{k}'-\mathbf{q}} \alpha_{\mathbf{k}'} \alpha_{\mathbf{k}} + \beta^{\dagger}_{\mathbf{k}+\mathbf{q}} \beta^{\dagger}_{\mathbf{k}'-\mathbf{q}} \beta_{\mathbf{k}'} \beta_{\mathbf{k}} - 2 \alpha^{\dagger}_{\mathbf{k}+\mathbf{q}} \beta^{\dagger}_{\mathbf{k}'-\mathbf{q}} \beta_{\mathbf{k}'} \alpha_{\mathbf{k}} \right)$$

$$- \sum_{\mathbf{k}} \mathcal{E}(t) \left(d_{cv} \; \alpha^{\dagger}_{\mathbf{k}} \beta^{\dagger}_{\mathbf{k}} + h.c \right), \tag{2.43}$$

after restoring the normal ordering of the field operators using the anti-commutation rules and leaving out the constant terms.

In the electron-hole representation, the single particle energies given by Eqs. (2.23) and (2.24), become:

$$E_{e,k} = E_{c,k} = \hbar \epsilon_{e,k} \tag{2.44}$$

which remains unchanged, and:

$$E_{h,k} = -E_{v,k} + \sum_{\mathbf{q} \neq \vec{0}} V_q = \hbar \epsilon_{h,k} \tag{2.45}$$

which shows that the kinetic energy of the holes includes the Coulomb energy of the full valence band; or, in other words: the hole energy is the energy of the completely filled valence band minus the energy of the valence band with a vacant electronic

state. Eq. (2.45) shows a positive dispersion of the hole energy whereas Eq. (2.24) gives a negative dispersion for the valence band electrons: the effective hole mass m_h and the effective valence band electron mass m_v have opposite signs. Therefore, the effective electron mass m_e simply equals the effective conduction band electron mass m_c and the hole effective mass, m_h, is exactly the opposite of the valence band electron effective mass, m_v. Note that the heavy hole dispersion in Eq. (2.45) takes the Coulomb interaction amongst the carriers into account and changes sign, but conserves the same curvature.

Derivation of the SBE

The quantities of interest are the electron distribution $n_{e,\mathbf{k}}(t)$, the hole distribution $n_{h,\mathbf{k}}(t)$ and the interband polarization $p_{\mathbf{k}}(t)$ defined as:

$$\begin{cases} n_{e,\mathbf{k}}(t) = \langle \alpha^{\dagger}_{\mathbf{k}} \alpha_{\mathbf{k}} \rangle \\ n_{h,\mathbf{k}}(t) = \langle \beta^{\dagger}_{-\mathbf{k}} \beta_{-\mathbf{k}} \rangle \\ p_{\mathbf{k}}(t) = \langle \beta_{-\mathbf{k}} \alpha_{\mathbf{k}} \rangle \end{cases} \tag{2.46}$$

Based on these definitions and the Hamiltonian given by Eq. (2.43) we can derive the equation of motion for $n_{e,\mathbf{k}}(t)$, $n_{h,\mathbf{k}}(t)$ and $p_{\mathbf{k}}(t)$, using the Heisenberg equation of motion:

$$i\hbar \frac{\partial}{\partial t}\, \hat{\mathcal{O}}(t) = [\hat{\mathcal{O}}(t), \mathcal{H}] \tag{2.47}$$

for any operator $\hat{\mathcal{O}}(t)$ in the Heisenberg picture. Inserting the 2-operator products given in Eqs. (2.46) into Eq. (2.47), performing lengthy calculations involving the normal ordering of the Fermion operators, and taking the average defined as in Eq. (2.37) together with the definitions given in Eqs.(2.46) yields:

$$\begin{aligned} \hbar \left[i\frac{\partial}{\partial t} - (\epsilon_{e,k} + \epsilon_{h,k}) \right] p_{\mathbf{k}} &= (n_{e,\mathbf{k}} + n_{h,\mathbf{k}} - 1)\; d_{cv}\; \mathcal{E}(t) \\ &+ \sum_{\mathbf{k}'} \sum_{\mathbf{q} \neq \vec{0}} V_q \Big(\langle \alpha^{\dagger}_{\mathbf{k}'-\mathbf{q}} \beta_{-\mathbf{k}-\mathbf{q}} \alpha_{\mathbf{k}'} \alpha_{\mathbf{k}} \rangle + \langle \beta_{\mathbf{k}'+\mathbf{q}} \beta_{-\mathbf{k}-\mathbf{q}} \beta^{\dagger}_{\mathbf{k}'} \alpha_{\mathbf{k}} \rangle \\ &\qquad + \langle \beta_{\mathbf{k}'} \alpha^{\dagger}_{\mathbf{k}'-\mathbf{q}} \alpha_{\mathbf{k}'} \alpha_{\mathbf{k}-\mathbf{q}} \rangle + \langle \beta_{-\mathbf{k}} \beta_{\mathbf{k}'-\mathbf{q}} \beta^{\dagger}_{\mathbf{k}'} \alpha_{\mathbf{k}+\mathbf{q}} \rangle \Big) , \end{aligned} \tag{2.48}$$

$$\hbar\frac{\partial}{\partial t}\, n_{e,\mathbf{k}} = -2\ \mathrm{Im}\ (d_{cv}\ \mathcal{E}(t)\ p^*_{\mathbf{k}}) + \ i\ \sum_{\mathbf{k}'}\sum_{\mathbf{q}\neq\vec{0}}\ V_q\ \Big(\langle\alpha^\dagger_{\mathbf{k}}\alpha^\dagger_{\mathbf{k}'-\mathbf{q}}\alpha_{\mathbf{k}-\mathbf{q}}\alpha_{\mathbf{k}'}\rangle - \langle\alpha^\dagger_{\mathbf{k}+\mathbf{q}}\alpha^\dagger_{\mathbf{k}'-\mathbf{q}}\alpha_{\mathbf{k}}\alpha_{\mathbf{k}'}\rangle + \langle\alpha^\dagger_{\mathbf{k}}\alpha_{\mathbf{k}-\mathbf{q}}\beta^\dagger_{\mathbf{k}'-\mathbf{q}}\beta_{\mathbf{k}'}\rangle - \langle\alpha^\dagger_{\mathbf{k}+\mathbf{q}}\alpha_{\mathbf{k}}\beta^\dagger_{\mathbf{k}'-\mathbf{q}}\beta_{\mathbf{k}'}\rangle\Big)\,, \tag{2.49}$$

and

$$\hbar\frac{\partial}{\partial t}\, n_{h,\mathbf{k}} = -2\ \mathrm{Im}\ (d_{cv}\ \mathcal{E}(t)\ p^*_{\mathbf{k}}) + \ i\ \sum_{\mathbf{k}'}\sum_{\mathbf{q}\neq\vec{0}}\ V_q\ \Big(\langle\beta^\dagger_{-\mathbf{k}}\beta^\dagger_{\mathbf{k}'-\mathbf{q}}\beta_{-\mathbf{k}-\mathbf{q}}\beta_{\mathbf{k}'}\rangle - \langle\beta^\dagger_{-\mathbf{k}+\mathbf{q}}\beta^\dagger_{\mathbf{k}'-\mathbf{q}}\beta_{-\mathbf{k}}\beta_{\mathbf{k}'}\rangle + \langle\alpha^\dagger_{\mathbf{k}'+\mathbf{q}}\alpha_{\mathbf{k}'}\beta^\dagger_{-\mathbf{k}}\beta_{-\mathbf{k}+\mathbf{q}}\rangle - \langle\alpha^\dagger_{\mathbf{k}'+\mathbf{q}}\alpha_{\mathbf{k}'}\beta^\dagger_{-\mathbf{k}-\mathbf{q}}\beta_{-\mathbf{k}}\rangle\Big)\,. \tag{2.50}$$

These equations are essentially exact but the knowledge of the time evolution of the four-operator products is required in order to solve them. These terms appear as a direct consequence of the many-body Coulomb interaction in the Hamiltonian in Eq. (2.43). Indeed if one neglects it, the equations (2.48), (2.49) and (2.50) are reduced to the optical Bloch equations for free carrier transitions [17, 19]. At this step of the calculations, the polarization equation, Eq. (2.48), already exhibits another important many-body effect: the phase-space filling due to the Pauli blocking factor $(n_{e,\mathbf{k}} + n_{h,\mathbf{k}} - 1)$ which reduces the oscillator strength as the plasma density increases. To proceed with our calculations, we need to address the problem raised by the four-operator products. If we want to evaluate the time evolution of the four-operator products it turns out that six-operator products appear in the calculations, and so on indefinitely: eventually, one has to deal with an infinite hierarchy of coupled differential equations containing expectation values of products of higher and higher number of field operators. As already briefly discussed in the Introduction, one cannot solve these coupled differential equations exactly and needs to make approximations. The simplest approximation consists of the RPA scheme: one

splits the four-operator terms into products of densities and interband polarizations. By neglecting some of the higher order correlations in the system but retaining the coupling between the density and polarization, we can for instance factorize the products of four operators $\langle \alpha^{\dagger}_{\mathbf{k'-q}} \beta_{\mathbf{-k-q}} \alpha_{\mathbf{k'}} \alpha_{\mathbf{k}} \rangle$ (appearing in Eq. (2.48)) into one which is a product of the distribution $n_{e,\mathbf{k}}$ and the interband polarization $p_{\mathbf{k+q}}$ only:

$$\langle \alpha^{\dagger}_{\mathbf{k'-q}} \beta_{\mathbf{-k-q}} \alpha_{\mathbf{k'}} \alpha_{\mathbf{k}} \rangle = \langle \alpha^{\dagger}_{\mathbf{k'-q}} \alpha_{\mathbf{k}} \rangle \langle \beta_{\mathbf{-k-q}} \alpha_{\mathbf{k'}} \rangle \delta_{\mathbf{k'-q,k}} \tag{2.51}$$

The sum over $\mathbf{k'}$ in Eq. (2.48) yields the following term: $p_{\mathbf{k+q}} n_{e,\mathbf{k}}$, according to the definitions of $n_{e,\mathbf{k}}$ and $p_{\mathbf{k}}$ given in Eq. (2.46).

Thus, using the RPA yields the Hartree-Fock equations [11, 13, 44]:

$$\frac{\partial}{\partial t}\, p_{\mathbf{k}}(t) = -i(e_{e,k} + e_{h,k})\; p_{\mathbf{k}}(t) - i(n_{e,\mathbf{k}}(t) + n_{h,\mathbf{k}}(t) - 1)\; \omega_{R,\mathbf{k}}(t), \tag{2.52}$$

$$\hbar \frac{\partial}{\partial t}\, n_{e,\mathbf{k}}(t) = -2 \text{ Im } (\omega_{R,\mathbf{k}}(t)\; p^{*}_{\mathbf{k}}(t)), \tag{2.53}$$

and

$$\hbar \frac{\partial}{\partial t}\, n_{h,\mathbf{k}}(t) = -2 \text{ Im } (\omega_{R,\mathbf{k}}(t)\; p^{*}_{\mathbf{k}}(t)), \tag{2.54}$$

where

$$\hbar \omega_{R,\mathbf{k}}(t) = d_{cv}\; \mathcal{E}(t) + \sum_{\mathbf{q} \neq \mathbf{k}} V_{|\mathbf{k-q}|}\; p_{\mathbf{q}}(t) \tag{2.55}$$

defines the generalized Rabi frequency $\omega_{R,\mathbf{k}}$ which appears in the three equations (2.52), (2.53) and (2.54).

The finite carrier density in the plasma leads to a further renormalization of the single-particle energies[14] because of the finite exchange term $\Sigma_{exc}(k)$ [42]:

[14]Or shrinkage of the bandgap: the transition energy between the valence band and the conduction band decreases with increasing the plasma density.

$$\hbar e_{i,k} = \hbar\epsilon_{i,k} + \Sigma_{exc,i}(k) = \hbar\epsilon_{i,k} - \sum_{\mathbf{q}\neq\mathbf{k}} V_{|\mathbf{k}-\mathbf{q}|} n_{i,q}, \qquad i = e, h \tag{2.56}$$

and to the phase space filling effect because of the population inversion described by the factor $1 - n_e - n_h$. Note that if we have different spin populations, the exchange term is spin-dependent. In such conditions, the bandgap shrinkage also depends on the spin populations[15]. Thus, qualitative effects such as energy shifts and bleaching of the peaks in the absorption spectra can be explained at the Hartree-Fock level. Unlike the optical Bloch equations, the Hartree-Fock equations are not diagonal in the momentum index $\mathbf{k}$. Indeed the expressions of the generalized Rabi frequency and the exchange term in Eqs. (2.55) and (2.56) show that the Coulomb interaction leads to a coupling of all momentum states. Eqs. (2.53) and (2.54) also describe the generation of electrons and holes pairs by absorption of light and show that the rate of change of the hole population is identical to the rate of change of the electron population. However, The Hartree-Fock equations do not take into account the many-body effects which lead to the plasma screening. Nevertheless, it is possible to replace V_q with a screened Coulomb potential V_q^s as defined in section 2.1.3; but, as the Hamiltonian with the bare Coulomb potential already contains the mechanism for plasma screening, one has to be careful with an *ad hoc* phenomenological inclusion of effects of plasma screening which might be counted twice if one goes beyond the RPA. Finally, as one deals with a mixture of both types of quasi-particles, the screening of the Coulomb potential needs to take into account the effects of both excited electrons and holes at the screened Hartree-Fock level. Thus, assuming that the total screening is given by the sum of the effects resulting from the separate electron and hole plasmas[16], the 2D plasma frequency, Eq. (2.28), the 2D effective plasmon frequency,Eq. (2.29), and the 2D screening wavenumber in Eq. (2.14), become:

[15] In chapter 5, we shall see that depending on the initial spin populations, the exciton resonances are differently located.

[16] We neglect the excitonic screening which at high enough plasma density is a good approximation.

$$\begin{cases} \omega_{pl}^2 = \omega_{pl,e}^2 + \omega_{pl,h}^2 \\ \omega_q^2 = \omega_{q,e}^2 + \omega_{q,h}^2 \\ \kappa = \dfrac{e^2}{2\pi\epsilon\hbar^2} \ \sum_{\alpha=e,h} m_\alpha n_{k=0}^\alpha = \kappa_e + \kappa_h \end{cases} \tag{2.57}$$

The energy renormalisation of the single particles in the valence band is defined in Eq. (2.45). If one replaces the bare Coulomb potential V_q by the screened potential V_q^s, Eq. (2.45) becomes

$$E_{h,k}^s = -E_{v,k} + \sum_{\mathbf{q}\neq\vec{0}} V_q^s = \hbar\epsilon_{h,k}^s. \tag{2.58}$$

This equation defines the hole energy in the presence of the screened Coulomb potential and can also be expressed this way:

$$E_{h,k}^s = -E_{v,k} + \sum_{\mathbf{q}\neq\vec{0}} V_q - \sum_{\mathbf{q}\neq\vec{0}} \left(V_q - V_q^s\right) = E_{h,k} + \sum_{\mathbf{q}\neq\vec{0}} \left(V_q^s - V_q\right). \tag{2.59}$$

The last term in Eq. (2.59) which can be considered as an additional contribution to the bandgap renormalization, is called the Coulomb-hole self energy or Debye shift ΔE_{CH} [42]:

$$\Delta E_{CH} = \sum_{\mathbf{q}\neq\vec{0}} \left(V_q^s - V_q\right). \tag{2.60}$$

The Debye shift is not dependent on the wave vector and is negative for finite plasma densities. From now on, we suppose that it is implicitly included in the definition of the renormalized single-particle energies:

$$\hbar e_{i,k} = \hbar\epsilon_{i,k} + \Sigma_{exc,i}(k) + \frac{1}{2}\,\Delta E_{CH}, \qquad i = e, h. \tag{2.61}$$

These renormalized energies will also appear in the Fermi distributions together with the renormalized quasi-chemical potential:

$$f_{i,k} = \frac{1}{\exp\ \beta\left[\hbar e_{i,k} - \left(\mu_i + \Sigma_{exc,i}(k) + \frac{1}{2}\ \Delta E_{CH}\right)\right] + 1} = \frac{1}{\exp\ \beta\left(\hbar\epsilon_{i,k} - \mu_i\right) + 1}\ , \tag{2.62}$$

where the index i stands for electrons (e) and holes (h). As the renormalization of the energies $\hbar e_i$ is exactly the same as it is for the quasi-chemical potential μ_i, they cancel each other in the Fermi distributions which remains unchanged.

Finally, there are several sources of dephasing such as carrier-carrier ($e-e$, $e-h$ and $h-h$) scattering, carrier-phonon scattering, scattering by impurities or lattice imperfection (inducing local modifications of the Coulomb potential). These effects can be considered either by including from the beginning of the calculations additional terms to the Hamiltonian in Eq. (2.43) (which here only describes the electronic interactions) or by adding phenomenological decay and dephasing contributions to the equations at the end of the calculations. To obtain even more accurate results, one has to go beyond the Hartree-Fock level. This can be done by separating the equations of motion for $n_{e,\mathbf{k}}(t)$, $n_{h,\mathbf{k}}(t)$ and $p_{\mathbf{k}}(t)$ into two parts in the following way:

$$\frac{\partial}{\partial t}\ \langle\hat{\mathcal{O}}(t)\rangle = \frac{\partial}{\partial t}\ \langle\hat{\mathcal{O}}(t)\rangle_{HF} + \frac{\partial}{\partial t}\ \langle\hat{\mathcal{O}}(t)\rangle\Big|_{col}, \tag{2.63}$$

where the collision terms which have to be evaluated stand for the corrections to the Hartree-Fock equations (2.52), (2.53) and (2.54). For instance, if one concentrates on the electronic contributions to carrier scattering and dephasing and this four operator term $\langle\alpha^\dagger_{\mathbf{k}}\alpha^\dagger_{\mathbf{k'-q}}\alpha_{\mathbf{k-q}}\alpha_{\mathbf{k'}}\rangle$, the collision contribution is defined as:

$$\delta\langle\alpha^\dagger_{\mathbf{k}}\alpha^\dagger_{\mathbf{k'-q}}\alpha_{\mathbf{k-q}}\alpha_{\mathbf{k'}}\rangle = \langle\alpha^\dagger_{\mathbf{k}}\alpha^\dagger_{\mathbf{k'-q}}\alpha_{\mathbf{k-q}}\alpha_{\mathbf{k'}}\rangle - \langle\alpha^\dagger_{\mathbf{k}}\alpha_{\mathbf{k}}\rangle\langle\alpha^\dagger_{\mathbf{k-q}}\alpha_{\mathbf{k-q}}\rangle\delta_{\mathbf{k},\mathbf{k'}}\ , \tag{2.64}$$

where $\langle\alpha^\dagger_{\mathbf{k}}\alpha_{\mathbf{k}}\rangle\langle\alpha^\dagger_{\mathbf{k-q}}\alpha_{\mathbf{k-q}}\rangle\delta_{\mathbf{k},\mathbf{k'}}$ comes from the random phase approximation which leads to the Hartree-Fock equations. The time derivative of the above collision contribution gives three terms which can be evaluated using the Heisenberg equation

and the electron-hole Hamiltonian in Eq. (2.43). The calculations involve two-, four- and six-operator terms. Leading further the calculations yields the carrier Boltzmann collision rates for the carrier-carrier scattering. This is not the object of this research work. Extensive studies can be found in the literature [47, 48, 49, 11, 50, 51].

2.3.2 Beyond the two-band approximation: the light hole contribution

Brief overview of the degenerate valence bands

A more realistic study of the semiconductor valence bands has to take into account the effect of the spin of the carriers: at high speed the spin of an electron interacts with the magnetic field created by its own motion. This coupling leads to an alteration of the energy levels in the semiconductor[17]. Band structure calculations done with Kane's **k**.**p** theory [52] for 3D and 2D systems show that the spin-orbit interaction lifts the degeneracy of the valence bands states. In this case only the total angular momentum $\mathbf{J} = \mathbf{L} + \mathbf{S}$ is conserved (i.e. commutes with the Hamiltonian of the system), which means that the eigenstates of the system are not eigenstates of the operators $\mathbf{L}^2$ and $\mathbf{L}_z$ with the associated spin up and down states, but of $\mathbf{J}^2$ and $\mathbf{J}_z$. To illustrate that, we give here some results of calculations of the semiconductor valence bands in the vincinity of the Γ-point of the Brillouin zone. Taking $L = 1$ and $S = 1/2$ leads to four eigenstates for $J = 3/2$ and two for $J = 1/2$. Restricting ourselves to the four optical states for $J = 3/2$, we find that these four states have two twofold degenerate energy eigenvalues, depending on the value of total spin magnetic moment m_J (i.e. the eigenvalue of J_z):

$$E = \frac{\hbar^2 k^2}{2m} \left(\gamma_1 + \frac{5}{2}\,\gamma_2 - 2\gamma_2 m_J^2\right), \tag{2.65}$$

γ_1 and γ_2 are the phenomenological Luttinger parameters [53, 54].

These energies are twofold degenerate because of their quadratic dependence on m_J:

[17] This leads to an additional relativistic term in the Hamiltonian. Another relativistic effect, which is not taken into account here, is the alteration of the mass of the electron.

- For $m_J = \pm 3/2$:

$$E_{hh} = (\gamma_1 - 2\gamma_2)\ \frac{\hbar^2 k^2}{2m}\ . \tag{2.66}$$

- For $m_J = \pm 1/2$:

$$E_{lh} = (\gamma_1 + 2\gamma_2)\ \frac{\hbar^2 k^2}{2m}\ . \tag{2.67}$$

E_{hh} and E_{lh} are the energies of the heavy-hole and the light-hole bands respectively. Looking at their expressions, one can see that at the point $k = 0$ these two bands are still degenerate. The degeneracy is lifted for finite values of k because of the different effective masses:

$$m_{hh} = m/(\gamma_1 - 2\gamma_2), \tag{2.68}$$

and

$$m_{lh} = m/(\gamma_1 + 2\gamma_2). \tag{2.69}$$

Eqs. (2.68) and (2.69) show the obvious origin of the terminology of the heavy and the light holes.

For 2D structures, one has to take into account both the effects of the energy of the confinement of the carriers (see section 2.2.1) and the strains which appear when one wants to accommodate a small mismatch of the lattice constants of two different materials by elastically straining one or both of the components. This leads to strained layer structures which can also be grown by molecular beam epitaxy. In this case, even for $k = 0$ there is no degeneracy since Eq. (2.67) becomes:

$$E_{lh} = \Delta E_{cs} + \frac{\hbar^2 k^2}{2m_{lh}}, \tag{2.70}$$

where ΔE_{cs} accounts for the band splitting due to strain and confinement. Its value can be taken from experiments.

Equations of motion

Since the heavy hole-light hole band splitting observed in the experiments described in chapter 5, is $\Delta_{cs} = 30$ meV, we neglect the heavy hole and light hole coupling. In the same fashion as above, calculations lead to:

$$\frac{\partial}{\partial t}\, p^{\lambda}_{\mathbf{k}}(t) = -i(e_{e,k} + e_{\lambda,k})\; p^{\lambda}_{\mathbf{k}}(t) - i(n_{e,\mathbf{k}}(t) + n_{\lambda,\mathbf{k}}(t) - 1)\; \omega^{\lambda}_{R,\mathbf{k}}(t)\;, \tag{2.71}$$

$$\hbar\frac{\partial}{\partial t}\, n_{e,\mathbf{k}}(t) = -2\ \mathrm{Im}\ (\omega^{\lambda}_{R,\mathbf{k}}(t)\; p^{\lambda *}_{\mathbf{k}}(t))\;, \tag{2.72}$$

and

$$\hbar\frac{\partial}{\partial t}\, n_{\lambda,\mathbf{k}}(t) = -2\ \mathrm{Im}\ (\omega^{\lambda}_{R,\mathbf{k}}(t)\; p^{\lambda *}_{\mathbf{k}}(t))\;, \tag{2.73}$$

for $\lambda = hh, lh$ and $e_{i,k}$ defined as in the above section[18]. The Rabi frequency is defined by:

$$\hbar\omega^{\lambda}_{R,\mathbf{k}}(t) = d^{\lambda}_{cv}\; \mathcal{E}(t) + \sum_{\mathbf{q}\neq\mathbf{k}} V_{|\mathbf{k}-\mathbf{q}|}\; p^{\lambda}_{\mathbf{q}}(t)\;. \tag{2.74}$$

Eqs. (2.72) and (2.73) describe the generation of electrons and holes pairs due to optical transitions from the valence bands to the conduction band. In these equations, just the coherent term is considered, and as long as the scattering (dephasing) terms are ignored, the rate of change of the hole population is identical to the rate of change of the electron population.

2.4 Conclusion

In this chapter, we gave an overview of the electronic and thermodynamic properties of semiconductor quantum wells, considering the finite width of the quantum wells. We assumed the 2D formulas to be valid for the chemical potential, but we intro-

[18]Including ΔE_{cs} in the definition of the light hole energy $\hbar e_{lh,k}$

duced a form factor to account for the alteration of the Coulomb potential energy in real heterostructures. We used the static plasmon-pole approximation to account for the screening in a 3-component electron/hole plasma. This allowed analytical calculations to be done in order to simplify the numerical work in the next chapters. The link between electronic, thermodynamics and optical properties of the electron-hole plasma was made introducing the electric-dipole interaction energy in the definition of the Hamiltonian, Eq. (2.22). The knowledge of the interband polarization $p_{\mathbf{k}}$ is required to evaluate the polarization function $P(t)$, and hence the optical susceptibility $\chi(\omega)$. One obtains $p_{\mathbf{k}}$ by solving the SBE, Eqs. (2.71), (2.72) and (2.73). We assume here that the screened Hartree-Fock approximation is sufficient to describe the interplay between the thermodynamics of the electron/hole plasma and its optical properties. As we shall see in the next chapter, the Coulomb many-body effects as well as the Pauli blocking entering Eq. (2.71) strongly influence the shape of the absorption spectra.

Chapter 3

Numerical solutions of the semiconductor Bloch equations

3.1 Introduction

In this chapter we present and discuss the numerical solutions of the SBE. We consider the specific case of quantum wells where Coulombic effects are more important than in the bulk systems. Although the electronic and thermodynamic properties of the electron-hole plasma were presented and discussed for $ZnSe$ only in chapter 2, the SBE will be solved considering two different types of materials: the mid-gap semiconductor $GaAs$ and the wide-gap semiconductor $ZnSe$. In this chapter we are also concerned with the comparison between the optical spectra computed for both type of materials as it will help in obtaining more physical insight as far as the interplay between the Fermionic nature of the carriers and the Coulombic effects in the electron-hole plasma is concerned. Moreover, it will also help us in assessing the quality of the screening model we use: in materials such as $ZnSe$ where the Coulomb interaction plays an important role, the limitations of the static plasmon-pole approximation are more visible than in the results obtained with materials such as $GaAs$. To discuss the basic properties of the absorption phenomenon, we present calculations done for $GaAs$ first.

3.2 Formulation of the numerical problem

Solving the SBE even at the screened Hartree-Fock level, i.e. Eqs. (2.52), (2.53) and (2.54), is a complicated task. As discussed below and in Appendix B, the Coulomb interaction term which couples all the equations, i.e. all the **k**-states is the main source of the difficulties that one has to deal with when solving the SBE (see also

Ref. [44]). It is numerically demanding and one has to find ways of simplifying the problems that in particular arise from the singular behaviour of the Coulombic terms and the coupling with the light field (nonlinearity of the SBE).

3.2.1 Simplifying the numerical work

The simplest situation is when one assumes that the plasma is in quasi-equilibrium and that the probe field $\mathcal{E}$ is sufficiently weak not to generate a significant population of carriers. Under these conditions, Eqs. (2.53) and (2.54) become:

$$\frac{\partial}{\partial t}\, n_{e,\mathbf{k}}(t) = \frac{\partial}{\partial t}\, n_{h,\mathbf{k}}(t) = 0, \tag{3.1}$$

and we only have to solve Eq. (2.52) which is an equation linear in the field. Furthermore, for the numerical analysis it is convenient to remove the rapidly varying phase factor from $p_{\mathbf{k}}$ and to work with a slowly varying polarization amplitude. To do so, we make the following substitution:

$$p_{\mathbf{k}} \longrightarrow p_{\mathbf{k}} e^{i\omega t}. \tag{3.2}$$

In this case, Eq. (2.52) becomes:

$$\frac{\partial}{\partial t}\, p_{\mathbf{k}}(t) = -i(e_{e,k} + e_{h,k} - \omega - i\gamma)\; p_{\mathbf{k}}(t) - i(n_{e,\mathbf{k}}(t) + n_{h,\mathbf{k}}(t) - 1)\; \omega_{R,\mathbf{k}}(t), \tag{3.3}$$

where the Rabi frequency $\omega_{R,\mathbf{k}}(t)$ is defined as in Eq. (2.55). The envelope of the electric field $\mathcal{E}(t)$ entering the definition of the Rabi frequency $\omega_{R,\mathbf{k}}(t)$ in Eq. (2.55), is assumed to be Gaussian, centered on $t = 0$:

$$\mathcal{E}(t) = \exp -(t^2/2\Delta_t^2), \tag{3.4}$$

where Δ_t is half the width of the pulse.

Note that for a more realistic description of the time dependence of the polariza-

tion $P(t)$ at the screened Hartree-Fock level as discussed at the end of section 2.3.1, we added a dissipative term to the SBE, by introducing a small phenomenological damping coefficient γ. Setting $\dot{p}_{\mathbf{k}}|_{col} \simeq -\gamma p_{\mathbf{k}}$ is the simplest approximation that one can make to simulate the collision contribution in Eq. (2.63) which describes the polarization decay (dephasing) and hence the broadening of the optical spectra, due to carrier-phonon scattering. This also facilitates the numerical convergence.

Another aspect of the numerical problem is to evaluate the discrete sums over $\mathbf{k}$-vectors appearing in Eqs. (2.55) and (2.56) for instance. The usual technique is to transform the discrete sum by an integral, assuming that replacing the discrete set of $\mathbf{k}$-vectors by a continuous carrier momentum distribution is a good approximation. In a two-dimensional problem this gives:

$$\sum_{\mathbf{k}} \longrightarrow \frac{\mathcal{A}}{4\pi^2} \int_0^{\infty}\int_0^{2\pi} k dk\, d\phi \tag{3.5}$$

3.2.2 Evaluation of the Coulomb matrix elements

In Eqs. (2.55) and (2.56) there are terms in which the Coulomb interaction $V_{|\mathbf{k}-\mathbf{q}|}$ exhibits a singularity for $\mathbf{k} = \mathbf{q}$ at low and zero density. This singularity has to be removed before undertaking any calculation, but considerable care must be taken when integrating in the vincinity of the singularity. On one hand, one does not want to perform the whole numerical integration with a dense mesh as it is time consuming; on the other hand, removing the singular points on a coarse mesh leads to a rather inaccurate result as an important number of points in the region where the discontinuous function is fast varying are neglected in the numerical integration. A way to overcome this sort of problem is to evaluate the difference between calculations which would be done with a dense mesh and calculations which would be done with a coarse mesh. This can only be done if $V_{|\mathbf{k}-\mathbf{q}|}$ is a slow enough varying function far from the singularity. The correction will be significant in the regions where $k \approx q$ (see Appendix C for further detail). In the quasi-equilibrium situation that is treated in this chapter, the evaluation of the Coulomb matrix elements $V_{|\mathbf{k}-\mathbf{q}|}$ has

to be performed only once for a given density as all the physical parameters remain constant.

To illustrate our discussion, we evaluate the nondiagonal elements that appear in the Rabi frequency, Eq. (2.55):

$$\sum_{\mathbf{q}\neq\mathbf{k}} V_{|\mathbf{k}-\mathbf{q}|}\; p_{\mathbf{q}}(t)\;. \tag{3.6}$$

The above expression can be rewritten this way:

$$\sum_{\mathbf{q}\neq\mathbf{k}} V_{|\mathbf{k}-\mathbf{q}|}\; p_{\mathbf{q}}(t) = \frac{e^2}{8\pi^2\epsilon}\int_0^\infty f_q q p_q\, dq \int_0^{2\pi} \frac{d\theta}{\sqrt{k^2+q^2-2kq\cos\theta}} = \int_0^\infty V^*(k,q)\; p_q\, dq\;, \tag{3.7}$$

assuming that there is no angular dependence in the interband polarization $p_{\mathbf{q}}$. The quantity $V^*(k,q)$ is the angle averaged Coulomb potential energy, defined as follows:

$$V^*(k,q) = \frac{e^2}{8\pi^2\epsilon}\; f_q q \int_0^{2\pi} \frac{d\theta}{\sqrt{k^2+q^2-2kq\cos\theta}}\;. \tag{3.8}$$

The above expression has to be computed numerically.

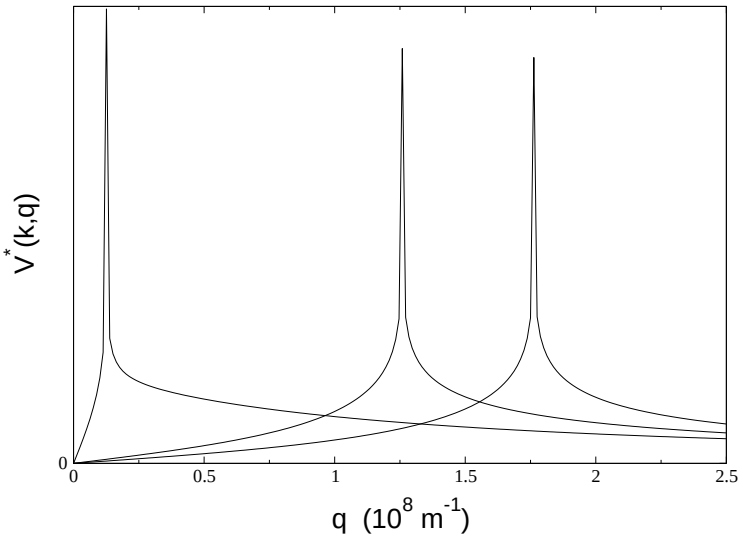

Figure 3.1: Singular behaviour of $V^*(k,q)$, for various values of k.

Because of the singular behaviour of $V^*(k,q)$ displayed in Fig. 3.1, its numerical evaluation is both difficult and time consuming. For further detail on how we treat this problem, see Appendix C.

3.3 The polarization function

From Eq. (2.40), we compute the complex polarization function $P(t)$ as follows:

$$P(t) = d_{cv} \sum_{\mathbf{k}} p_{\mathbf{k}}(t) \ . \tag{3.9}$$

To calculate $P(t)$ we need to solve first Eq.(3.3). To do so, we solve the coupled equations for Re $p_{\mathbf{k}}(t)$ and Im $p_{\mathbf{k}}(t)$:

$$\begin{aligned} \hbar \ \frac{\partial}{\partial t} \ \text{Re} \ p_{\mathbf{k}}(t) = -\hbar\gamma \ \text{Re} \ p_{\mathbf{k}}(t) + \hbar(e_{e,k} + e_{h,k} - \omega) \ \text{Im} \ p_{\mathbf{k}}(t) \\ +(n_{e,\mathbf{k}} + n_{h,\mathbf{k}} - 1) \sum_{\mathbf{q}\neq\mathbf{k}} V_{|\mathbf{k}-\mathbf{q}|} \ \text{Im} \ p_{\mathbf{q}}(t) \ , \end{aligned} \tag{3.10}$$

and

$$\begin{aligned} \hbar \ \frac{\partial}{\partial t} \ \text{Im} \ p_{\mathbf{k}}(t) = -\hbar\gamma \ \text{Im} \ p_{\mathbf{k}}(t) - \hbar(e_{e,k} + e_{h,k} - \omega) \ \text{Re} \ p_{\mathbf{k}}(t) \\ -(n_{e,\mathbf{k}} + n_{h,\mathbf{k}} - 1) \ (d_{cv} \ \mathcal{E}(t) + \sum_{\mathbf{q}\neq\mathbf{k}} V_{|\mathbf{k}-\mathbf{q}|} \ \text{Re} \ p_{\mathbf{q}}(t)) \ . \end{aligned} \tag{3.11}$$

Even though Re $p_{\mathbf{k}}(t)$ and Im $p_{\mathbf{k}}(t)$ are coupled, it is only Im $p_{\mathbf{k}}(t)$ whose time evolution is explicitly governed by $\mathcal{E}(t)$. The imaginary and real parts of $P(t)$ are shown in Fig. 3.2, for both a free carrier plasma and interacting plasma at zero and finite densities. The probe field $\mathcal{E}(t)$, whose center frequency is tuned on the bandgap, is also shown.

The amplitude of the real part, Re$P(t)$, is larger than the amplitude of the imaginary part, Im$P(t)$, for both the free carrier and interacting plasmas. The density dependence of the polarization function appears clearly: the higher the density is, the more bleached the peak of $P(t)$ is, for both interacting and non-interacting plasmas. This is due to the Pauli blocking effect reducing the oscillator strength.

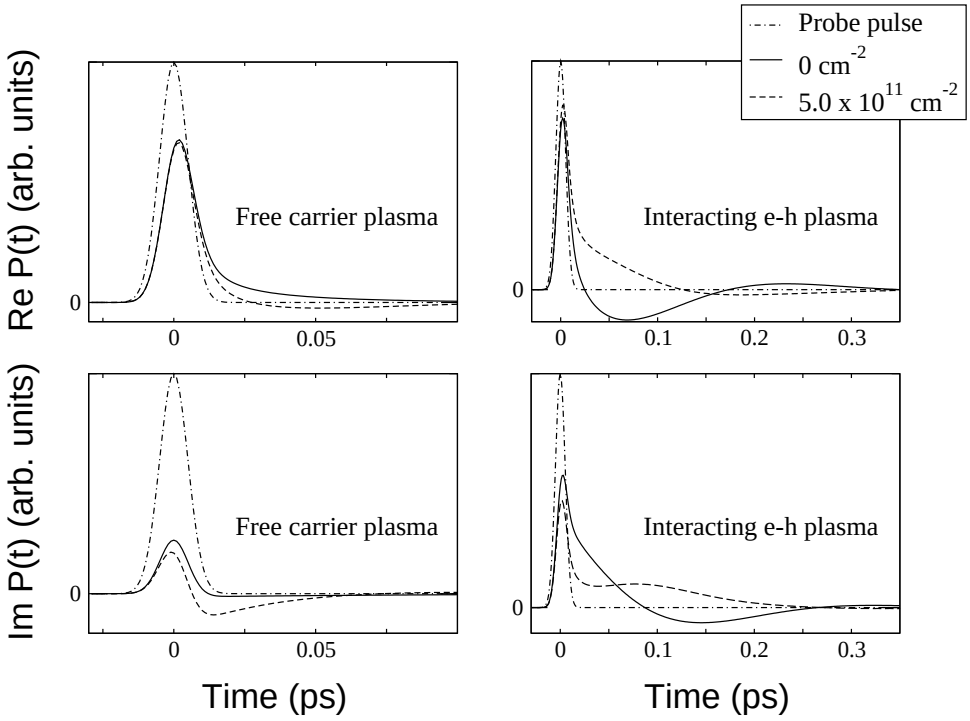

Figure 3.2: Real and imaginary parts of the polarization function as a function of time, in the case of both a free carrier plasma and interacting plasma for various plasma densities, in a 4 nm $GaAs$-based semiconductor quantum well. The plasma temperature is taken to be T = 77 K.

The decay of the polarization function reflects the presence of the phenomenological damping coefficient γ in Eq. (3.3), which accounts for the collisions in the plasma that cause the dephasing. Here $\hbar\gamma = 3.4$ meV. However, the inclusion of the Coulomb interaction enhances the amplitude of the polarization function which decays on a longer time scale (0.3 ps) when compared to the free carrier plasma (0.05 ps).

As one can see in Fig. 3.3 the behaviour of $P(t)$ is not just dominated by the damping γ, but is also influenced by the electron-hole attractive interaction.

The knowledge of the polarization function $P(t)$ is required to compute the optical susceptibility $\chi(\omega)$ defined as:

$$\chi(\omega) = \frac{\hat{P}(\omega)}{\epsilon\hat{\mathcal{E}}(\omega)}, \tag{3.12}$$

where $\hat{P}(\omega)$ and $\hat{\mathcal{E}}(\omega)$ are the Fourier transform of the polarization function $P(t)$

and of the electric field $\mathcal{E}(t)$. It is a complex function whose imaginary part gives the absorption $\alpha(\omega)$ [11]:

$$\alpha(\omega) \propto \mathrm{Im}\chi(\omega) \tag{3.13}$$

and whose real part gives the refractive index $n(\omega)$ [11]:

$$n(\omega) \propto \mathrm{Re}\chi(\omega). \tag{3.14}$$

These relations are valid for both interacting and noninteracting plasmas. Most of the spectra below will be shown as function of the photon energy scaled to the 3D Rydberg, R_y: $\Delta = (\hbar\omega - E_g)/R_y$.

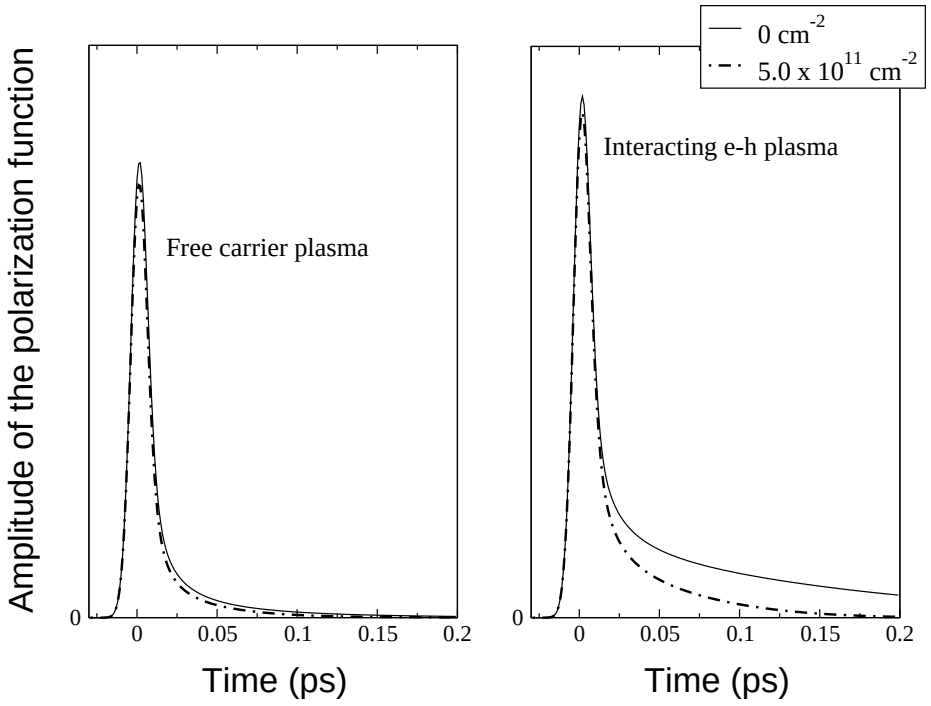

Figure 3.3: Polarization function as a function of time, in the case of both a free carrier plasma and interacting plasma for various plasma densities, in a 4 nm $GaAs$-based semiconductor quantum well. The plasma temperature is taken to be T = 77 K.

3.4 Absorption in a free carrier plasma

3.4.1 Density dependence of the absorption spectra

In the case of a free carrier plasma, for a given temperature, the density dependence of the absorption spectra comes only from the Pauli blocking effect. As we can see in Fig. 3.4, the presence of a finite plasma density affects the oscillator strength around the band edge.

A finite plasma density influences the shape of the absorption spectra: there is an overal blue shift and a bleaching of the absorption that becomes more and more important with increasing the plasma density. The lower energy conduction band states being occupied, the semiconductor can only absorb light at higher energy states, and the probability of such optical transition decreases. Another interesting effect occurs at higher density: the band filling factor $1 - n_e - n_{hh}$, and therefore the optical absorption can become negative if the chemical potential, $\mu = \mu_e + \mu_{hh}$, is positive and satisfies the inequality: $E_g < \hbar\omega < E_g + \mu$. For a given temperature this happens only if the density is high enough: we enter the gain regime and have stimulated emission.

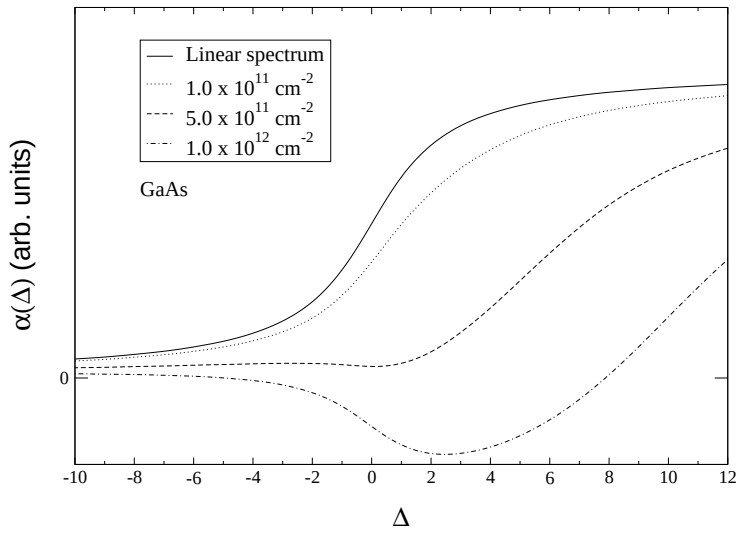

Figure 3.4: 2D free carrier plasma absorption spectra for various densities, at $T = 77$ K. The Pauli blocking is responsible for the blue shift of the absorption and the gain regime at high density.

3.4.2 Temperature dependence of the absorption spectra

The behaviour of the absorption spectra not only depends on the plasma density but also on the temperature, as shown below. In fact, the band filling factor that influences the oscillator strength decreases with increasing the plasma temperature. Indeed, the Pauli blocking effect reflects the Fermionic nature of the electron hole plasma. However, with increasing temperature the Fermion gas is less and less degenerate and the density has to be very high so as to have the chemical potential positive and satisfying the above inequality.

With increasing the plasma temperature for a given density, the absorption spectra in Fig. 3.5 show an increase of the probability of an optical transition around the band edge. However, one can also see that higher in the band the absorption is less effective at high temperature than it is at low temperature for a given density. This is due to the shape of the Fermi-Dirac distributions: at high temperature, the higher energy states are occupied which lowers the probability of an optical transition.

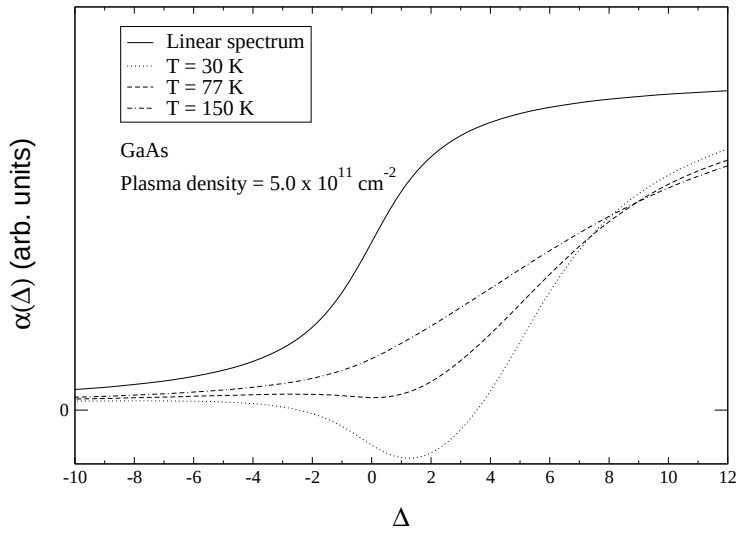

Figure 3.5: 2D free carrier plasma absorption spectra for various temperatures. The Pauli blocking that is responsible for the blue shift of the absorption and the gain regime at high density, becomes less important with increasing the plasma temperature.

3.5 Inclusion of the Coulomb interaction

The free carrier theory allows us to describe and explain the influence of the Fermionic nature of the carriers on the response of the electron-hole plasma. To obtain a more realistic description of the properties of the semiconductor media, one needs to take the Coulomb interaction into account as electrons and holes are electrically charged particles that interact. As shown below, the presence of the Coulomb forces in the plasma modifies significantly the shape of the absorption spectra displayed above as much as it complicates the analysis as one has to deal with the interplay between the Fermionic nature of the carriers with their electrical properties.

3.5.1 Many-body corrections

As explained in chapter 2, we solve the SBE at the screened Hartree-Fock level of approximation. As we shall see below, introducing the Coulomb interaction in the Hamiltonian, Eq. (2.22), yields many-body corrections arising from the Hartree-Fock contribution. These corrections are the renormalization of the electric-dipole interaction energy which leads to the excitonic enhancement of the interband transition probability and to the bandgap shrinkage because of energy shifts caused by the presence of a finite interacting plasma density.

Excitonic enhancement

First, we study the excitonic enhancement shown in Fig. 3.6. When computing absorption spectra including Coulomb interaction, the first striking feature is the exciton peak appearing below the band edge. In the case of a perfect 2D system, i.e. we do not consider the finite width of the quantum well, the location of the exciton resonance is exactly four times the excitonic Rydberg energy below the band edge: $R_y^{2D} = 4R_y$. This is the increased value of the quantum well exciton binding energy, due to the 2D confinement of the motion of the carriers. Another important feature is the enhancement of the continuum absorption, above the band edge. These two features can be well seen in Fig. 3.6. Finding the heavy hole exciton peak exactly

at R_y^{2D} below the band edge provides a good test for the quality of the numerical calculations.

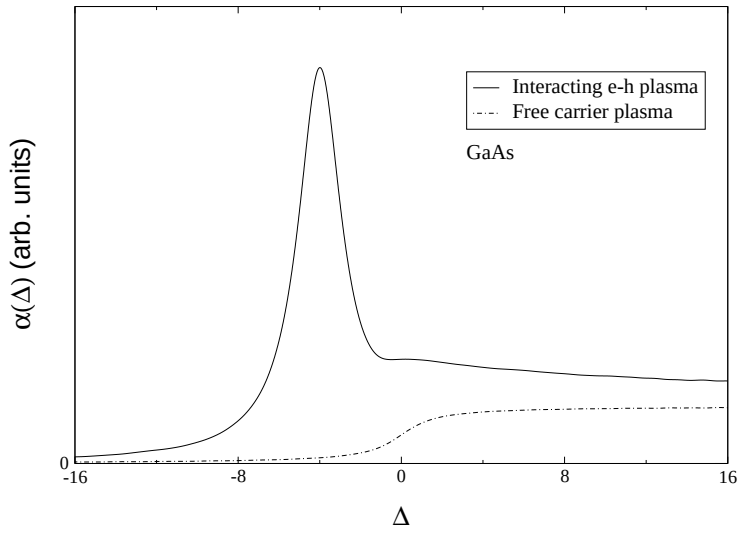

Figure 3.6: 2D interacting and noninteracting plasma linear absorption spectra. We can clearly see the excitonic resonance four Rydbergs below the band edge as well as the Coulomb enhancement in the continuum absorption region, above the band edge.

The existence of resonances and the enhancement of the continuum optical spectrum has its origin in the renormalization of the electric-dipole interaction energy which is caused by the attractive Coulomb interaction between the conduction and the valence bands. In particular, there is a pronounced increase in the optical absorption around the band edge when compared to the free carrier results. This can be explained as follows: because of the attractive Coulomb interaction between the conduction and the valence band, electrons and holes have a greater tendency to be in the vincinity of each other for a longer duration than would be the case if they were noninteracting particles. In other words, the interaction time is increased and leads to a higher probability of an optical transition. The broadening of the exciton resonance is essentially due to carrier-carrier scattering or carrier-phonon scattering in the electron-hole plasma. In our calculations, this is simply described by the phenomenological damping coefficient γ.

The bandgap renormalization

As stated earlier in this chapter, a finite plasma density causes the shrinkage of the bandgap because of the energy renormalizations of the single particle energies (see Eqs. (2.61)). The renormalization of the energy states is essentially due to the alteration of the Coulomb potential in the Hamiltonian of the electron-hole system. Indeed, with increasing the carrier density, more vacant valence band states are available to allow the redistribution of charges for more effective screening. Since the screening of a repulsive interaction leads to a lowering of the conduction electron energy, the transition energy decreases. As shown below, it is possible to evaluate the bandgap renormalization. However, the results that one may obtain heavily depend on the approximations used to perform the calculations. To be more specific, the quality of the screening model used to compute the screened Coulomb potential is of particular importance. The aim of this section is to show some results based on simplified calculations to support the comments and discussions in the next sections.

To calculate the bandgap renormalization we need to evaluate both the screened exchange self-energy, Eq. (2.56), and the Debye shift, Eq.(2.61). The screening model that is used in this work is based on the static plasmon-pole approximation (see Appendix A) which allows an analytical treatment of the problem of the energy renormalization. Noting that the k-dependence of the exchange self-energy is weak in the band-edge region, we can further simplify the calculations approximating the momentum transfer $|\mathbf{k}-\mathbf{q}|$ in Eq. (2.56), by the density dependent 2D Fermi wavevector k_F defined as follows:

$$k_F = (2\pi N)^{1/2}. \tag{3.15}$$

Inserting Eq. (3.15) into Eq. (2.56), and performing numerical calculations, also evaluating Eq. (2.60), yield the density dependence of the bandgap shrinkage displayed in Figs. 3.7 and 3.8. We also compare the results for low and high temperature regimes.

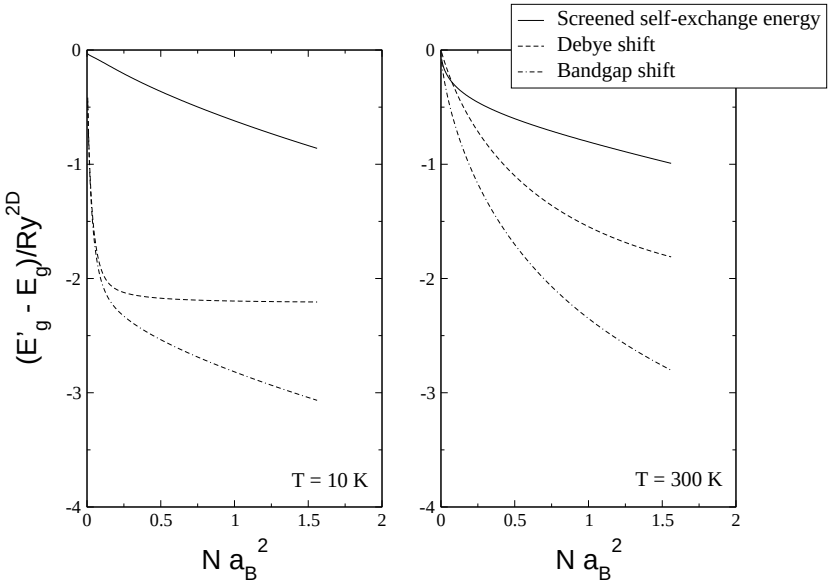

Figure 3.7: Two-dimensional bandgap shift scaled to the two-dimensional *GaAs* Rydberg as a function of the two-dimensional density scaled to the exciton Bohr radius at 10 K and 300 K.

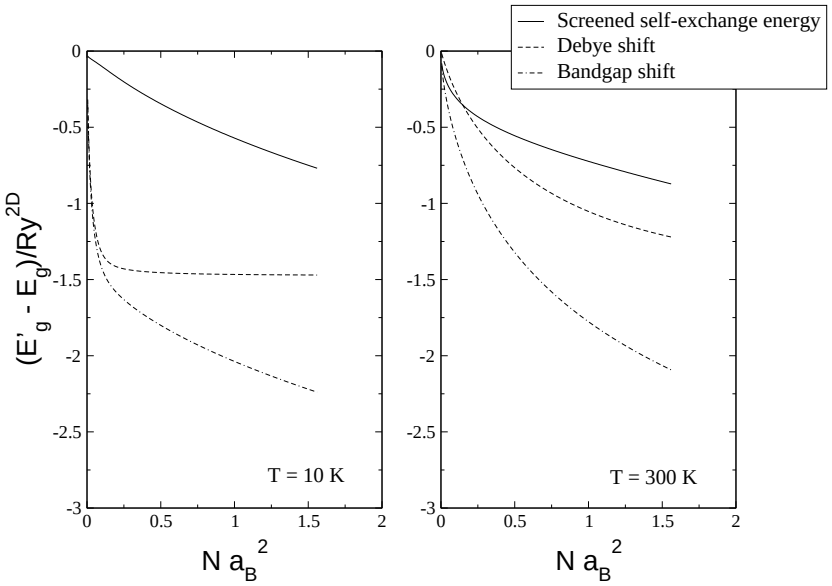

Figure 3.8: Bandgap shift scaled to the two-dimensional *GaAs* Rydberg in a 4 nm *GaAs*-based semiconductor quantum-well as a function of the two-dimensional density scaled to the exciton Bohr radius at 10 K and 300 K.

The bandgap renormalization clearly depends on both the plasma density and temperature. In particular, thanks to the Debye shift we can see the importance of the screening effect on the energy shifts. For a given temperature, increasing the plasma density enhances the renormalization of the energy states as both the Coulomb hole and the exchange energy increase. However, as mentioned earlier, for a given density, increasing the temperature lowers the plasma screening; as a

consequence, the strength of the Coulomb interaction becomes bigger; but, while the exchange self-energy also becomes bigger, the Coulomb hole energy, Eq. (2.60), becomes smaller. Both the exchange and Coulomb hole energies are additive, but the Debye shift having a more important contribution on the energy renormalization than the exchange energy, the overall result is a lowering of the energy shift. Note that at low temperature and high density, there is a saturation of the screening parameter as shown in Fig. (2.2). A consequence is that the Debye shift also saturates at low temperature and high density. For a given temperature and density, the introduction of the form factor in the calculations to account for a finite well-width modifies both the dielectric function and the strength of the Coulomb interaction which becomes smaller. That explains why the bandgap shrinkage is bigger in an ideal 2D system than it is actually in a quantum well. For further discussion, see Ref. [42].

3.5.2 Density dependence of the absorption spectra

As for the free carrier calculations, it is interesting to study the density dependence of the absorption spectra for a given temperature, when the Coulomb interaction is included in the analysis. Indeed, the location of the excitonic resonance as well as its height depend on the interplay between the Coulombic forces and the Fermionic nature of the carriers.

The absorption spectra in Fig. 3.9 show that the spectral location of the excitonic resonance is pretty much independent of carrier density as one can see on experimental spectra. This result is a consequence of the cancellation of two effects: lowering of the exciton binding energy and bandgap renormalization. Because of a finite plasma density, the Coulomb interaction is screened, hence weakened; the effective strength of the Coulombic forces is further decreased because of the phase space filling: as one can see in Eq. (3.3), the Pauli blocking factor lowers the Coulomb term entering the definition of the Rabi frequency, Eq. (2.55). This leads to a lowering of the exciton binding energy.

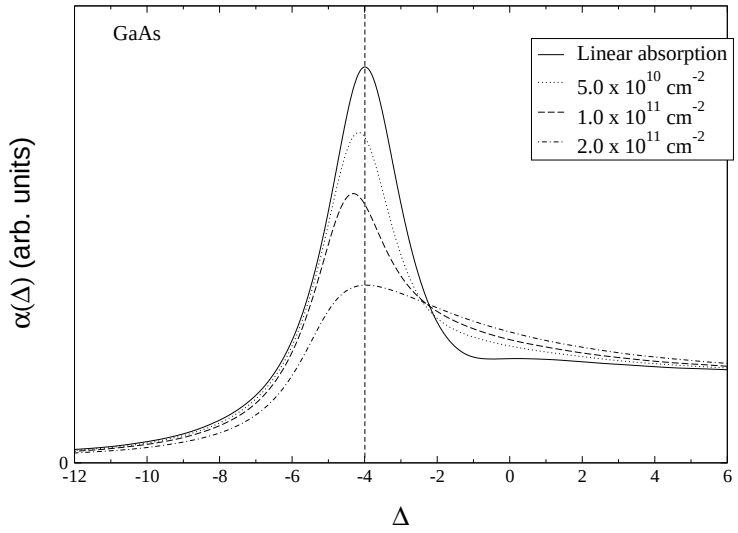

Figure 3.9: Absorption spectra in a $GaAs$-based semiconductor quantum well, including the Coulomb interaction, in a low density regime, at $T = 77$ K. Note the bleaching of the excitonic peak on essentially the same energy line as the excitonic resonance of the linear spectrum.

But, as seen in the above section the presence of carriers in the plasma also yields a bandgap shrinkage, and a consequence is that because of the energy shift of the band edge, the reduced exciton binding energy does not affect the location of the exciton peak on the optical spectrum. The bleaching of the exciton peak has also its origin in plasma screening and phase-space filling: because of plasma screening, the strength of Coulomb interaction is weakened and so is the excitonic enhancement; and, because of Pauli blocking, the probability of an optical transition is also lowered. When we study absorption spectra obtained with pump and probe experiments with spin-selective excitation, in chapter 5, we shall be in position to evaluate the relative importance of plasma screening and phase-space filling on the exciton peak bleaching.

As mentioned in the above sections, the quality of the screening model influences the accuracy of the results. Both the exciton binding energy and bandgap renormalization crucially depend on the screening. We chose to work using the quasi-static plasmon-pole approximation as it allows analytical calculations that simplify the difficult numerical treatment of the problem. Looking at the spectra in Fig. 3.9, one can

see that there is a slight red shift of the exciton peaks compared with experimental data, which becomes more and more important with increasing the plasma density. This shows the limitation of the screening model that we use: it overestimates the bandgap reduction. Comparison between bandgap renormalization evaluated with the quasi-static plasmon-pole approximation and with the dynamical plasmon-pole approximation can be found in the literature [42]. Despite this limitation, we obtain a good qualitative agreement with experimental results which is sufficient for our purposes.

In Fig. 3.10, we explore the high density regime. With increasing the density the plasma screening becomes more and more important. The Coulomb interaction is weak and exciton bound states tend to disappear. Moreover, as more and more low energy states are occupied, the probability of absorption becomes smaller. Hence the oscillator strength decreases with increasing plasma density. The above spectra show the exciton resonance vanishing as well as an increased absorption around the band edge. When one enters the gain region, the Coulomb interaction has not much effect on the shape of the absorption around the gap and the phase space filling effect becomes the dominant process as described above in the case of free carrier theory.

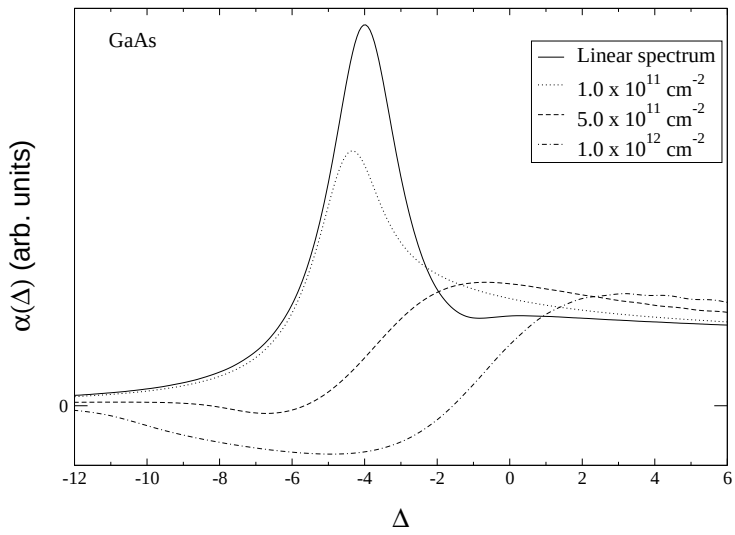

Figure 3.10: Absorption spectra in a $GaAs$-based semiconductor quantum well, including the Coulomb interaction, for various densities at $T = 77$ K.

3.5.3 Temperature dependence of the absorption spectra

As well as for the free carrier results, it is interesting to discuss the effect of the temperature on the absorption spectra when the Coulomb interaction is included in the calculations. As one can see on Figs. 3.7 and 3.8, for a given density, the temperature has an effect on the bandgap renormalization, but does not affect much the spectral location of the exciton resonance as the binding energy is also temperature dependent.

We choose to show absorption spectra at high density to show how an increase in the plasma temperature affects the gain and absorption. At high temperature, the phase space filling effect is weakened as the plasma is less degenerate. A consequence is that one needs to have a very high plasma density to enter the gain region at high temperature. The Coulomb interaction becomes more important as increasing the temperature lowers the plasma screening. As seen in Fig. 3.11, the absorption is less effective higher in the band at high temperature than it is at low temperature for a given density. This is due to the shape of the Fermi-Dirac distributions: at high temperature, the higher energy states are occupied which lowers the probability of an optical transition.

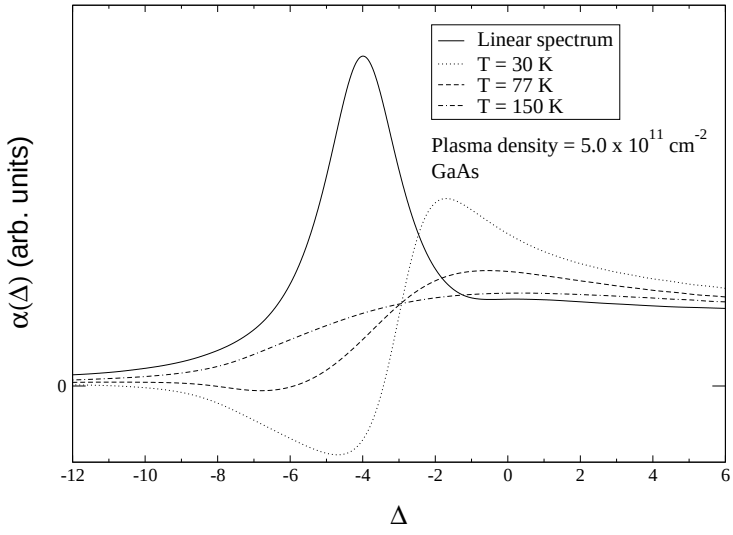

Figure 3.11: Absorption spectra in a semiconductor quantum well, including the Coulomb interaction, for various temperatures at a given density.

Note that we simplify the calculations by keeping the phenomenological damping coefficient γ constant when the plasma temperature and density vary.

3.6 Beyond the simple calculations: more realistic absorption spectra

For quantum wells having a finite well width, the Coulomb interaction between the confined carriers differs from the one in an ideal 2D system. We have discussed the effect of a finite well width on the Coulomb interaction in chapter 2, section 2, and the alteration one has to make to the Coulomb potential by introducing a form factor (see Appendix B). The Coulomb interaction being effectively weaker in a realistic quantum well heterostructure than it is in an ideal 2D electron-hole system, the exciton binding energy is smaller than the 2D Rydberg value given above. This is observed on experimental spectra. Another feature that is also observed is the presence of a light hole exciton peak just below the band edge. As seen in chapter 2, section 3, it is possible to derive an equation of motion for the interband polarization describing the optical transition between the light hole band and the valence band. We show in Figs. 3.12 and 3.13 absorption spectra taking into account the finite well width, and absorption spectra that exhibit light hole exciton resonances.

3.6.1 Effect of a finite well width

Including the form factors in the numerical calculations, considering Eqs. (2.28), (2.29) and (2.30), yields the results displayed in Fig. (3.12).

The linear spectrum in the case of the ideal 2D confinement exhibits an exciton resonance exactly located at the 2D Rydberg energy, which is four times bigger than the 3D Rydberg as well known. The introduction of a form factor blue shifts and bleaches the exciton resonance. One may explain the observed blue shift saying that the exciton binding energy being smaller, the exciton peak is located closer to the band edge than it is in the ideal case. As far as the exciton peak bleaching is concerned, the excitonic enhancement discussed above is less important when the Coulomb interaction interaction is weaker.

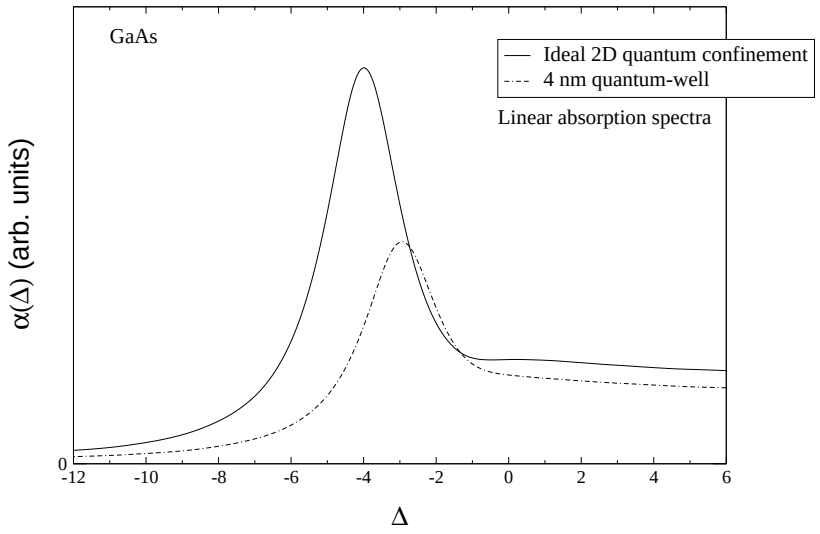

Figure 3.12: Linear absorption spectra in a semiconductor quantum well. Comparison between the ideal 2D quantum confinement and a 4 nm quantum-well.

3.6.2 Inclusion of the light hole

To evaluate the absorption spectra describing optical transitions from both the heavy and light hole bands to the conduction band, we solve Eqs. (2.71), (2.72), and (2.73), in the same fashion as discussed in section 3.2, at the begining of this chapter.

For our calculations with $GaAs$ parameters we arbitrary take the heavy hole-light hole band splitting to be $\Delta E_{cs} = 10$ meV, which is important enough to neglect the heavy hole and light hole coupling. In the case of $ZnSe$, we take $\Delta E_{cs} = 30$ meV from the experiments described in chapter 5. The absorption spectra $\alpha_{hh}(\Delta)$ and $\alpha_{lh}(\Delta)$ being computed, we obtain the total absorption spectrum $\alpha(\Delta)$ by adding them up: $\alpha(\Delta) = \alpha_{hh}(\Delta) + \alpha_{lh}(\Delta)$, as shown in Fig. 3.13. The density and temperature dependent properties we discussed above for the two-band model are still valid. However, one can see that there is a finite redshift of the light hole exciton peak which is more pronounced than for the heavy hole exciton peak. This comes from the screening model: the use of the quasi-static plasmon-pole approximation leads to an overestimation of the bandgap shrinkage which is not compensated by the lowering of the light hole exciton binding energy. The light hole exciton peak

properties are mainly dominated by the electrons in the quasi-equilibrium regime in which the light hole density is zero.

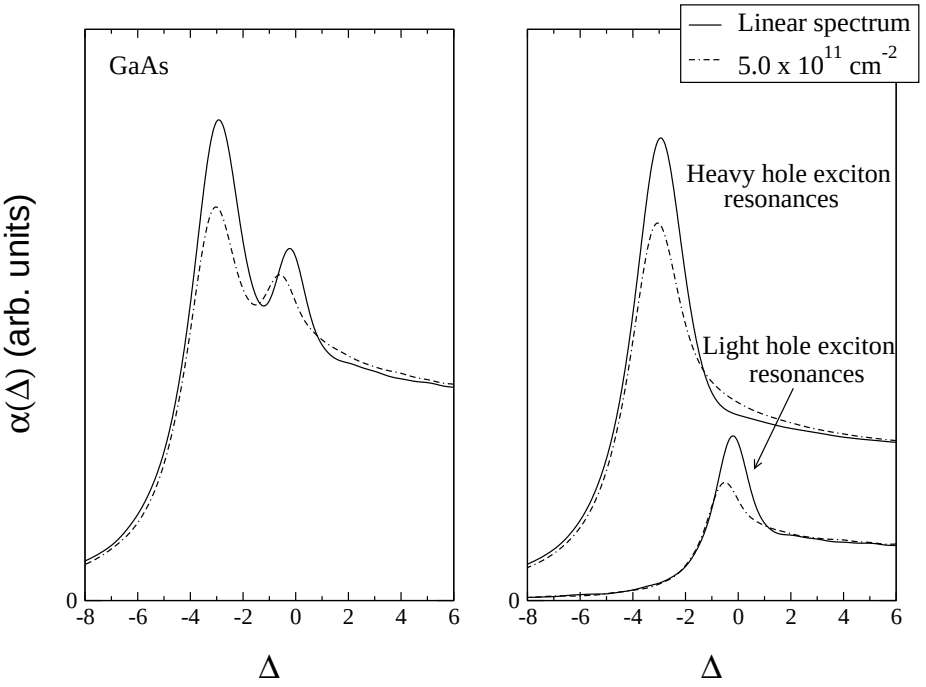

Figure 3.13: Absorption spectra in a 4 nm *GaAs*-based semiconductor quantum well including the light hole band. Comparison between the full spectra and the contributions of the heavy hole exciton and light exciton absorption spectra.

3.6.3 Comparison between GaAs and ZnSe

Until now, calculations were done with *GaAs* parameters to explain and illustrate the basic properties of the SBE and the absorption spectra. However, the results we shall present in the next chapters are based on *ZnSe* parameters as we have access to experimental data concerning the properties of this II−VI material. So, in the next section we compare numerical results obtained for *GaAs* and *ZnSe*. Having discussed above the basic properties, we can now proceed with a comparative analysis of the numerical calculations done with both types of materials, mid-gap *GaAs* and wide-gap *ZnSe* considering the finite well width and both the heavy and light bands. To do so, we shall work in dimensionless units for the plasma densities which will be scaled to the exciton Bohr radius a_B for each material.

The bandgap renormalization

In this section, the bandgap renormalization is calculated with $ZnSe$ parameters and shown in Fig. 3.14.

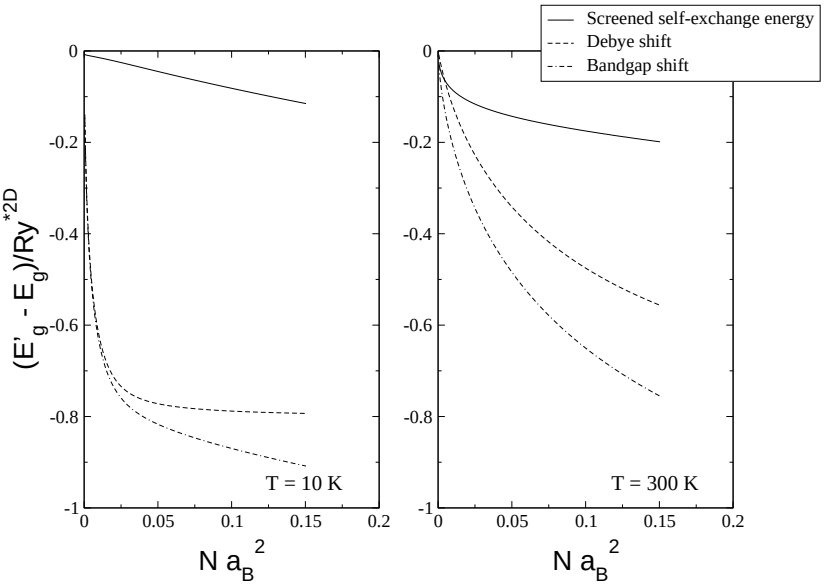

Figure 3.14: Bandgap shift scaled to the two-dimensional $ZnSe$ Rydberg in a 4 nm quantum-well as function of the two-dimensional density scaled to the exciton Bohr radius at 10 K and 300 K.

Because of the lower values of the dielectric constant ϵ and of the effective masses, m_e and m_{hh}, in $GaAs$ compared to $ZnSe$, the exciton Bohr radius a_B is bigger for $GaAs$ (see the Introduction for the values of these quantities). So, the first thing that one can note is that because of the smaller value of the exciton Bohr radius for $ZnSe$, the scaled density is smaller than it is for $GaAs$, whereas the plasma density is the same. The value of the bandgap shift also appears to be smaller in scaled units when compared to $GaAs$, but as the Rydberg energy is about five times bigger for $ZnSe$ than it is for $GaAs$, the bandgap shift is in fact much more important.

Differences between $ZnSe$ and $GaAs$ absorption spectra

Various physical parameters such as the bandgap energy, the dielectric constant and the effective masses play a role in the shape of the semiconductor absorption spectra (see the Introduction for the values taken for $GaAs$-based and $ZnSe$-based

semiconductor quantum-wells). When one compares the values of these parameters for $GaAs$ with those of $ZnSe$, one may think that the differences that are not so big should not lead to significant alteration on the absorption spectra of these materials. However, as we show in Fig. 3.15, this is not the case. In particular the optical properties of these materials crucially depend on the the value of the dielectric constant.

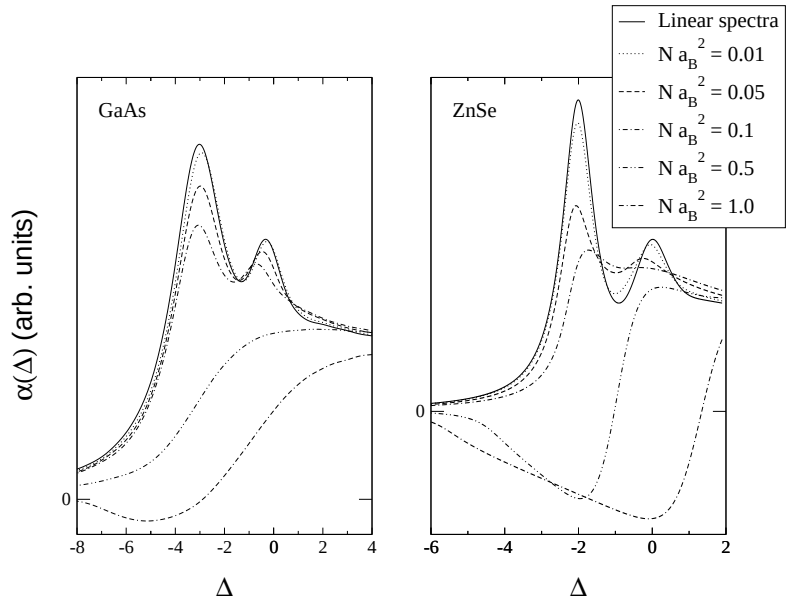

Figure 3.15: Comparison of the absorption spectra in $GaAs$ and $ZnSe$ 4 nm semiconductor quantum wells for various densities, at $T = 77$ K. Note that the 3D Rydberg being about five times bigger for $ZnSe$ than it is for $GaAs$, the frequency range covered by Δ is bigger for $ZnSe$ absorption than it is for $GaAs$.

We have seen in the above section that because of the finite well-width, the 2D heavy hole exciton binding energy is smaller than the 2D Rydberg. When comparing the location of the heavy hole exciton peaks for both materials, $GaAs$ and $ZnSe$, one can see that for the same well width, the alteration of the exciton binding energy is less important for $GaAs$ than $ZnSe$. This is simply due to the fact that the dielectric constant for $GaAs$ is smaller than for $ZnSe$: the Coulomb interaction being weaker for $GaAs$, the effect of a finite well width on the Coulomb interaction is less dramatic than it is for $ZnSe$. Another striking feature is that for the same scaled density, Na_B^2, the exciton peaks are much more bleached in the $ZnSe$ spectra than they are in the $GaAs$ spectra. This is essentially due to the bigger value of the

exciton Bohr radius a_B for $GaAs$, that makes the plasma density smaller for a given value of Na_B^2. However, for the same plasma density at a given temperature, the exciton peak in a $GaAs$ spectrum is more bleached than it is in a $ZnSe$ spectrum as we see in Fig. 3.16.

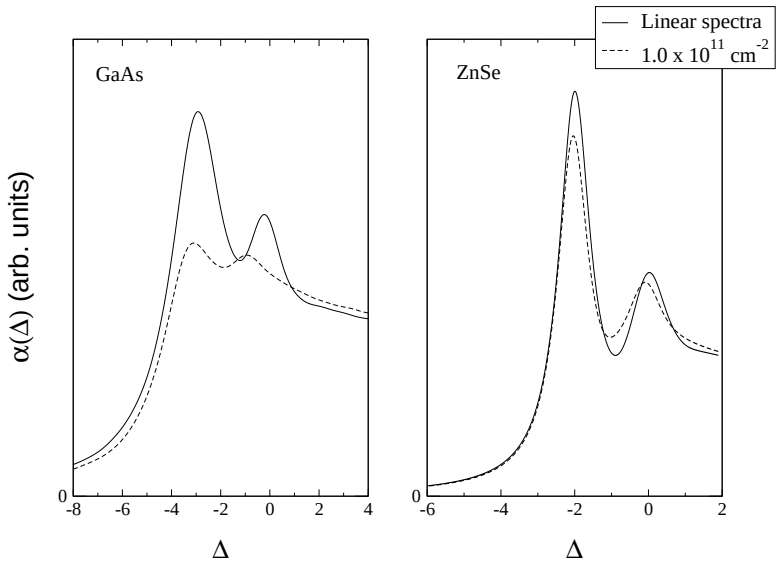

Figure 3.16: Comparison of the absorption spectra in $GaAs$ and $ZnSe$ 4 nm semiconductor quantum wells for a finite plasma density, at $T = 77$ K.

This feature can be well explained if one compares the thermal wavelengths of the carriers for both $GaAs$ and $ZnSe$. As the effective masses for $GaAs$ are smaller than they are for $ZnSe$ (see the Introduction), the thermal wavelengths of the carriers are bigger for $GaAs$ than they are for $ZnSe$. This means that for a given temperature and a given density, the electron-hole plasma is more degenerate in $GaAs$ than it is in $ZnSe$. A direct consequence is that the phase-space filling factor is more important in $GaAs$. Moreover, the Coulomb interaction being weaker in $GaAs$, the excitonic enhancement is also weaker.

Numerical problems for the highly degenerate regime

While writing and testing the codes for solving the SBE for both $GaAs$ and $ZnSe$, we saw that we had to be careful when evaluating the absorption spectra at high density and low temperatures as it yields unphysical behaviours such as spikes on

the absorption spectra as shown in Figs. 3.17 and 3.18.

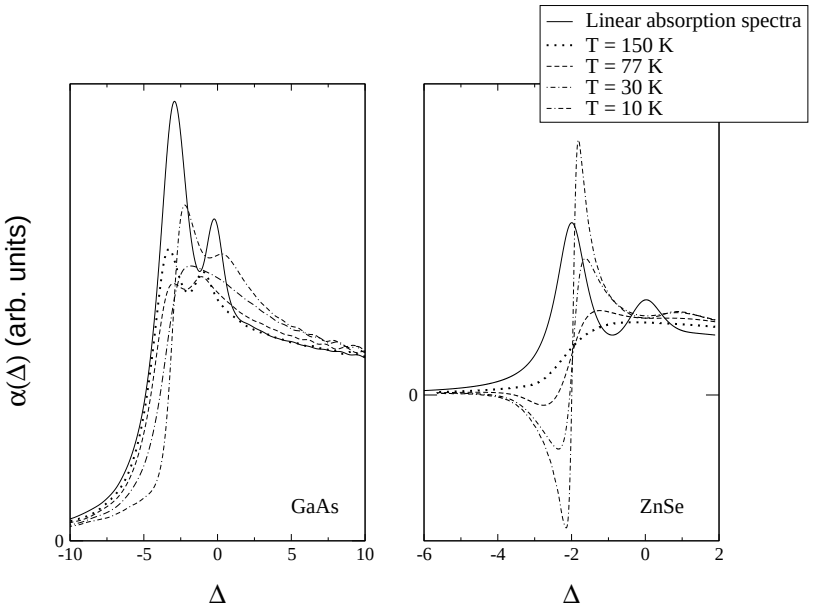

Figure 3.17: Unphysical behaviour of the numerical solutions of the SBE when decreasing the plasma temperature at a plasma density given by $Na_B^2 = 0.2$. Comparison between calculations done for *GaAs* and *ZnSe* parameters.

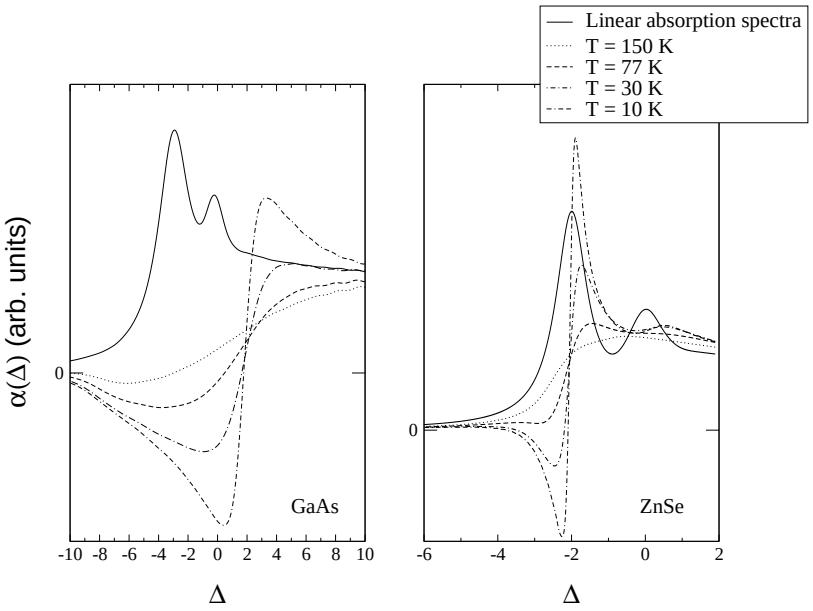

Figure 3.18: Unphysical behaviour of the numerical solutions of the SBE when decreasing the plasma temperature at a given high density, here 10^{12}cm^{-2}. Comparison between calculations done for *GaAs* and *ZnSe* parameters.

To discuss this problem we computed absorption spectra for various temperatures and evaluated the spectra with the same scaled density: $Na_B^2 = 0.2$, i.e.

$N_{GaAs} = 1.275 \times 10^{11}\text{cm}^{-2}$ and $N_{ZnSe} = 1.328 \times 10^{12}\text{cm}^{-2}$, and also with the same plasma density $N = 10^{12}\text{cm}^{-2}$. The numerical solutions of the SBE start being unphysical when the highly degenerate regime is entered, which for the chosen densities is below $T = 30$ K. For $Na_B^2 = 0.2$, as shown in Fig. 3.17, results obtained for $GaAs$ do not exhibit a dramatic behaviour as the one observed for $ZnSe$. This is due to the fact that N_{GaAs} is ten times smaller than N_{ZnSe}. However, for temperatures below than 30 K, two significant peaks appear below and above the band edge on the $GaAs$ spectra. These peaks are not excitonic as the phase space filling and plasma screening are too strong, and are not matching any experimental feature that one can observe for such density and temperature regime. For the same density $N = 10^{12}\text{cm}^{-2}$, the highly degenerate regime is entered at higher temperature for $GaAs$, as the carrier effective masses are lighter in $GaAs$. However, as one can see in Fig. 3.18, down to $T = 30$ K, the computed $GaAs$ absorption spectra are more reliable than those evaluated for $ZnSe$. Hence, this issue is not a simple matter such as using a mesh that is not accurate enough to account for the fast varying distribution Fermi functions around the chemical potential. Indeed, the Coulomb potential also seems to play a role, as numerical solutions of the SBE appear to be more stable for $GaAs$ at low temperature. One would need to take time to explore the interplay between the number of k-points, the shape of the Fermi distributions and the Coulomb interaction, so as to find a practical way to overcome this situation in order to compute absorption spectra at extremely low temperatures. Further discussion on numerical problems can be found in Ref. [44].

3.7 Refractive index spectra

In this thesis, we do not focus on the study of the refractive index, but it emerges naturally as a by-product of our calculations. Therefore, we only give a brief description of the figure below. For more detail, see Ref. [55].

The refractive index spectra in Fig. 3.19, are evaluated for an interacting electron/hole plasma. We can see clearly that the linear refractive index spectrum

exhibits a maximum and a minimum. With increasing the carrier density, the maximum decreases whereas the minimum increases. Keeping increasing the plasma density, the gain region (see the above section) is entered. Then the initial maximum disappears and the minimum becomes a maximum. This effect is often exploited in optical switching devices which are based on dispersive optical bistability [11, 56].

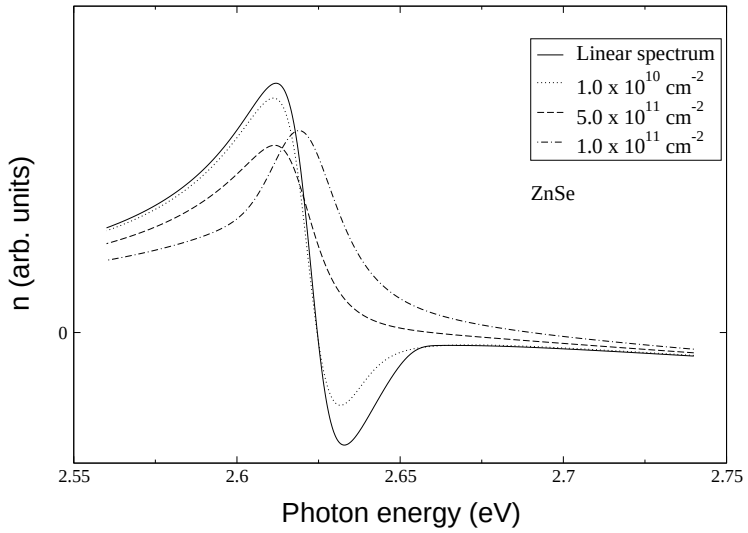

Figure 3.19: Refractive index spectra for various plasma densities in 4 nm $ZnSe$-based quantum-well, at $T = 77$ K.

3.8 Discussion and conclusion

In this chapter we illustrated in detail the calculations presented in chapter 2. We studied the interplay between the Fermionic nature of the carriers and the Coulombic forces that acts on them, exploring various regimes in temperature and density. Comparing results for two different type of material, mid-gap $GaAs$ and wide-gap $ZnSe$, we saw the more dominant role played by the Coulomb interaction on the optical properties of $ZnSe$-based semiconductor quantum-wells: Coulomb enhancement and bandgap renormalization are more important in $ZnSe$ than they are in $GaAs$. The effect of a finite well width was also taken into account and we showed that the strength of the 2D Coulomb interaction is smaller in real heterostructures than it is in an ideal 2D electron/hole system. Hence, the exciton binding energy is

not exactly four times the value of the Rydberg energy, but a decreasing function of the well width. The introduction of the light hole band in the calculations was necessary to account for the light hole exciton resonance that one can observe on experimental absorption spectra (see section 5.2 in chapter 5 for instance). We saw that the static plasmon-pole approximation yields an overestimation of the bandgap shrinkage as numerical results exhibits a slight redshift of the exciton resonances (see also Ref. [42]). All the calculations and numerical results presented in this chapter were done assuming a quasi-equilibrium situation defined by $\mu_{lh} = \mu_{hh} \neq \mu_e$ and $T_e = T_{hh}$, i.e. $N_{lh} \approx 0$ and $N_e = N_{hh}$: the intraband scattering has led to a fast equilibration of the initial carriers distributions within the bands and the plasma cooling has led to a cooling of the carriers temperatures down to the lattice temperature. All the results presented in this chapter as well as in chapter 2, together with the discussion and comments that we made, will help when we study the nonequilibrium regime in the next two chapters.

Chapter 4

Nonequilibrium carrier dynamics in semiconductor quantum-wells

4.1 Introduction

In thermal equilibrium, all elementary excitations in a semiconductor (electrons, holes, phonons...) can be characterized by a temperature that is the same as the lattice temperature. Under the influence of an external perturbation such as an electric field or an optical excitation, the distribution functions of these elementary excitations deviate from those in thermal equilibrium. In general, the nonequilibrium distributions are nonthermal, i.e. they are not characterized by a temperature. The term "hot carriers" is often used to describe this nonequilibrium situation. In this chapter, we study the time evolution of an initially hot electron/hole plasma created by optical pumping. This can be described as follows: after the fast dephasing time (see Introduction and Ref. [6]), the energy in the carrier gas is redistributed as a result of carrier-carrier collisions, and the initial nonthermal distributions approach thermalized distributions with characteristic temperatures for electrons and holes, T_e and T_h. Then, the electrons and holes thermalize with each other by electron-hole collisions, so that the plasma can be described by a common temperature, T_c. This temperature can be different from the lattice temperature, T_{lat}. The next process is the plasma cooling by interactions with the phonons.

Properties of hot carriers are determined by various interactions between carriers and other elementary excitations in the semiconductor. Therefore their investigation is of fundamental interest as it provides information about scattering processes. In this chapter, we are concerned with the nonequilibrium thermodynamics of spin-polarized carrier gases and their mutual interaction as we consider

excitations created by spin-selective optical pumping.

The object of chapters 2 and 3 was to present the theoretical framework in which one can study the absorption phenomenon in semiconductor quantum-wells in a quasi-equilibrium situation. Here, based on the available experimental data (see next chapter) we move beyond such a quasi-equilibrium situation: we include six dynamical processes which lead eventually to a thermal quasi-equilibrium in the electron-hole plasma: relaxation of the hot carriers distributions towards Fermi-Dirac distributions, thermalization, plasma cooling, carrier spin-flip, scattering between the light and heavy hole bands and recombination (both radiative and non-radiative). A microscopic treatment accounting for all these many-body effects is computationally prohibitive. Instead, we use a phenomenological approach to describe the time evolution of the electron-hole plasma.

The aim of this chapter is to present our model for the time evolution of the electron-hole plasma created by spin-selective excitation. In section 4.2, we study the dynamical processes mentioned above to describe the time evolution of the carrier distributions and the nonequilibrium plasma screening. Section 4.3 deals with the plasma initial conditions created by the polarized pump beam. In particular, we account for the selection rules for the optical transitions and we assume the initial hot carrier distributions to be Gaussian. In section 4.4, we present and discuss numerical results. Finally, section 4.5 concludes this chapter with a summary and a discussion on our model.

4.2 Dynamical processes

4.2.1 Time evolution of the carrier distributions

In our model, the time evolution of the distribution function, $n^{\sigma}_{c,\mathbf{k}}(t)$, of a carrier c with a spin σ takes several dynamical processes into account. Relaxation of the carrier distributions, carrier spin-flip, recombination and light hole scattering yield the following system of six coupled differential equations ($\sigma = \uparrow$ or $\downarrow$ indicating the two spin-states):

$$\frac{dn^{\sigma}_{e,\mathbf{k}}}{dt} = \frac{n^{eq,\sigma}_{e,\mathbf{k}} - n^{\sigma}_{e,\mathbf{k}}}{\tau^{e}_{eq}} + \frac{n^{therm,\sigma}_{e,\mathbf{k}} - n^{\sigma}_{e,\mathbf{k}}}{\tau^{e}_{therm}} + \frac{n^{\sigma'}_{e,\mathbf{k}} - n^{\sigma}_{e,\mathbf{k}}}{\tau^{e}_{sf}} - \frac{n^{\sigma}_{e,\mathbf{k}}\, n^{\sigma'}_{hh,\mathbf{k}}}{\tau^{e,hh}_{rad}} - \frac{n^{\sigma}_{e,\mathbf{k}}\, n^{\sigma}_{lh,\mathbf{k}}}{\tau^{e,lh}_{rad}} - \frac{n^{\sigma}_{e,\mathbf{k}}}{\tau^{e}_{nr}} ,$$

$$\frac{dn^{\sigma}_{hh,\mathbf{k}}}{dt} = \frac{n^{eq,\sigma}_{hh,\mathbf{k}} - n^{\sigma}_{hh,\mathbf{k}}}{\tau_{eq}} + \frac{n^{therm,\sigma}_{hh,\mathbf{k}} - n^{\sigma}_{hh,\mathbf{k}}}{\tau_{therm}} + \frac{n^{\sigma'}_{hh,\mathbf{k}} - n^{\sigma}_{hh,\mathbf{k}}}{\tau^{hh}_{sf}} - \frac{n^{\sigma'}_{e,\mathbf{k}}\, n^{\sigma}_{hh,\mathbf{k}}}{\tau^{e,hh}_{rad}} + \frac{n^{\sigma}_{lh,\mathbf{k}}}{2\tau_{lh}} + \frac{n^{\sigma'}_{lh,\mathbf{k}}}{2\tau_{lh}} , \qquad (4.1)$$

$$\frac{dn^{\sigma}_{lh,\mathbf{k}}}{dt} = \frac{n^{eq,\sigma}_{lh,\mathbf{k}} - n^{\sigma}_{lh,\mathbf{k}}}{\tau^{lh}_{eq}} + \frac{n^{therm,\sigma}_{lh,\mathbf{k}} - n^{\sigma}_{lh,\mathbf{k}}}{\tau^{lh}_{therm}} + \frac{n^{\sigma'}_{lh,\mathbf{k}} - n^{\sigma}_{lh,\mathbf{k}}}{\tau^{lh}_{sf}} - \frac{n^{\sigma}_{lh,\mathbf{k}}\, n^{\sigma}_{e,\mathbf{k}}}{\tau^{e,lh}_{rad}} - \frac{n^{\sigma}_{lh,\mathbf{k}}}{\tau^{lh}_{nr}} - \frac{n^{\sigma}_{lh,\mathbf{k}}}{\tau_{lh}} .$$

These equations are numerically solved to obtain the time dependence of the carrier distributions $n^{\sigma}_{c,\mathbf{k}}(t)$ whose values are between 0 and 1. The various terms entering the above system are described as follows:

Intraband scattering (τ_{eq} terms): the optical pumping creates a population of hot carriers. One of the fastest processes (i.e. subpicosecond time scale [6]) that occurs in each band is the rapid equilibration of these carriers: due to carrier-carrier scattering the initial hot carrier distributions evolve towards Fermi-Dirac quasi-equilibrium distributions. Extensive work on this specific topic involving the quantum Boltzmann equation can be found in the literature [47, 48, 49, 50, 51]. Here we use a phenomenological approach to describe the time evolution of the hot carrier distributions which is characterized by a relaxation time τ_{eq} associated with intraband scattering. Thus, the quantities $n^{eq,\sigma}_{c,\mathbf{k}}$ in Eqs. (4.1) are Fermi-Dirac distributions describing the quasi-equilibrium for each spin-polarized subsystem, having the same carrier density and energy as the nonequilibrium distribution. Note that the intraband scattering does not change the carrier densities nor the total kinetic energy.

Carrier thermalization (τ_{therm} terms): a process that also influences the time evolution of the carrier distributions is the thermalisation process amongst carriers of different types. The scattering between electrons and heavy and light holes is a process that drives the initial carrier temperatures, T_c^σ, to a common quasi-equilibrium temperature, T_{eq} that can be different from the lattice temperature, T_{lat}. To evaluate T_{eq}, one needs to calculate the total plasma energy E_{tot} and then compute the corresponding temperature T_{eq} assuming a Fermi-Dirac distribution. To account for the thermalization process, we suppose that the time evolution of the distribution functions is characterised by a phenomenological time τ_{therm}. Thus, the quantities $n_{c,\mathbf{k}}^{therm,\sigma}$ in Eqs. (4.1) are Fermi-Dirac distributions describing the quasi-equilibrium for each spin-polarized subsystem, having the same carrier density but an energy corresponding to the common quasi-equilibrium temperature T_{eq}.

Carrier spin-flip (τ_{sf} terms): the spin-flip is a process by which the spin orientation of a carrier is reversed. The detailed mechanisms responsible for such a phenonemon are not yet well understood despite extensive studies [57, 58, 59, 60, 61, 62, 63, 64, 65, 66, 67] and we shall consider the spin-flip phenomenologically with the associated characteristic time τ_{sf}. The spin-flip introduces a coupling between the spin-states σ and σ' for a given type of carrier c which considerably complicates the solution of Eqs. (4.1). The value of τ_{sf} is poorly known and one of our aims with this model would be to extract this from the experimental data.

Recombination (τ_{rad} and τ_{nr} terms): we distinguish here between radiative and nonradiative recombination. Radiative recombination is a process that occurs on relatively long time scale compared to the others described above ($\tau_{rad} \sim 1$ ns in $ZnSe$). Time resolved photoluminescence experiments are used to study this phenomenon [68, 69]. For an optical transition to occur one needs to have an electron in the state $\mathbf{k}$ together with a light or a heavy hole in the same state $\mathbf{k}$ provided

that their spins satisfy the selection rules described later in this chapter. The total observed luminescence intensity $I_{pl}(t)$ is directly linked to the distribution functions of these carriers:

$$I_{pl}^{\lambda}(t) \propto \sum_{\mathbf{k}} |d_{cv}^{\lambda}|^2 \; n_{e,\mathbf{k}}^{\sigma}(t) \; n_{\lambda,\mathbf{k}}^{\sigma'}(t) \; , \tag{4.2}$$

for the heavy and light hole optical transitions, where $\lambda = lh$ or hh, and d_{cv} is the dipole matrix element.

For a detailed study of radiative recombination and spontaneous emission rate, see Ref. [70]. Detailed calculations to evaluate τ_{rad} can be found in Ref. [71] and in Appendix D, and its expression is given by Eq. (D.13). The term τ_{nr} in the right hand side of Eq. (4.1) accounts for the nonradiative recombination. Radiative and nonradiative recombination are two competing processes. Experimental data shown in chapter 5 show that it is a faster process than the radiative recombination at high plasma density. Nonradiative recombination occurs either via recombination centers or by Auger processes. Recombination centers are usually deep impurity levels close the bandgap center. In Auger processes, the energy released as a consequence of the recombination is transferred to another electron. This electron gets excited into a higher state in the band from where it can return step by step to its ground state without radiation, by scattering with phonons. The likelihood of Auger processes increases as the carrier density increases. Experimental studies of the nonradiative recombination can be found in [72, 73, 74]. A theoretical study of Auger processes including the effects of electron-hole correlations can be found in [75].

Heavy hole and light hole scattering (τ_{lh} terms): away from the zone centre, both heavy and light holes are mixtures of the bulk valence band states. This enhances the intersubband scattering between the heavy and light hole bands. Many processes involving other quasi-particles (heavy and light holes, phonons, excitons...) can facilitate this type of scattering, and it is non-trivial to assess the relative importance of each of the processes. To avoid such complication we

make a simple approximation assuming that this scattering is spin-independent, i.e. $|3/2, 1/2\rangle_{lh}$ scatters equally into $|3/2, 3/2\rangle_{hh}$ and $|3/2, -3/2\rangle_{hh}$ and vice-versa. When the quasi-equilibrium between the heavy hole and the light hole bands is reached, their chemical potentials have to satisfy the relation: $\mu_{lh} = \mu_{hh} - \Delta E_{cs}$ because of the band splitting due to the confinement and strain. Solving this equation at low temperature and for typical electron-hole plasma densities, i.e. of the order of 10^{11} cm^{-2} or more, yields a negligible light hole density: $N_{lh}/N \approx 0$. Hence, we include a simple decay characterised by the time τ_{lh} in Eqs. 4.1 to model the light hole scattering.

4.2.2 Plasma cooling

The intraband scattering dominates the fast carrier distribution relaxation, but is not a process that dissipates energy. Thus, the initial electron-hole plasma temperature is determined by the kinetic energy of the nonequilibrium distribution created by the femtosecond pump pulse. Depending on the energy of the excitation pulse, the effective plasma temperature can be well above the lattice temperature. The most important source of energy dissipation is due to the coupling of the electronic system with the lattice. The plasma cooling can be treated by solving the quantum Boltzmann equation describing the carrier-phonon scattering [50, 51], but we restrict ourselves to a phenomenological approach. Hence, the loss of carrier kinetic energy obeys a rate equation:

$$\frac{dE^{\sigma}_{tot,c}}{dt} = \frac{E^{eq,\sigma}_{tot,c} - E^{\sigma}_{tot,c}}{\tau_{cool}} \ . \tag{4.3}$$

The total energy $E^{eq,\sigma}_{tot,c}$ per unit area calculated from the quasi-equilibrium distribution $n^{eq,\sigma}_{c,E}$ at the lattice temperature is given by:

$$E^{eq,\sigma}_{tot,c} = \sum_{E} E \ n^{eq,\sigma}_{c,E} = \frac{m_c}{2\pi\hbar^2} \times \int_0^{\infty} \frac{E \ dE}{\exp \beta_{lat}(E - \mu^{\sigma}_c) + 1} \ . \tag{4.4}$$

The chemical potential $\mu^{\sigma}_c(N^{\sigma}_c, T^{\sigma}_c)$ is given by:

$$\mu_c^\sigma(N_c^\sigma, T_c^\sigma) = \frac{1}{\beta_c^\sigma}\ \ln\Big(\exp\ (2\pi\hbar^2\beta_c^\sigma N_c^\sigma/m_c) - 1\Big)\ , \tag{4.5}$$

where N_c^σ and β_c^σ are the 2D density and the inverse thermal energy of the carrier of type c in the spin state σ. This integral has to be calculated numerically. $E_{tot,c}^\sigma(t=0) = E_{tot,c}^{G,\sigma}$ is the total energy per unit area calculated from the initial nonequilibrium distribution $n_{c,E}^{G,\sigma 1}$ as follows:

$$E_{tot,c}^{G,\sigma} = \sum_E E\ n_{c,E}^{G,\sigma} = \frac{m_c}{2\pi\hbar^2} \times C_c^\sigma \int_0^\infty E\ e^{-(E-\bar{E}_c^\sigma)^2/\Delta_E^2}\ dE\ . \tag{4.6}$$

Integrating by parts and using the following definition of the error function

$$\mathrm{erfc}(x) = \frac{2}{\sqrt{\pi}} \int_x^\infty e^{-u^2}\ du\ , \tag{4.7}$$

leads to:

$$E_{tot,c}^{G\sigma} = \Delta_E\ \sqrt{\frac{2}{\pi}} \times \frac{N_c^\sigma e^{-\bar{E}_c^\sigma/2\Delta_E^2}}{\mathrm{erfc}(-\bar{E}_c^\sigma/\Delta_E^2\sqrt{2})}\ + \bar{E}_c^\sigma\ N_c^\sigma\ . \tag{4.8}$$

Eq. (4.3) has to be solved numerically using Eq. (4.8) as the initial condition. To evaluate the effective carrier temperatures at each point in time, we use the time evolution of the nonequilibrium energies $E_{tot,c}^\sigma(t)$. We calculate first the quasi-equilibrium energies as an explicit function of temperature $E_c^{eq,\sigma}(T_c^\sigma)$; then, equating $E_c^{eq,\sigma}(T_c^\sigma)$ and the nonequilibrium energies $E_{tot,c}^\sigma(t)$ gives the effective temperature T_c^σ at the time t:

$$E_c^{eq,\sigma}(T_c^\sigma) = \frac{m_c}{2\pi\hbar^2}\ \left(e^{2\pi\hbar^2\beta_c^\sigma N_c^\sigma/m_c} - 1\right)\ \times \int_0^\infty \frac{E\ dE}{e^{\beta_c^\sigma E} + e^{2\pi\hbar^2\beta_c^\sigma N_c^\sigma/m_c} - 1}\ , \tag{4.9}$$

where $\beta_c^\sigma = 1/k_B T_c^\sigma$.

The initial temperatures T_c^σ depend on the characteristics of the pump pulse:

[1] We assume that the initial nonequilibrium distribution is Gaussian as defined later in section 4.3, Eq. (4.19).

energy E_{pump}, width Δ_E and intensity, i.e. number of carriers N_c^σ created.

The knowledge of the distributions $n^\sigma_{c,\mathbf{k}}(t)$ will allow us to evaluate the time evolution of the Pauli blocking factor entering the equations of motion for the interband polarizations in Eq. (3.3) that will be solved in the next chapter. It will also be used to calculate the time evolution of the plasma screening in order to evaluate the Coulomb matrix elements as the electron-hole plasma evolves.

4.2.3 Time evolution of the plasma screening

As the plasma temperature and the carrier densities evolve, the plasma screening changes. In chapter 2 and in Appendix A, detail is given on how the density and temperature dependent screening can be evaluated in a quasi-equilibrium electron-hole system. In chapters 2 and 3, we chose to work with the static plasmon-pole approximation as it is an approximation which is good enough to obtain qualitative results. In this chapter we are concerned with the time evolution of the electron-hole plasma and we need to find a simple way to evaluate it in a nonequilibrium situation. As the Lindhard formula given in Eq. (2.10) is valid for both equilibrium and nonequilibrium situations, it is our starting point:

$$\epsilon_q(\omega) = 1 - V_q \sum_{\sigma,\mathbf{k}} \sum_c \frac{n^\sigma_{c,\mathbf{k}-\mathbf{q}} - n^\sigma_{c,\mathbf{k}}}{\hbar(\omega - i\delta + E^\sigma_{c,k-q} - E^\sigma_{c,k})} \,. \tag{4.10}$$

To ease notations we do not explicitly denote the time dependence of the various physical quantities above defined in this chapter and in chapter 2. Again, we have to simplify the above expression as it is not practical to use for numerical purposes because of its continuum of poles. As in chapter 2, we choose to work in the long wavelength limit $q \to 0$. Detail of this calculation can be found in Appendix A. Nevertheless, we need to emphasize a particular step of the calculation which will help in treating the nonequilibrium problem. From Eq. (A.18) one obtains:

$$\epsilon(q \to 0, \omega) \approx 1 + \frac{V_q}{\hbar\omega} \sum_{\sigma,\mathbf{k}} \sum_c \sum_i q_i \frac{\partial n^\sigma_{c,\mathbf{k}}}{\partial k_i} \times \left(1 + \frac{\hbar}{m_c\omega}\, \vec{k}\cdot\vec{q}\right). \tag{4.11}$$

The important point here is that the term proportional to $\sum_{\mathbf{k}} \partial n^{\sigma}_{c,\mathbf{k}}/\partial k$ vanishes because it yields the value of the distribution function at $k \to \infty$ even if it is a nonequilibrium function, so Eq. (4.11) becomes:

$$\epsilon(q \to 0, \omega) = 1 + \frac{V_q}{\hbar\omega} \sum_{\sigma,\mathbf{k}} \sum_{c} \sum_{i} q_i \frac{\partial n^{\sigma}_{c,\mathbf{k}}}{\partial k_i} \times \frac{\hbar}{m_c \omega} \vec{k} \cdot \vec{q}. \tag{4.12}$$

Leading further the calculations as in Appendix A yields:

$$\epsilon(q \to 0, \omega) = 1 - \frac{V_q}{\omega^2} \sum_{\sigma,\mathbf{k}} \sum_{c} \sum_{i,j} q_i q_j \int \frac{d^2k}{4\pi^2 m_c} n^{\sigma}_{c,\mathbf{k}} \frac{\partial k_i}{\partial k_j} , \tag{4.13}$$

which finally gives:

$$\epsilon(q \to 0, \omega) = 1 - V_q \frac{q^2}{\omega^2} \sum_{c} \frac{N_c}{m_c}. \tag{4.14}$$

From the above equations it appears that the time dependence of the distribution functions $n^{\sigma}_{c,\mathbf{k}}$ due to the relaxation process does not affect the expression of $\epsilon(q \to 0, \omega)$: it has the same form as in quasi-equilibrium calculations (see Eq. (A.22)). So, to treat the nonequilibrium problem for the screening, we can choose to calculate the screening from the quasi-equilibrium formulas as derived in Appendix A and given in chapter 2. The time dependence of $\epsilon(q \to 0, \omega)$ is contained in N_c. Together with the definition of the bare 2D Coulomb potential in a quantum well (i.e. including the form factor f_q) given by Eq. (2.26), Eq. (4.14) also defines the plasma frequency $\omega_{pl}(q)$:

$$\omega^2_{pl}(q) = \sum_{c} \omega^2_{pl,c}(q) = \frac{e^2}{2\epsilon} q f_q \sum_{c} \frac{N_c}{m_c}. \tag{4.15}$$

As in chapter 2, the plasma screening is evaluated within the static plasmon-pole approximation. The modified 2D effective plasmon frequency is:

$$\omega^2_q = \sum_{c} \sum_{\sigma} \left[\frac{e^2}{2\epsilon} q f_q \frac{N^{\sigma}_c}{m_c} \left(1 + \frac{q}{f_q \kappa^{\sigma}_c} \right) \right] + \sum_{c} \frac{N_c}{N} \frac{C}{4} \left(\frac{\hbar q^2}{2m_c} \right)^2 , \tag{4.16}$$

where the screening wavenumber, κ_c^σ, is given by:

$$\kappa_c^\sigma = \frac{m_c^2}{4\pi\epsilon\hbar^2}\ n_{c,k=0}^\sigma = \frac{m_c^2}{4\pi\epsilon\hbar^2}\ \left(1 - \exp\ (-2\pi\hbar^2\beta_c^\sigma N_c^\sigma/m_c)\right)\ . \tag{4.17}$$

Eq. (4.10) is the generalization of Eq. (2.13) to the case of an electron-hole plasma composed of six spin-polarized carrier gases. The dielectric function ϵ_q in the static plasmon-pole approximation:

$$\epsilon_q^{-1} = 1 - \frac{\omega_{pl}^2(q)}{\omega_q^2}\ . \tag{4.18}$$

As already discussed in chapter 2, the static plasmon-pole approximation only gives good qualitative results to explain the density dependent band-gap renormalization. Therefore, we have to bear in mind that the use of this screening model leads to an overestimation of the band-gap shrinkage.

4.3 Initial conditions for the electron/hole plasma

We now turn to the three pump-probe polarisation configurations and the initial carrier distributions they produce as the starting point for the solution of Eqs. (4.1):

- opposite circular polarisations (OCP) for which the pump and the probe beams are both circularly polarised but in opposite senses.
- same circular polarisations (SCP) for which the pump and the probe beams are circularly polarised in the same sense.
- same linear polarisations (SLP) for which the pump and the probe beams are both linearly polarized.

4.3.1 Selection rules for optical transitions

Depending on the pump-probe polarisation configuration, we generate different couplings between the ground state and the various spin-states $|J, m_J\rangle$. In our analysis we include the two-fold degenerate conduction band $|1/2, 1/2\rangle_e$ and $|1/2, -1/2\rangle_e$, the

two-fold degenerate heavy hole band $|3/2, 3/2\rangle_{hh}$ and $|3/2, -3/2\rangle_{hh}$ and the two-fold degenerate light hole band $|3/2, 1/2\rangle_{lh}$ and $|3/2, -1/2\rangle_{lh}$. The selection rules for zinc blende semiconductors are used [76] and the relative populations generated by optical pumping in the continuum are as depicted in Fig. 4.1:

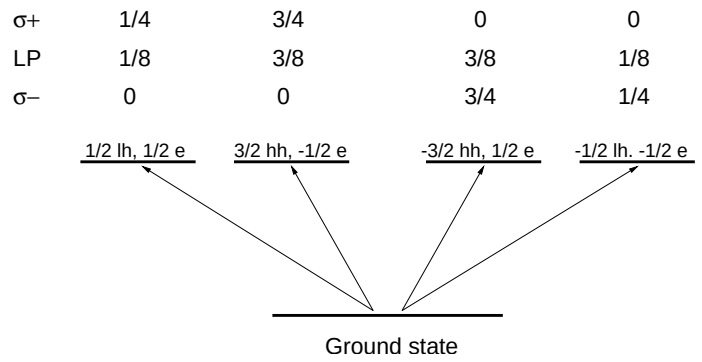

Figure 4.1: Selection rules for optical transitions achieved with polarised pump light.

The ratio of 3 between the populations created from the heavy hole and light hole transitions comes from the ratio of the dipole matrix elements which describe the relative strength of these optical transitions [76].

4.3.2 The Gaussian hot carrier distribution

The optical pumping creates a population of hot carriers. The initial nonthermal distribution is assumed to be Gaussian in energy[2] reflecting the spectral width and the location of the pump pulse:

$$n^{\sigma}_{c,\mathbf{k}}(t=0) = n^{G,\sigma}_{c,E_{\mathbf{k}}} = C^{\sigma}_{c} \times \exp^{-(E^{\sigma}_{c,\mathbf{k}} - \bar{E}^{\sigma}_{c})^2/\Delta^2_E} \ . \tag{4.19}$$

C^{σ}_{c} are the normalization coefficients for each energy distribution of each type of carriers in each spin-state and the mean values of the energies $\bar{E}^{\sigma}_{c}$ are evaluated from the experimental value of the photon energy of the pump beam, E_{pump}: for the vertical transition from the heavy hole band to the conduction band, conservation of energy gives:

[2]This means that it is not Gaussian in terms of wave-vector **k**.

$$E_g + \frac{\hbar^2 k^2}{2m_e} + \frac{\hbar^2 k^2}{2m_{hh}} = E_{pump} \ . \tag{4.20}$$

From the knowledge of E_{pump}, it is straightforward to calculate the corresponding wavenumber $k = k_{pump}$:

$$\hbar k_{pump} = \sqrt{2\mu_{e,hh}\left(E_{pump} - E_g\right)} \ , \tag{4.21}$$

where $\mu_{e,hh}$ is the reduced mass of the heavy hole - electron system. Then:

$$\begin{cases} \bar{E}_e^{\sigma'} = \hbar^2 k_{pump}^2 / 2m_e \\ \bar{E}_{hh}^{\sigma} = \hbar^2 k_{pump}^2 / 2m_{hh} \ . \end{cases} \tag{4.22}$$

As heavy holes are heavier than electrons, the energy of the initial hot electron gas is bigger than the initial hot heavy hole gas energy. In the case of a vertical transition from the light hole band to the conduction band, the evaluation of k_{pump} gives:

$$\hbar k'_{pump} = \sqrt{2\mu_{e,lh}\left(E_{pump} - E_g - \Delta E_{cs}\right)} \ , \tag{4.23}$$

according to Eq. (2.70), and:

$$\begin{cases} \bar{E}_e^{\sigma} = \hbar^2 k_{pump}'^2 / 2m_e \\ \bar{E}_{lh}^{\sigma} = \hbar^2 k_{pump}'^2 / 2m_{lh} \ . \end{cases} \tag{4.24}$$

where $\mu_{e,lh}$ is the reduced mass of the light hole - electron system. Here, even if the effective mass of the light hole is smaller than the effective mass of the heavy hole, the initial hot light hole gas is colder than the initial hot heavy hole gas. This is due to the strain and confinement energies ΔE_{cs} which lowers the light holes kinetic energies.

Knowing the mean energies $\bar{E}_c^{\sigma}$, we can now evaluate the normalization coefficient C_c^{σ} of the above Gaussian distributions. Denoting N_c^{σ} the 2D density of carriers of type c in the spin-state σ, we have to evaluate C_c^{σ} such that:

$$N_c^\sigma = \sum_{\mathbf{k}} n_{c,E_\mathbf{k}}^{G,\sigma} \ . \tag{4.25}$$

Approximating the above discrete sum by a 2-dimensional integral and performing the angular integration yields:

$$N_c^\sigma = \frac{m_c}{2\pi\hbar^2}\, C_c^\sigma \int_0^\infty e^{-(E-\bar{E}_c^\sigma)^2/\Delta_E^2}\, dE \ . \tag{4.26}$$

Using the definition for the error function, Eq. (4.7), that we substitute into Eq. (4.26) after making the appropriate change of variables yields:

$$C_c^\sigma = \frac{2\hbar^2\sqrt{2\pi}}{m_c\Delta_E} \frac{N_c^\sigma}{\mathrm{erfc}(-\bar{E}_c^\sigma/\Delta_E\sqrt{2})} \ . \tag{4.27}$$

Note that C_c^σ are not only defined by the above equation. Indeed, as we deal with distribution functions, their maximum which is reached for $E_{c,\mathbf{k}}^\sigma = \bar{E}_c^\sigma$ has to be 1/2. This creates the following constraint on the value of the normalization coefficients:

$$C_c^\sigma \leq 1/2 \ , \tag{4.28}$$

which means that for a given pump energy E_{pump} and a given pulse width Δ_E there is a maximum density N_c^σ that can be reached.

In the SLP situation, electrons with a given spin σ are created from both the light and heavy hole transitions. So, the initial distribution for the spin-polarised electron gases in the SLP is the sum of two Gaussian distributions, each centered appropriately.

4.4 Numerical results

In this section, we are concerned with the interplay between the various dynamical processes included in our model and their influence on the time evolution of the carrier density, plasma energy and temperature. We present results where the ex-

citations have been performed either by circularly polarised pump light CP or by linearly polarised light LP. These two cases are sufficient to describe SLP, OCP and SCP pump-probe experiments.

The lattice temperature is taken to be $T_{lat} = 77$ K[3] and the initial plasma density $N = 3 \times 10^{11}\text{cm}^{-2}$. The location of the pump pulse is 30 meV above the bandgap. The material parameters used are those given in the Introduction. The phenomenological parameters entering Eqs. (4.22) are: $\tau_{eq} = 0.1$ ps, $\tau_{cool} = 1$ ps, $\tau_{therm} = 1$ ps, $\tau_{sf} = 30$ ps, $\tau_{rad} = 1.6$ ns, $\tau_{nr} = 30$ ps and $\tau_{lh} = 0.5$ ps. The three parameters τ_{eq}, τ_{cool} and τ_{therm} are chosen according to Ref. [6]. The radiative recombination time, τ_{rad}, is evaluated from Eq. (D.13). The nonradiative recombination time is taken from the experimental exciton bleaching dynamics that is shown in chapter 5, Fig. 5.2. No experimental results are available yet to give us an estimate for the light hole scattering time, τ_{lh}, but based on the light hole exciton peak bleaching dynamics, we find it to be very fast. The spin-flip times have been chosen comparing numerical results with experimental data shown in chapter 5, Fig. 5.2.

Before presenting and discussing the numerical results, it is useful to describe the numerical procedure used to calculate the time evolution of the electron/ hole plasma thermodynamics. This is depicted in Fig. 4.2.

The initial plasma density N, the pumping energy E_{pump} as well as the Gaussian distribution, Eq. (4.19), define the initial conditions that are fed in the computer code. Depending on the polarization configuration we impose, the spin-polarized gases are populated according to the selection rules shown in Fig. 4.1. Then, the initial energy of each carrier gas, $E^{G\sigma}_{tot,c}$, is calculated as in Eq. (4.8). Equating $E^{G\sigma}_{tot,c}$ and $E^{eq,\sigma}_{c}(T^{\sigma}_{c})$ in Eq. (4.9) yields the initial effective carrier gas temperatures T^{σ}_{c}. The next step consists then of solving the system of coupled equations, Eq. (4.1), to find the values of the carrier distributions and the carrier densities at the next step

[3] As discussed in chapter 3, we find in materials with strong Coulomb effects such as $ZnSe$, that strongly degenerate cases at 4 K are numerically prohibitive due to the large number of k-states required around the Fermi energy.

in time.

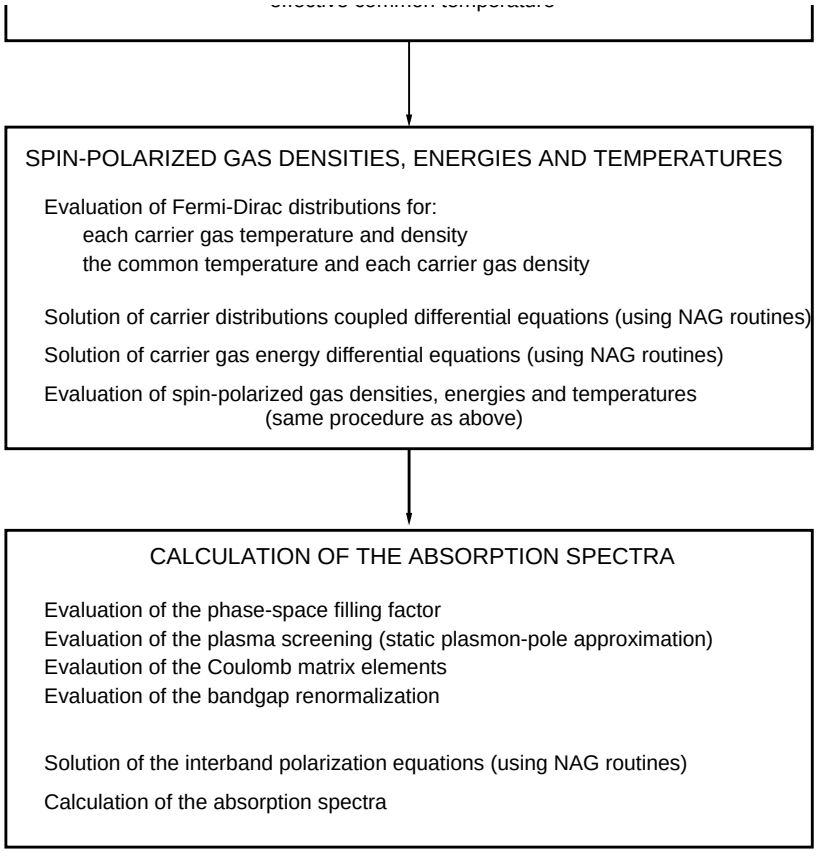

Figure 4.2: Flow chart describing the numerical procedure used to calculate the time evolution of the distribution functions, the plasma density, energy and temperature in order to compute the phase-space filling factor and the plasma screening.

Solving Eq. (4.3) gives the carrier gas energies and hence the temperatures using Eq. (4.9). The plasma screening and the Pauli blocking are then computed and used to solve the interband polarization equations, Eq. (2.71). The solutions of Eq. (2.71)

as a function of the pump-probe delay, will be calculated and discussed in the next chapter.

4.4.1 Time evolution of the carrier densities

First we study the time evolution of the carrier densities obtained solving Eqs. (4.1) with $N = 3 \times 10^{11}\text{cm}^{-2}$, the pumping energy $E_{pump} = 2.69$ eV, and shown on Fig. 4.3:

Electrons: the processes responsible for the change in population are the electron spin-flip and the recombination. The population of spin down electrons decreases while the population of electrons with opposite spin increases. The carrier spin-flip process tends to create equal spin populations over a time scale given by $\tau_{sf}^{e} = 30$ ps. Then, the recombination which occurs on the same time scale given by $\tau_{nr} = 30$ ps becomes dominant and drives both populations towards zero. That is the reason why the initially less populated electron gas exhibits a maximum at early times (10 ps). Note that in the SLP case, the spin-flip process has no effect on the dynamics of the electron densities. Hence, the only contributor to the density decay in the SLP situation is recombination. Also note that the radiative recombination too slow (1.6 ns) to have much influence on the fast population dynamics.

Heavy holes: similar comments apply for the heavy hole population dynamics as above with $\tau_{sf}^{hh} = 30$ ps. However, the fast intersubband scattering that drives the light holes into the heavy hole band on a time scale given by $\tau_{lh} = 0.5$ ps has to be considered here. That explains the fast initial rise of both heavy hole densities, before they start decaying. Note that the initial spin down heavy hole density is zero, unlike the electrons whose populations in both spin states is non-zero from the beginning because of optical transitions from both the heavy and light hole bands.

Light holes: the time evolution of the light hole populations can also be described as the electron ones with $\tau_{sf}^{lh} = 30$ ps. However, as in the case of the heavy

holes, one has to consider the intersubband scattering. As it is a very fast process, the population of light holes decreases on a very short time scale given by $\tau_{lh} =$ 0.5 ps. After one picosecond the light hole density is negligible (but non-zero as heavy holes still scatter into the light hole band). Note that in the case of the spin down light hole gas, the population always remains very low: the spin-flip time is comparatively too long to make any significant change.

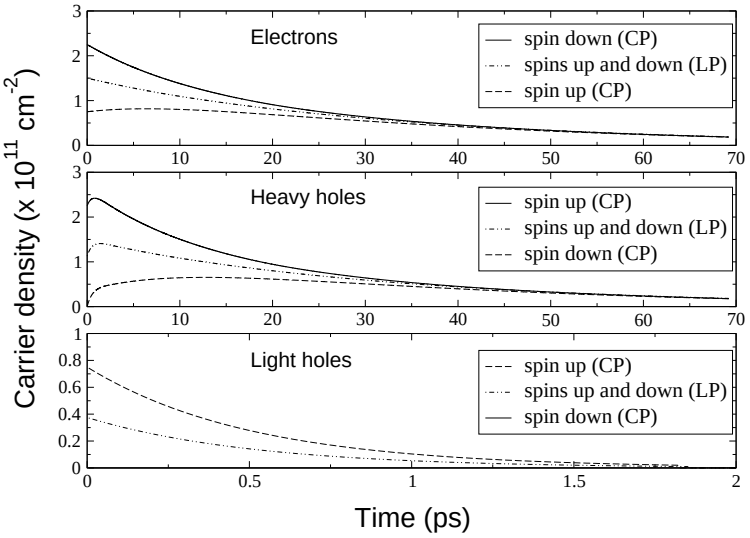

Figure 4.3: Time evolution of the spin-polarized gases populations created by spin-selective excitation. Note the short time scale for the light hole density decay, and for the electron spin populations to equilibrate.

4.4.2 Time evolution of the plasma energy

The solutions of Eq. (4.3) are shown in figures below for each spin-polarized gas.

Electrons: the initial total energy of the spin down electron gas in the CP case corresponds to a temperature above the lattice temperature and hence is a decreasing function of time because of the cooling process that occurs on a time scale given by $\tau^e_{cool} = 1$ ps. One can observe that the energy of the electron gas with opposite spin is an increasing function of time before cooling down to the lattice energy. It is due to the thermalisation process between carriers of different types and also to the fact that the density increases over the same amount of time because

of the spin-flip , and hence increases the total energy. In the LP case, we only observe a cooling as the spin-flip has no influence on the time evolution of the densities.

Heavy holes: the initial rise of the carrier densities for both heavy hole gases because of the light hole scattering, influences the behaviour of the energy which is an increasing function of time at early times. The thermalisation process is also responsible for this rise as the initial hole gases energies are below the spin down electron gas energy. In the case of the spin down heavy hole gas, the increase occurs on a much longer time scale than for the opposite spin heavy hole gas. This is due to the spin-flip process that increases the population for the spin up heavy hole gas in the CP case.

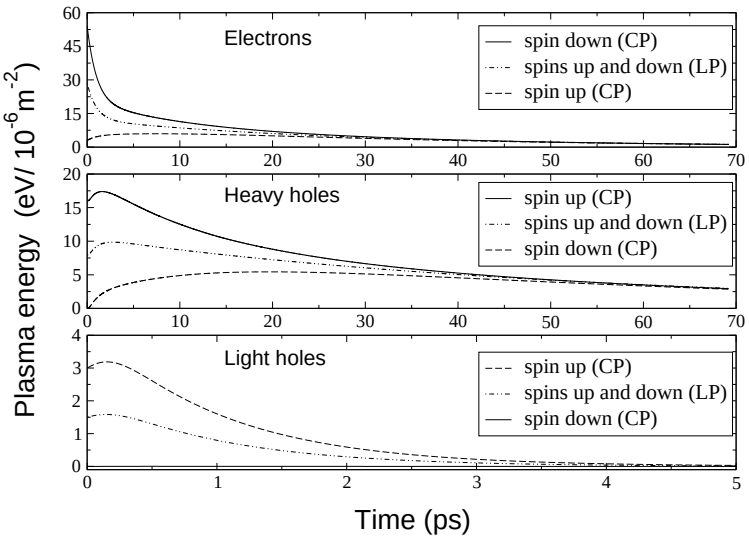

Figure 4.4: Time evolution of the spin-polarized gases energy loss. Note the very short time scale for the light hole gases energy loss.

Light holes: the initial rise of the energy for the light hole gases is only due to the thermalisation process. As the light hole density decay is fast, it only takes a few picoseconds for the light hole gas energy to become negligible. The population of the spin down light hole gas remains very low, so does the energy.

4.4.3 Time evolution of the plasma temperature

The temperatures computed from Eq. (4.9) are shown in figures below for each spin-polarized gas.

Electrons: the time evolution of the electron temperatures follows exactly the time evolution of the electron gas energies, but converges fast towards the lattice temperature whereas the electron energies keep decreasing. This is due to the fact that the electron densities also decrease via recombination, keeping the average electron kinetic energy constant.

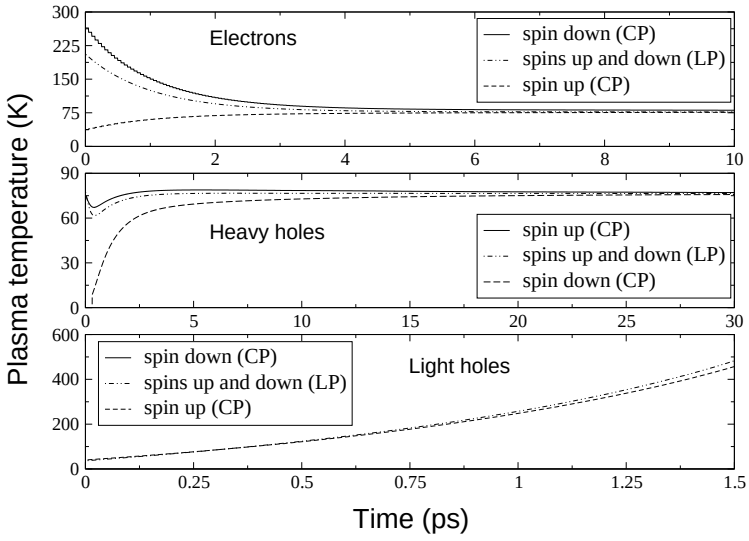

Figure 4.5: Time evolution of the spin-polarized gases temperatures. Note the very short time scale for the light hole temperature evolution.

Heavy holes: the heavy hole gas energies increase at very early times, so do the densities because of the light hole scattering. In the CP case, for the spin down heavy hole gas, despite this increase in energy, the average heavy hole kinetic energy decreases. Hence the effective temperature decreases. Then because of the thermalisation with the electrons and the lattice, the temperature starts increasing. For the spin up heavy hole gas, we observe a monotonical increase towards the lattice temperature as it gains energy from the thermalisation processes with the other carriers and the lattice. However, as the densities starts decreasing, the heavy holes energy also start decreasing. But, as in the case of electrons, there is compensation

between the energy loss and the density decay that makes the average heavy hole kinetic energy constant when it reaches the lattice temperature.

Light holes: the light hole density decay is so fast compared to the plasma cooling that the average light hole kinetic energy keeps increasing and the light hole gases temperatures go beyond the lattice temperature. In fact, the light hole gases have no time to reach the quasi-equilibrium with the lattice. We stopped calculating the light hole gas effective temperatures when their population is small enough and their temperature high enough to have no influence on the absorption spectra.

4.4.4 Time evolution of the plasma screening

As discussed in section 4.2.3, we can make use of the quasi-equilibrium formulas to evaluate the time evolution of the plasma screening in the long wavelength limit. The inverse screening lengths for each carrier gas are computed from Eq. (4.14) at each time step, after having calculated $T_c^\sigma(t)$ and $N_c^\sigma(t)$. As already mentioned in chapter 2, the screening parameter κ is a function of the plasma temperature and density, so its time evolution reflects the interplay between both of them.

Before discussing in detail the time evolution of each spin-polarized gas inverse screening length shown in Fig. 4.7, we look first at the total inverse screening length shown in Fig. 4.6. The total screening length, κ, is the sum of each contribution, κ_c^σ, described in Fig. 4.7.

The screening is not spin-dependent so the CP case describe both SCP and OCP configurations. The fast decay at early times is due to the heating of the heavy hole gas, despite the cooling of the electron gas and the light hole scattering into heavy holes, as it contributes the most to the total screening. Then, because of the slower recombination which becomes the dominant process, the plasma screening decreases with the plasma density.

Electrons: the initial spin down electron density is three times larger than the initial spin up electron density; but, as its initial temperature is also much larger

(five times), the screening due to the the spin down electron gas, is smaller. Then, because of the fast thermalization and cooling (a few picoseconds), the spin down electron gas contribution to the plasma screening becomes more important as its density remains the largest. The initial temperature of the spin up electron gas is below the lattice temperature, so as time passes, the spin up electron gas is heating up. The spin-flip process is a too slow process (30 ps) to rapidly increase the spin up electron population, so we just observe a decay of the screening parameter, initially reflecting the heating and the further enhanced by the recombination process that occurs on the same time scale as the spin-flip. In the LP case, the spin-flip plays no role in the time evolution of the screening parameter, so we just observe an initial increase due to the cooling process followed by a decay due to the recombination.

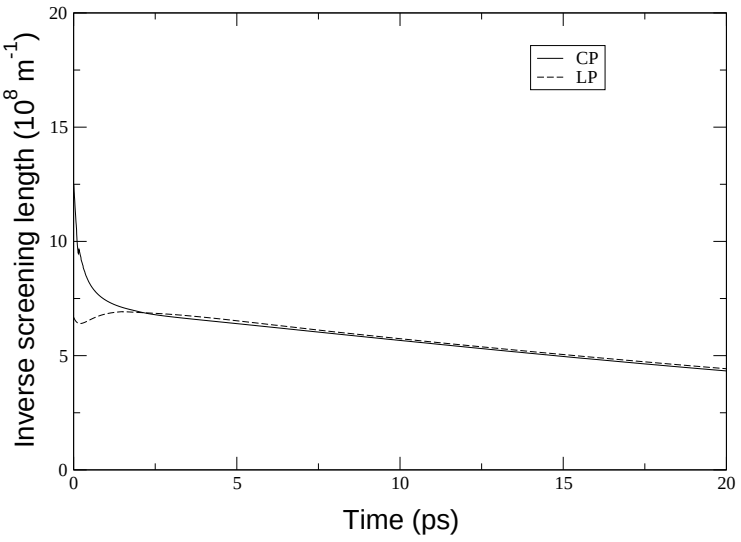

Figure 4.6: Time evolution of the inverse screening length.

Heavy holes: the values of the screening lengths in the case of the heavy holes are larger than the electron ones as the heavy hole gases are much colder and their effective mass is heavier than the electron one. The time evolution for the heavy hole contribution to the plasma screening is very similar to the electron one. The main difference comes from the fact that light holes scatter very fast into the heavy hole band (0.5 ps time scale). That explains why the maximum observed for the spin up heavy hole screening parameter occurs earlier than the one for the spin

down electron one. The spin-flip has no influence in the LP case and the time evolution of the screening parameter is driven by the recombination on a longer time scale.

Light holes: the time evolution of the light hole screening parameters is only driven by the fast scattering into the heavy hole bands and the other dynamical effects (thermalization, cooling, spin-flip, recombination) have no noticeable influence as they are slower processes. The spin down light hole screening parameter (CP case) is always negligible as the spin down light hole density is always very small. Note that the light hole contribution to the screening is zero after 2 ps.

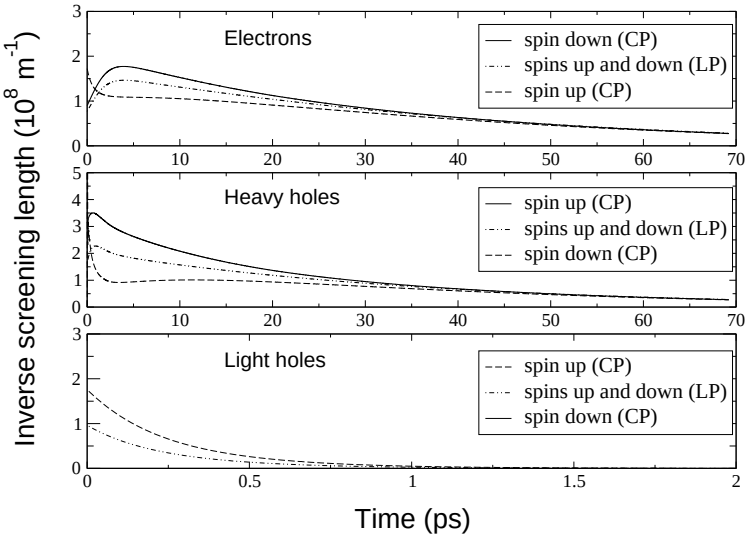

Figure 4.7: Time evolution of the inverse screening lengths for each spin-polarized gas. Note the very short time scale for the light hole screening evolution.

4.5 Conclusions

In this chapter we developed a simple model to describe the time evolution of the quasi-2D electron/hole plasma. We included several dynamical effects: relaxation of the carrier distributions, thermalization, plasma cooling, carrier spin-flip, recombination (radiative and nonradiative) and light hole scattering into heavy holes. A full microscopic treatment of all these effects is computationally prohibitive, and we chose a phenomenological approach using rate equations. We described the time

dependence of the density, energy and temperature of each spin-polarised gas and obtained insight in the interplay between the processes mentioned above. We also found that we could address the problem of the time dependence of the plasma screening in a simple fashion, using quasi-equilibrium formulas in the long wavelength limit. In the next chapter, we shall compute the absorption spectra as a function of the pump-probe delay, solving the interband polarization equation, Eq. (2.71), together with Eqs. (4.1). The results shown and discussed in this chapter will help in describing and explaining the dynamics of the excitonic peaks in the next chapter.

Chapter 5

Ultrafast pump-probe dynamics in semiconductor quantum-wells

5.1 Introduction

From an experimental point of view, one can investigate the optical properties of semiconductors by exciting carriers (via optical pumping or carrier injection) and measuring the absorption of a subsequent probe pulse. By comparing with the linear absorption spectrum, one obtains information on the influence of the excitations on the absorption phenomenon and insight into the electronic and optical properties of the electron-hole plasma. The interpretation of experimental results is however non-trivial given the substantial influence of Coulomb and many-body effects which give rise to a rich variety of broadening and energy renormalizations. Moreover, the time evolution of the initial electron/hole plasma makes the whole problem challenging, both theoretically and numerically. In this chapter, we use the model developed and discussed in chapter 4 to describe the influence of the nonequilibrium electron/hole system on the absorption spectra.

As already discussed in the previous chapter, the orders of magnitude of some of the scattering times describing the dynamical processes included in our model are known (see Ref. [6], page 282) or can be evaluated (τ_{rad} is calculated in Appendix D, Eq. (D.13)). However, we do not know how fast the light holes scatter into the heavy hole band, and the spin-flip times are also poorly known despite numerous studies under various conditions [57, 58, 59, 60, 61, 62, 63, 64, 65, 66, 67]. One of our aims with our model would be to extract these times from the available experimental data comparing the computed exciton resonances bleaching and shift dynamics with experimental results. We currently have only one set of reliable experimental results

for the heavy hole exciton dynamics (see Figs. 5.1 and 5.2).

Detail of experiments are given in the next section, but we point out that they have been performed using a $ZnSe/ZnCdSe$ sample cooled down at a temperature of 4 K. In chapter 3, we discussed the numerical problems that arise when numerical calculations are performed in the highly degenerate limit. Here, to obtain reliable numerical results, the absorption spectra are computed at $T_{lat} = 77$ K. This makes the comparison between the calculations and experiments obviously more difficult as it is not possible to assess the difference between "good numerical results" at 4 K and the reliable results at 77 K. Nevertheless, we assume that, even if the results are quantitatively different, the qualitative behaviour is not much affected.

This chapter is organised as follows: the object of section 2 is to give a brief overview of the pump and probe experiments carried out at Heriot-Watt University[1]. The available experimental results will help in extracting an order of magnitude for the carrier spin-flip times in section 3, where we compare experiments with our model. We discuss the exciton dynamics, i.e. bleaching and energy shift as functions of the pump-probe delay, considering the results of chapter 4.

5.2 Ultrafast pump and probe experiments

A femtosecond laser system consisting of a Beamlok Argon ion (Ar^+) laser, a Tsunami mode-locked Ti:Sapphire laser, a Spitfire pulsed Ti:Sapphire RGA and an ultrafast kHz optical parametric amplifier (OPA), has been used for the generation of the ultrafast pump pulses. The Ar^+ laser and the Merlin laser were the excitation sources for the Tsunami laser and the Spitfire amplifier respectively. The Tsunami output was fed to the Spitfire where it was temporally stretched, amplified and finally temporally compressed. The Spitfire output provided the pump beam for the frequency conversion processes in the OPA. The overall system was capable of delivering a 1kHz train of $\sim$ 150 fs pulses and the wavelength was tuned at 459 nm ($\sim$ 2.69 eV). For the generation of the white light continuum (WLC), $\sim$ 5%

[1]The experiments were performed by George Papageorgiou in the Physics Department.

of the Spitfire output ($\lambda = 800$ nm) was focused on a 10 mm thick quartz cuvette containing de-ionised water. The pump pulse was used to excite the semiconductor sample, which was mounted on the cryostat and cooled at 4 K. The pump power, and therefore the carrier density, could be controlled with the use of a neutral density filter. The pump pulse power incident in the cryostat was 0.06 mW. The changes induced in the transmitted probe pulse energy were measured as a function of the time delay between the pump and probe pulses, with an optical spectrum multi-channel analyser. A small portion of the WLC was selected prior to falling onto the sample using a glass microscope slide, in order to monitor its stability. The spot size radius of the probe beam was 190 μm and it was considerably smaller than that of the pump in order to probe a region of uniform photoexcited density. Both pump and probe beams were circularly polarized and independently controllable by $\lambda/4$ plates. Opposite circular (OCP) and same circular polarization (SCP) configurations were employed. The time resolution was provided by delaying the WLC pulses to the pump pulses relatively. The experimental work has been performed on a $ZnSe/ZnCdSe$ multiple quantum well structure of twenty 4nm-wide wells grown by molecular beam epitaxy on $GaAs$ substrate. The 20% Cd content in the wells produces light hole heavy hole exciton splitting of more than 30 meV.

The absorption spectra, Fig. 5.1, show that at early times, both the heavy hole and light hole exciton peaks are bleached but not much shifted. In the SCP case, the heavy hole exciton peak is more bleached because of the Pauli blocking effect that reduces the oscillator strength. In contrast, the light hole exciton peak is more bleached in the OCP case. The detailed description and interpretation of these experimental results will be given below with our numerical analysis. Increasing the delay between the pump and the probe beams shows that many dynamical processes occur in the electron/hole plasma, and change the shape of the absorption spectra. The dynamics of the absorption spectra is shown in Fig. 5.2.

Experimental data show an overall decay of the exciton peak bleaching as well as a convergence between the OCP and the SCP curves. They also show an initial blue

shift at early times and an energy shift that brings the resonances back to the linear spectrum exciton resonance. The energy shifts exhibits the same type of behaviour as the exciton bleaching: the OCP and SCP curves converge on a 30 ps time scale.

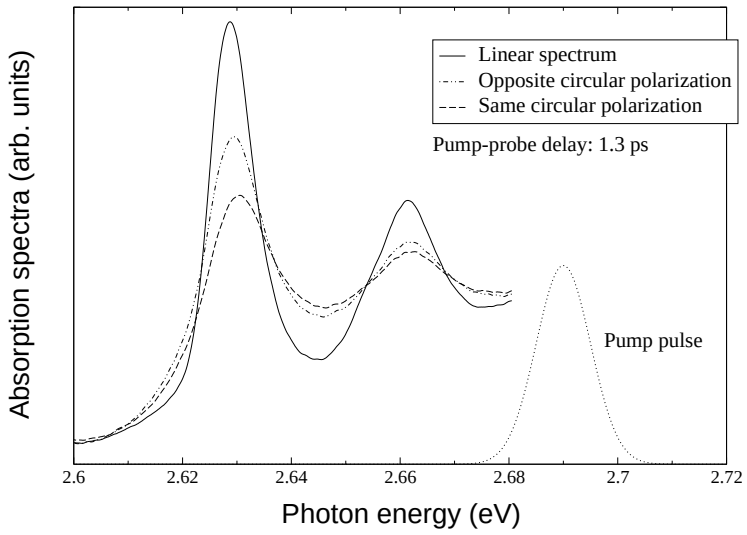

Figure 5.1: Measured absorption spectra. Comparison between the OCP and the SCP absorption.

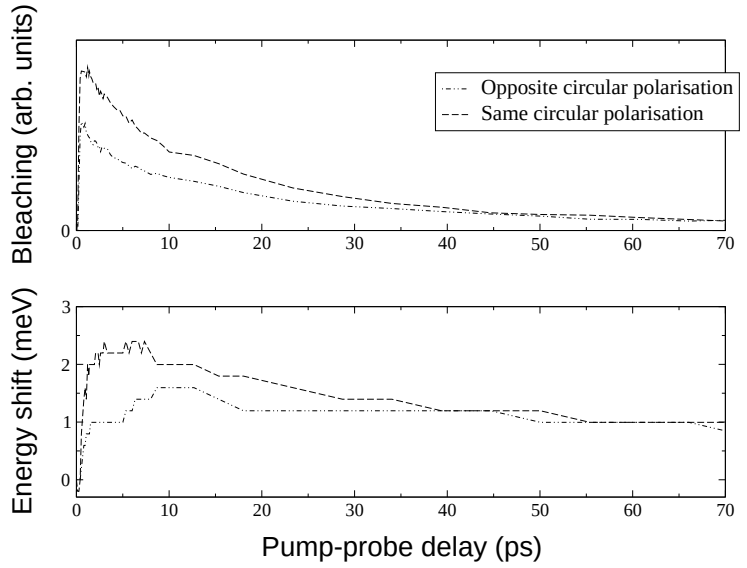

Figure 5.2: Measured absorption spectra dynamics. Comparison between the OCP and the SCP heavy hole exciton peaks bleaching and shift.

5.3 Numerical results

The computer code developed calculates the absorption spectra for various pump-probe delays and three polarization configurations, OCP, SCP and SLP, solving simultaneously Eqs. (2.71), (4.1) and (4.3). In chapter 3, the Coulomb matrix elements were calculated just once as none of the physical parameters entering the problem was varying. Here, the plasma density and temperature evolve very fast, so the Coulomb forces have to be evaluated at each time step. This added to the computation of the time evolution of the plasma density makes the running time long.

5.3.1 Comparison between numerical and experimental results

To describe and explain what we observe, we use the theoretical model presented in chapters 2 and 3, describing the absorption spectra, together with the nonequilibrium electron/hole plasma model developed in chapter 4. To present and discuss the dynamics of the absorption spectra, it is useful to refer to chapter 4 where the time evolution of the electron-hole plasma is described.

We recall the various parameters used: the lattice temperature is taken to be $T_{lat} = 77$ K and the initial plasma density $N = 3 \times 10^{11}\text{cm}^{-2}$. The effective masses we use are $m_e = m_{lh} = 0.15m_0$ and $m_{hh} = 0.6m_0$, where m_0 is the mass of the free electron. The dielectric constant is $\epsilon = 8.8$ and the bandgap $E_g = 2.66$ eV. The phenomenological parameters entering Eqs. (4.22) are: $\tau_{eq} = 0.1$ ps, $\tau_{cool} = 1$ ps, $\tau_{therm} = 1$ ps. These characteristic times only give an order of magnitude and are taken from Ref. [6]. The radiative recombination time $\tau_{rad} = 1.6$ ns is calculated for $ZnSe$ parameters using Eq. (D.13). The nonradiative recombination time τ_{nr} is taken from experiments. The light hole density decay $\tau_{lh} = 0.5$ ps is an arbitrary value that we impose. The spin-flip times, $\tau_{sf} = 30$ ps, have been chosen comparing the present numerical results with experimental data in Fig. 5.1.

The absorption spectra

In this section we present numerical solution of Eqs. (2.71), (4.1) and (4.3). The behaviour of the excitonic peak bleaching as well as their energy shift are discussed. First, we compare the calculated absorption spectra in Fig. 5.3 with experimental data on Fig. 5.1 for a given delay. The optical pumping is set 30 meV above the band edge, in the continuum, thus creating an initial unbound electron/hole plasma.

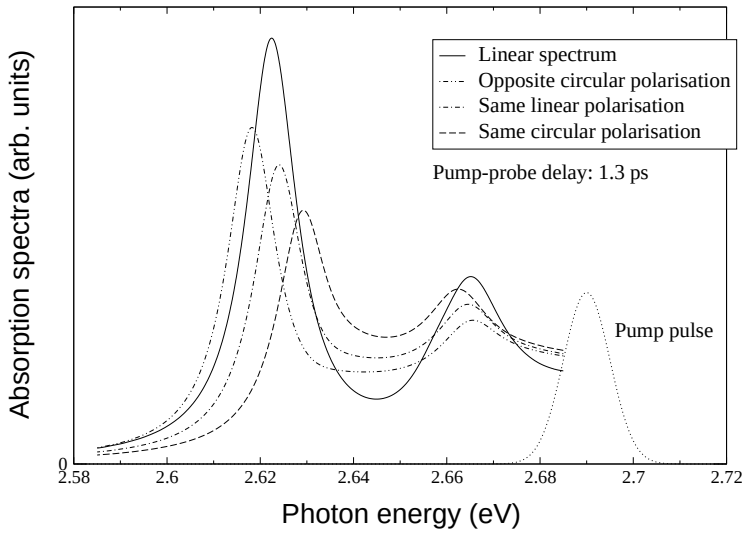

Figure 5.3: Calculated absorption spectra. Comparison between the OCP, SLP and the SCP absorption.

The experimental and numerical spectra look similar, but one can observe a significant redshift of the OCP exciton peak that is not observed in experimental data. This is due to the screening model we use and will discuss in more detail at the end of this section. The heavy hole exciton peak is more bleached in the SCP case than it is in the OCP, and it is more blue shifted. This is due to the phase space filling effect that is more important in the SCP configuration. For the light hole exciton, as in the experiment, we observe the opposite: the OCP light hole exciton peak is more bleached and blue shifted than the SCP light hole exciton peak. This is due to the fact that the spin up electrons excited with the σ^- polarized pump, from the heavy hole transition, occupy states that would be created from a light hole transition with the σ^+ polarized pump. So, in the OCP situation, the reduction of

the oscillator strength due to the phase space filling when one probes the light hole transition is more important than it is in the SCP case. The SLP configuration can be seen as an "intermediate" case between the OCP and SCP.

Heavy hole exciton peak dynamics

As mentioned above, we are concerned with the time evolution of the absorption spectra. So, we have computed both the bleaching and energy shift of the exciton resonances as functions of the time delay between the pump and the probe. The shifts are expressed in meV, and the bleaching is scaled to the maximum of the excitonic resonance of the linear spectrum. The location of the exciton peaks is calculated using a parabolic approximation for each maximum: knowing the highest point and the two nearest points around it, a parabola equation is calculated, from which we obtain the maximum. The maxima are plotted against the pump-probe delay to study the exciton bleaching and energy shift dynamics.

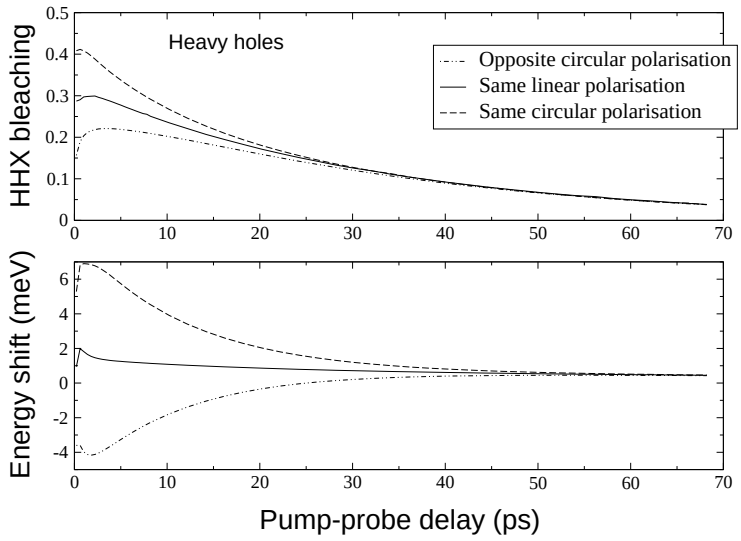

Figure 5.4: Calculated absorption spectra dynamics. Comparison between the OCP, SLP and the SCP heavy hole exciton peaks bleaching and shift.

The numerical results in Fig. 5.4 show a decay of the heavy hole exciton peak bleachings and energy shifts for OCP, SLP and SCP. The three curves converge after a few tens of picoseconds, because of spin-flip and recombination.

OCP: the initial state of the electron/hole plasma, given in Fig. 4.3, shows that the only contribution to the heavy hole exciton bleaching is due to the plasma screening that lowers the Coulomb enhancement. The rapid equilibration of the carrier distributions, together with the plasma cooling contribute to the increase of the bleaching at early times, i.e. less than 5 ps. Although in this case the carrier spin-flip occurs on the same time scale as the recombination, the latter process is dominant, and with the decreasing plasma density, the plasma screening and the phase-space filling become less important. Thus, the amount of bleaching decreases. Regarding the energy shift, the initial heavy hole exciton peak is redshifted. The bandgap renormalisation is not strong enough to compensate for the exciton binding energy which remains large because of the absence of the Pauli blocking effect. The redshift becomes even more important as the plasma screening is increased as a result of the fast light hole scattering. Then, because of the carrier spin-flip and the recombination process, the heavy hole exciton peak shifts towards the blue region and saturates on a longer time scale (from 30 ps). This behaviour is qualitatively different from what we observe in the experiments. This is due to the initial large redshift: if the initial calculated heavy hole exciton peak were not redshifted because of the screening model we use, it would enter the blue region because of increasing phase space filling effect due to spin-flip and plasma cooling; then because of recombination we would observe a shift towards the red region which would explain the presence of a maximum.

SCP: as well as the plasma screening, the phase-space filling contributes to the bleaching of the heavy hole exciton peak in this case. Because of the thermalization and the plasma cooling we observe a slight increase for short pump-probe delays ($\leq$ 2ps) but the carrier spin-flip lowers the amount of bleaching together with the recombination process. In the SCP case both processes contribute to lowering the Pauli blocking effect. The initial SCP heavy hole exciton peak is blue shifted even though the bandgap renormalisation is more important than it is in the OCP case (the exchange term is non-zero). This is due to the fact that the phase-space filling

factor lowers the exciton binding energy in the SCP case. Because of the fast relaxation of the distributions and the plasma cooling, the heavy hole exciton blue shift increases at early times ($\leq$ 2ps), then the spin-flip and recombination make the heavy hole exciton peak shift towards the linear heavy hole exciton peak. In the OCP situation, carrier spin-flip and recombination have competing effects on the exciton peak dynamics, whereas they work together in the SCP case.

SLP: as in the SCP case, plasma screening and phase-space filling contribute to the heavy hole exciton peak bleaching. There is an initial small increase due to the thermalization and the plasma cooling, but after a few picoseconds, the recombination process starts influencing effectively the behaviour of the bleaching. In the SLP case, the spin-flip process plays no role in the dynamics of the bleaching. The behaviour of the energy shift in the SLP case is similar but less dramatic than the OCP one, as it is not influenced by the spin-flip process.

Light hole exciton peak dynamics

In the case of the light hole transitions, the contribution of the light hole population becomes negligible very quickly as the light hole density decays on a very short time scale, $\tau_{lh} = 0.5$ ps. The behaviour of the light hole exciton peak bleaching and shift, shown in Fig. 5.5, is dominated by the electrons and also by the heavy holes because of their contribution to the plasma screening. As mentioned above, the bleaching is here more important in the OCP case than it is in the SCP. Because of the rapid light hole density decay, the bleaching decreases at very early times (less than 1 ps), but it increases shortly after because of the electron thermalization and the plasma cooling. Then, after a few picoseconds, the recombination process dominates the behaviour of the bleaching which monotonically decreases with increasing pump-probe delay. The three curves converge in about 30 ps. As far as the energy shift is concerned, the blue shift quickly becomes very small because of the fast light hole density decay.

As stated earlier, by comparing numerical results with experimental data, we

aim to give an estimate for the spin-flip times. Because of the very fast light hole decay and the lack of experimental data, our results are not conclusive for the light hole spin-flip time: there is no clear signature of the influence of the light hole gas on the absorption spectra that allows us to extract even an order of magnitude.

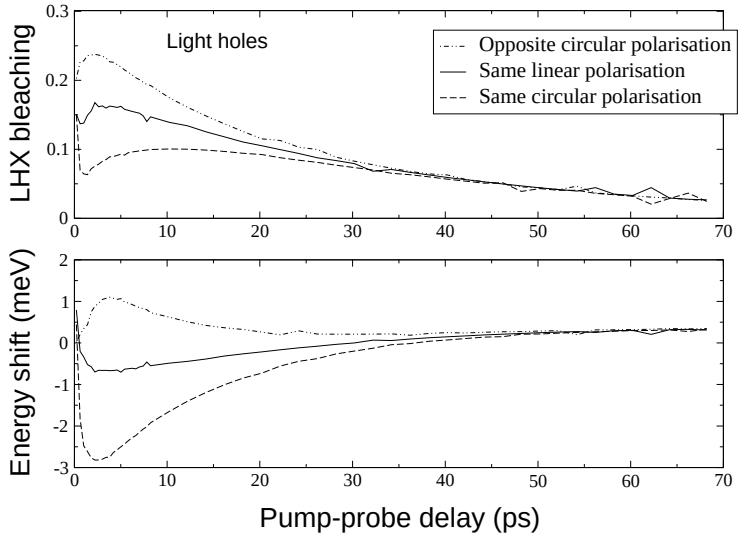

Figure 5.5: Calculated absorption spectra dynamics. Comparison between the OCP, SLP and the SCP light hole exciton peaks bleaching and shift.

The spin-flip times were simply extracted from Figs. 5.1 and 5.2, considering the necessary amount of time to lose the dichroïsm. The value $\tau_{sf} = 30$ ps reflects only the order of magnitude of the time needed for the spin populations to equilibrate. This time scale is comparable to values found for $GaAs$-based semiconductor quantum wells in various conditions [60]. In the next section we study various spin-flip time regimes and compare them. However, as stated above, to evaluate light hole scattering and spin-flip times, more experimental results are needed.

5.3.2 Exploring the parameter space

Comparison between various spin-flip time regimes

In the previous section, the spin-flip times were chosen to be the same for all the carriers. Here we explore two other regimes: $\tau_{sf}^{e} = 1$ ps, $\tau_{sf}^{hh} = 30$ ps and $\tau_{sf}^{e} = 30$ ps, $\tau_{sf}^{hh} = 1$ ps.

As mentioned earlier, the light hole spin-flip time has not much consequence on the absorption spectra and on the heavy hole exciton dynamics in particular, as we assume that both light hole spin-states scatter equally in both the heavy hole spin-states. Hence, we choose $\tau_{sf}^{lh} = \tau_{sf}^{hh}$.

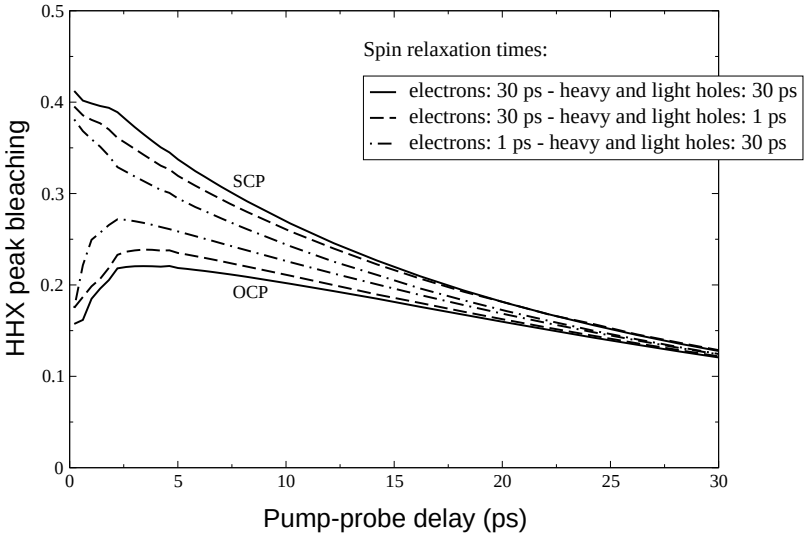

Figure 5.6: Heavy hole exciton peak bleaching dynamics. Comparison between various spin-flip time regimes.

To picture the influence of the spin-flip times on the heavy hole bleaching dynamics, we plot both the bleaching and the differential bleaching dynamics in Figs. 5.6 and 5.7. The differential bleaching is computed as (SCP - OCP)/2(SCP + OCP).

Here, we compare between the OCP and SCP only as the spin-flip time has no effect on the SLP spectra. The bleaching dynamics, in Fig. 5.6, shows that when the electron spin-flip time is short, the OCP and SCP curves converge faster than when it is long, even if the heavy hole spin-flip is short. The interesting feature that one can see on Fig. 5.7 is the convergence of the two curves that have a long electron spin-flip time, in about 30 ps. The differential absorption being finite, this means that after 30 ps, we cannot distinguish between the slow and fast heavy hole spin-flip time regimes. For a short electron spin-flip time, OCP and SCP bleaching curves converge much faster, hence the differential bleaching tends to 0 in 30 ps.

This means that the electrons, being lighter than the heavy holes[2], always dominate the phase space filling, even if the initial electron gas temperature is much higher than the heavy hole gas one (see Fig. 4.5 in chapter 4).

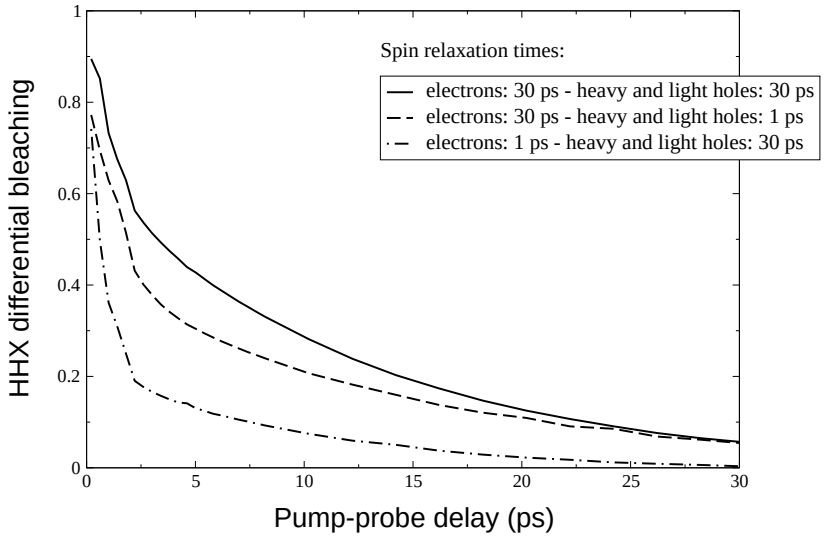

Figure 5.7: Heavy hole exciton peak differential bleaching dynamics. Comparison between various spin-flip time regimes.

Slow cooling regime

Calculations made with longer characteristic times for the plasma cooling ($\geq$ 5 ps), shown in Fig. 5.8, lead to results that are qualitatively very different from experimental data shown in Fig. 5.1.

The time evolution of the heavy hole exciton bleaching is characterized by a simple decay in the OCP and SCP cases (see Fig. 5.1), whereas our calculations show the presence of a maximum for short pump-probe delay due to increased Pauli blocking and screening because of plasma cooling. If the cooling characteristic time is increased, the numerical results show a plateau-like behaviour for pump-probe delays up to several picoseconds, before the recombination becomes dominant, as shown on Fig. 5.8. The early ($\leq$ 5 ps) behaviour observed in Fig. 5.4 for the OCP is enhanced and the SCP bleaching dynamics is qualitatively the same as in Fig. 5.4,

[2]In this case, $m_{hh}/m_e = 4$ (see the Introduction).

even though it exhibits a slower decay.

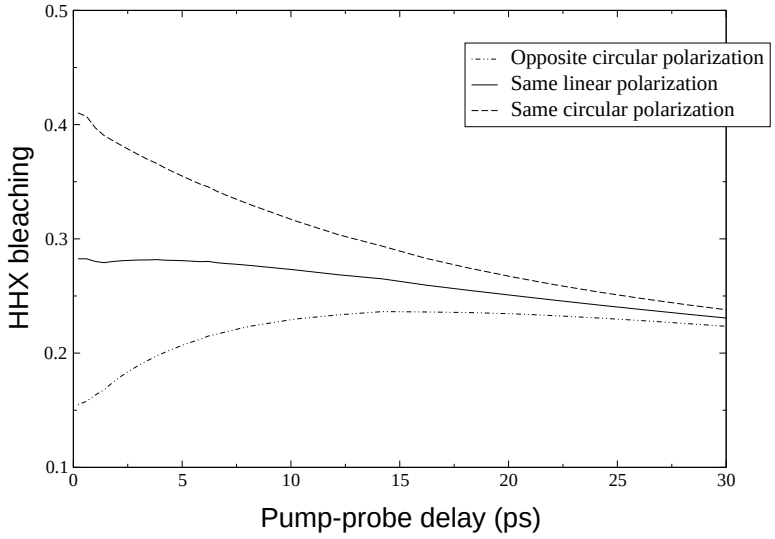

Figure 5.8: Heavy hole exciton peak bleaching dynamics computed with $\tau_{cool} = 5$ ps.

Slow light hole scattering regime

As mentioned at the beginning of this chapter, we do not have experimental data describing the light hole exciton dynamics. Hence, we cannot obtain enough information to extract the light hole scattering time τ_{lh}. We supposed it to be very fast, i.e. $\tau_{lh} = 0.5$ ps. In this section, we study the effect of a longer scattering time, $\tau_{lh} = 30$ ps (comparable to the nonradiative recombination time), on the heavy hole bleaching dynamics.

Except for τ_{lh}, all the scattering times involved in the calculation of the above heavy hole bleaching dynamics are the same as those used to produce the results shown in Fig. 5.4. Setting τ_{lh} longer modifies the Pauli blocking as well as the plasma screening in the three polarization configurations: OCP, SLP and SCP. The phase space filling effect is less important at the heavy hole exciton resonance as the heavy hole population does not increase as fast as in the previous case. Moreover, the plasma screening is also weaker than it was previously, as the total density of heavy holes, contributing more to it because of their heavy effective mass, is smaller.

Hence, the bleaching of the heavy hole exciton resonance is smaller with increas-

ing the light hole scattering time, τ_{lh}. Comparing Figs. 5.4 and 5.9, one can also note that modifying τ_{lh} has a more important impact on the OCP bleaching dynamics than it has on the SCP one. This is due to the fact that both the plasma screening and phase space filling dictate the amount of bleaching: in the OCP case, the initial bleaching is only due to plasma screening, whereas Pauli blocking has also to be taken into account for the SCP. As seen in the previous subsection, the electrons contribute more to the phase space filling than the heavy holes. As the pace of the light hole scattering does not affect much the electron gas (only through the very slow radiative recombination process), the change of τ_{lh} plays a more important role in the OCP bleaching dynamics because of plasma screening.

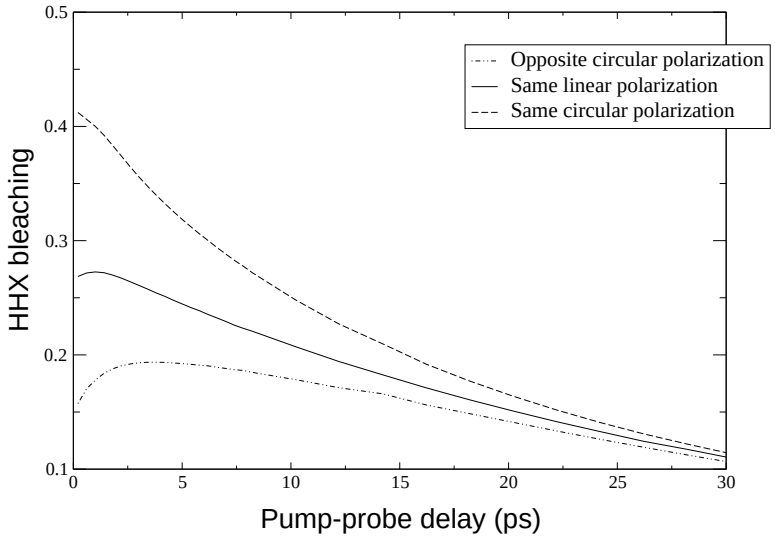

Figure 5.9: Calculated absorption spectra dynamics. Comparison between the OCP, SLP and the SCP heavy hole exciton peaks bleaching.

5.4 Discussion and conclusions

In our model, we considered spin-selective excitations and included various dynamical process. Except for the energy shift of the OCP heavy hole exciton, the numerical results are in good qualitative agreement with the experiment. According to our calculations, the spin populations equilibrate on a much longer time scale (30 ps) than the thermalization of the electron/hole plasma (1 ps). The plasma cooling enhances

the plasma screening and together with the relaxation of the distributions also enhances the Pauli blocking effect. These processes are amongst the fastest and we can observe their influence on the early behaviour of the exciton peaks bleaching and energy shift. The spin-flip process leads to opposite qualitative behaviours of the bleaching dynamics, depending on the initial polarization configurations. As seen above the exciton peaks bleaching and shift can either increase or decrease because of the spin-flip process depending on the type of exciton (heavy or light) and the polarizations OCP or SCP. The radiative recombination occurs on a time scale that is too large (about 1.6 ns in $ZnSe$) to have any effect on the fast bleaching and energy shift dynamics (below 100 ps). However, the nonradiative recombination is fast enough to observe an overall decay on a time scale shorter than 100 ps. As far as the energy shift is concerned, the screening model that we used for this work fails to describe at least qualitatively the OCP energy shift. The static plasmon-pole approximation leads to an overestimation of the bandgap shrinkage [42], which in turn leads to an important OCP heavy hole exciton peak redshift that is not observed on experimental data. As far as the SCP heavy hole exciton peak is concerned, the evaluated exciton binding energy for finite densities is too small because of the screening model we use. This explains, the initial large blueshift despite the important bandgap renormalisation in the SCP case. As for the SLP configuration, the static plasmon-pole approximation is good enough to describe the balance between the bandgap shrinkage and the exciton binding energy for finite plasma densities. With our model, it is possible to control the values of the phenomenological parameters in order to obtain further insight in the interplay between various dynamical processes. In this chapter, we explored various scenarios: different spin-flip times, slow plasma cooling and slow light hole scattering. Plasma screening and Pauli blocking depend on the complicated interplay between all the dynamical process. To go further, it would also be interesting to compare numerical results with more experimental data, especially for the light hole exciton dynamics.

Chapter 6

Exciton-electron scattering in semiconductor quantum-wells

6.1 Introduction

The understanding of many aspects of injection lasers requires a detailed knowledge of the gain spectrum versus photon energy, both for positive gain and optical absorption loss (negative gain). About twenty years ago, a method for measuring the absorption and gain spectra of lasers was presented by Henry *et al.* [40]. With this method, the absorption and gain spectra are determined from spontaneous emission spectra together with the measurement of the laser energy and differential quantum efficiency. The deduction of the gain spectrum is based on general relations between the rates of spontaneous emission, stimulated emission and optical absorption. These relations are independent of the type of optical transition or the nature of the initial and final state and absorption and gain spectra are obtained from spontaneous emission spectra. A derivation based on statistical mechanics shows the simplicity and generality of these relations. More recently (1990), Blood *et al.* [41] published a paper in which they used a method based on the analysis developed by Henry *et al.* to analyze the spontaneous emission spectra. With this method they could construct experimental curves of peak gain versus spontaneous recombination current from spontaneous emission spectra, without having to take into account optical losses or internal efficiency. Henry asserts that the model published in Ref. [40] is valid for any semiconductor in which the conduction band and the valence band are separately in thermal equilibrium and are characterized by quasi-Fermi levels, which can be the case for low and mid-gap semiconductors such as InP and $GaAs$ for instance, at room temperature. However, a new generation of lasers operating in

the blue spectral region has been arisen. These lasers are based on $ZnSe$ [77] and GaN [78]. Along with the large energy gap of these materials comes a large exciton binding energy of the same order as k_BT at room temperature. Therefore we can observe bound exciton states existing at high temperature which is mainly due to the strong Coulomb force in the wide-gap semiconductors. The importance of the excitonic gain processes is even further enhanced in quantum wells structures where the binding energy may be considerably larger than k_BT. It is then obviously not possible to assume two separate systems with no interaction between them. Hence, new theoretical treatment of the problem is needed to extend Henry's model the use of which would not be appropriate in the case of wide-gap semiconductors.

Models based either on bosonic exciton operators [79] or on Fermionic electron and hole operators [80, 81] have been proposed, but they are not fully satisfactory. Indeed, the "bosonic model" fails when one has to deal with high injection: the screening of the Coulomb potential weakens the binding and then produces an occupation of unbound scattering states which do not exhibit bosonic character. The "fermionic model" is too complex when high order excitonic correlations are important [70]. As we shall see below, another approach based on the concept of the degree of ionization of the electron-hole plasma [82, 83] deserves attention when ones needs to incorporate Coulomb correlations in the problem.

The aim of this chapter is to present a simple model to compute the spontaneous emission rate in wide-gap semiconductors quantum wells taking into account the exciton contribution. The object of section 2 is to present the interacting 2D electron-hole plasma model in the Boltzmann limit and the ionization degree. In section 3 the spontaneous emission rate in a free carrier plasma in quasi-equilibrium at room temperature is calculated. Section 4 is devoted to the problem of the exciton correlation. The ionization degree and the modified law of mass action are presented and studied in detail. We also evaluate the exciton-electron scattering matrix in a statically screened Coulomb potential after calculating the 2D exciton wavefunction. Finally, using Fermi's golden rule, we obtain an expression for the ex-

citon contribution to the spontaneous emission rate. Numerical results are presented and discussed in section 5, before concluding this chapter.

6.2 Spontaneous emission rate in semiconductor quantum-wells

6.2.1 The 2D electron/hole plasma

The model of the 2D electron-hole plasma in semiconductors [1] in which we deal with a mixture of two types of fermions (positively charged holes and negatively charged electrons) provides an interesting framework for the understanding of the thermodynamical and optical properties of semiconductor quantum wells. Here, we consider the case when the 2D carrier density, N, satisfies the following relation which defines the limit of the Boltzmann regime:

$$N\lambda_M^2/g \ll 1 \ , \tag{6.1}$$

where $\lambda_M = (2\pi\hbar^2/Mk_BT)^{1/2}$ is the thermal wavelength and g is the spin degeneracy of the 2D quasi-particles. The nondegenerate regime gives a realistic picture of the electron-hole plasma in wide-gap semiconductors in which we can neglect the effects of the Pauli blocking as long as we consider moderate carrier densities at room temperature.

As mentioned above, no fully satisfactory model concerning the optical properties of wide-gap semiconductors exists. Nevertheless, the concept of the degree of ionization in the interacting electron-hole plasma can help in obtaining some results which are useful for tackling this problem. Denoting a the type of the particle we consider (electrons or holes), we can divide the total density of particles a in the following way:

$$N_a = N_a^0 + N_a^{corr} \ , \tag{6.2}$$

according to Zimmerman's approach [84]. There are two contributions to the total density. The first, N_a^0, is the density of uncorrelated particles with renormalized

energies. This term is independent of the inter-particle interaction. The second one, N_a^{corr}, contains all correlation effects both in the bound and continuum states. The expression of the degree of ionization is then given by the following simple relation:

$$\alpha = \frac{N_e^0}{N_e} = \frac{N_e^0}{N_e^0 + N_e^{corr}} \ . \tag{6.3}$$

When α is close to unity, the thermodynamic properties of the electron-hole plasma are those of the ideal gas (defined by $\alpha = 1$). The dominant lasing mechanism is then stimulated emission from the free carrier plasma. For lower values of the degree of ionization we can observe a deviation of the thermodynamic properties of the plasma from those of the ideal gas which we cannot neglect. Then, several excitonic gain processes have to be considered. Therefore it is crucial to know the value of the degree of ionization to determine the main emission mechanism.

6.2.2 Screened Coulomb potential

The interaction between particles in an exciton/electron-hole plasma can be modeled by the statically screened Coulomb potential. The simplest approach is the use of the 2D statically screened potential [85]:

$$V_s(\rho) = \mp\frac{e^2}{\epsilon}\int_0^\infty \frac{qJ_0(q\rho)}{q+q_s}\ dq = \mp\frac{e^2}{\epsilon}\left[\frac{1}{\rho} - \frac{\pi}{2}\ \left(\mathbf{H}_0(q_s\rho) - N_0(q_s\rho)\right)\right] \ , \tag{6.4}$$

where q_s, in the Boltzmann limit, is the 2D Debye-Hückel screening wavenumber (which depends on temperature and carrier density), ϵ is the static dielectric constant of the semiconductor and $J_0(x)$, $N_0(x)$ and $\mathbf{H}_0(x)$ are the Bessel, Neumann and Struve functions respectively [86, 87]. We distinguish the electron-hole attraction and the electron-electron or hole-hole repulsion with the $\mp$ sign.

The validity of the potential Eq. (6.4) can be debated since it does not give a very realistic description of excitonic effects in a low density electron-hole plasma according to the authors of Refs. [88, 89]. Nevertheless, it is convenient for simpli-

fying the analytical calculations on one hand, and, on the other hand, despite the numerous realistic corrections and the existence of other approaches, it remains the most suitable to take into account the shallow bound states and low-energy scattering states [83] which are crucial for a proper description of the physics of the 2D electron-hole plasma as we shall see later.

6.2.3 The spontaneous emission rate

The spontaneous emission rate is a function of the separation of the quasi-Fermi levels [40, 71]. The first step in building our model consists of considering a free carrier plasma. The spontaneous emission rate is evaluated assuming a quantized electromagnetic field (defined in Appendix D). In the next step, the correlation effects contained in the correlated density, N_a^{corr}, will be taken into account. At room temperature there are several processes occurring in the exciton/electron-hole plasma, such as exciton-exciton scattering, phonon-exciton scattering, free carrier-exciton scattering. Here, only the scattering of $1s$ excitons with free electrons will be considered as it is the most likely process leading to photoluminescence (PL) at room temperature [90]. The knowledge of the 2D wavefunctions of these quasiparticles is then required to evaluate the scattering matrix and use Fermi's golden rule to calculate the contribution of the correlated quasi-particles to the total photoluminescence spectrum.

Here, we give the general expressions of both the free carrier plasma and exciton contributions to the spontaneous emission rate, $R_{sp}^{fc}(\hbar\Omega)$ [71] and $R_{sp}^{corr}(\hbar\Omega)$ [91, 92]:

$$\begin{aligned} R_{sp}^{fc}(\hbar\Omega) &= 2\sum_{\mathbf{k}\in BZ} r_{spon}(\mathbf{k}) \\ &= 2\sum_{\mathbf{k}\in BZ} \frac{1}{\tau_{rad}}\, f_c\left(E_c(\mathbf{k})\right)\left(1-f_v\left(E_v(\mathbf{k})\right)\right)\, \delta(\hbar\Omega - E_v - E_c)\ . \end{aligned} \tag{6.5}$$

The sum $\sum_{\mathbf{k}}$ is performed the over the first Brillouin zone, BZ. The radiative lifetime, τ_{rad} is calculated in Appendix D.

$$R_{sp}^{corr}(\hbar\Omega) = \sum_{\mathbf{K}} \sum_{\mathbf{k}_2} C_{\mathbf{K},\mathbf{k}_2} N_{\mathbf{K}} N_{\mathbf{k}_2} \ , \tag{6.6}$$

with

$$\begin{aligned} C_{\mathbf{K},\mathbf{k}_2} &= \frac{2\pi}{\hbar} \, |V_{scat}(K)|^2 \left(\frac{4\pi\beta_1 \Omega/\omega_0}{(1-\Omega^2/\omega_0^2)^2 + 4\pi\beta_1} \right) \\ &\quad \times \delta \left(E_g - E_b^{ex} + \frac{\hbar^2 K^2}{2M} - \hbar\Omega - \frac{\hbar^2}{2m_e}(K^2 + 2\mathbf{K}.\mathbf{k}_2) \right) \ , \end{aligned} \tag{6.7}$$

where $N_{\mathbf{K}}$ and $N_{\mathbf{k}_2}$ are the exciton and free carrier distributions (see Appendix E for detail of the calculations). The coefficient β_1 ensures that there is no divergence when the photon energy $\hbar\Omega$ is equal to the gap energy $E_g = \hbar\omega_0$. The exciton binding energy is E_b^{ex}, so the total energy of an exciton is: $E_X = E_g - E_b^{ex} + \hbar^2 K^2/2M$.

6.3 Contribution of the free-carrier plasma to the spontaneous emission rate

We show here the main steps to calculate the spontaneous emission rate R_{sp}^{fc} due to a distribution of carriers in quasi-thermodynamical equilibrium in a semiconductor quantum well. To do so, we need the knowledge of the radiative lifetime τ_{rad} evaluated in Appendix D.

The wavevectors $\mathbf{k}$, in Eq. (6.5), must satisfy the condition imposed by the conservation of energy expressed through the delta function:

$$E_c(\mathbf{k}) - E_v(\mathbf{k}) = \hbar\Omega = \frac{\hbar^2 \mathbf{k}^2}{2m_r} + E_g \ . \tag{6.8}$$

Approximating the discrete sum by an integral, we find the spectral distribution of the radiative recombination rate in a semiconductor:

$$R_{sp}^{fc}(\hbar\Omega) = \frac{m}{\pi\hbar^2} \int_0^\infty r_{spon}(E) \ \delta(E - \hbar\Omega) \ dE = \frac{m}{\pi\hbar^2} \ r_{spon}(\hbar\Omega)$$

$$= \frac{m}{\pi\hbar^2\tau_R}\, f_c(E_c)\,(1 - f_v(E_v)) \ . \tag{6.9}$$

Considering the expression of τ_{rad} given in Appendix D, Eq. (D.13), one finds:

$$R_{sp}^{fc}(\hbar\Omega) = \frac{q^2 x_{vc}^2 n_{op}\Omega^3}{\pi c^3 \hbar\epsilon_0}\ \frac{m}{\pi\hbar^2}\ f_c(E_c)\,(1 - f_v(E_v)) \ . \tag{6.10}$$

At room temperature, the distributions $f_c(E_c)$ and $f_v(E_v)$ in Eq. (6.10) can be approximated by Boltzmann functions:

$$\begin{cases} f_c(E_c) \approx \exp\left(-\dfrac{E_c - E_{F_c}}{k_B T}\right) \\ 1 - f_v(E_v) \approx \exp\left(-\dfrac{E_{F_v} - E_v}{k_B T}\right) \end{cases} \tag{6.11}$$

Thus, we can write:

$$f_c(E_c)\,(1 - f_v(E_v)) \approx \exp\left(-\frac{\hbar\Omega}{k_B T} \ + \ \frac{\Delta E_F}{k_B T}\right) \ , \tag{6.12}$$

where ΔE_F is the difference between the two quasi-Fermi levels: $\Delta E_F = E_{F_c} - E_{F_v}$. The spectral distribution can then be written as follows:

$$R_{sp}^{fc}(\hbar\Omega) = \frac{m_r}{\pi\hbar^2\tau_{rad}} e^{-\beta(E_c - E_{F_c})} e^{-\beta(E_{F_v} - E_v)} \ . \tag{6.13}$$

Considering the following relations between the chemical potentials, μ_e, μ_h, the gap, E_g, and the quasi-Fermi levels of the two bands, E_{F_c} and E_{F_v}, and between the photon energy and the energies of the two bands, E_c and E_v:

$$\begin{cases} E_{F_c} = E_g + \mu_e \\ E_{F_v} = -\mu_h \\ E_c - E_v = \hbar\Omega \end{cases} \tag{6.14}$$

Eq. (6.9) can be rewritten as follows:

$$R_{sp}^{fc}(\hbar\Omega) = \frac{m_r}{\pi\hbar^2\tau_{rad}}\ e^{-\beta(\hbar\Omega - E_g)}\ e^{\beta(\mu_e + \mu_h)} \ . \tag{6.15}$$

This expression explicitly depends on the fugacities $z_a = e^{\beta\mu_a}$, which can be

calculated from the low density limit expansion of the density of the noninteracting Fermi gas, as we shall see later (see Eqs. (6.22) and (6.61)).

6.4 The exciton contribution to the spontaneous emission rate

The term N_a^{corr} defined in Eq. (6.2), which depends on the inter-particle interaction, contains all correlation effects both in the bound and in the continuum states. For significant values of N_a^{corr} (low degree of ionization), several excitonic gain processes have to be considered for the lasing mechanism [93, 94, 95]. Therefore we need an accurate study of the bound and scattering states to gain further insight into the phenomena involved in the optical properties of wide-gap semiconductor quantum wells. Here, the attention is focused on the scattering between a $1s$ exciton and a free electron. Indeed, at room temperature, the population of $1s$ excitons remains the most important and their scattering with free electrons is the most likely process contributing to the photoluminescence [90]. This can be quickly described as follows: the exciton leaves its initial state on the band structure and reaches the photon line, transferring its momentum to the free electron as depicted in Fig. 6.1.

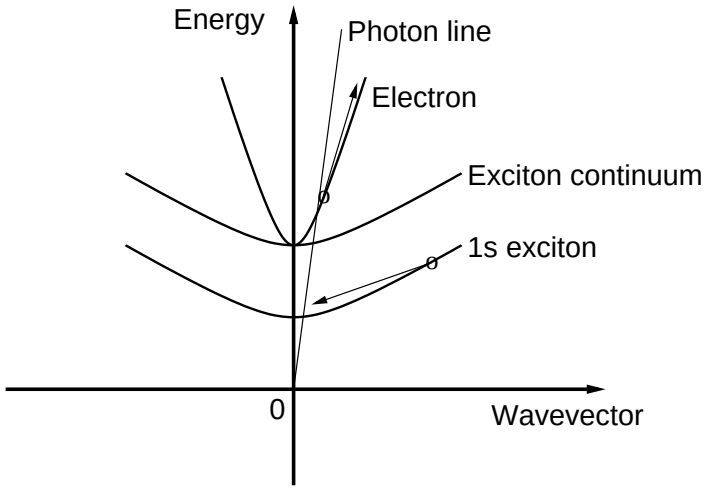

Figure 6.1: $1s$ exciton-electron scattering leading the exciton to the photon line whereas the electron gains momentum.

In order to calculate the scattering matrix element, the knowledge of the exciton wavefunctions is required. The statically screened Coulomb potential chosen to treat

the problem is given by Eq. (6.4). It increases for small values of ρ and vanishes at large distances as $1/\rho^3$ ($\rho \to \infty$). Such behavior permits the application of the variable phase method to this potential.

6.4.1 The ionization degree and modified law of mass action

To be able to calculate the ionization degree of the plasma, the knowledge of the partition function describing all the interactions between the particles is required. Therefore, we have to take into account the scattering state contributions in addition to the bound state sum. Indeed, if the scattering term is neglected the bound state energies increase towards the continuum with increasing screening. As such a state reaches zero energy, a partition function that contains only the bound state sum will be discontinuous. The variable phase method [96] allows on the one hand to calculate these shallow-state binding energies and low-energy scattering phase shifts, and, on the other hand, is a way to compute the number of bound states in the attractive potential Eq. (6.4) thanks to the 2D Levinson's theorem [97]:

$$\lim_{k\to 0} \delta_m(k) = \nu_m \pi \ , \tag{6.16}$$

where m is the value of the projection of the angular momentum onto the symmetry axis of the potential and ν_m the number of bound states. It is possible to show that using the 2D Levinson's theorem Eq. (6.16), a proper account of scattering eliminates the singularities in the partition function and thus in the thermodynamic properties of the nonideal gas [97].

The relation between the 2D scattering phase shift and the two-body interaction part of the partition function of 2D interacting Boltzmann particles is given by the 2D analogue of the Beth-Uhlenbeck formula [98]:

$$Z_{int} = \sum_m \sum_\nu e^{-\beta E_{m,\nu}} + \frac{1}{\pi} \int_0^\infty \left(\sum_{m=-\infty}^{\infty} \frac{d\delta_m(q)}{dq} \right) \ e^{-q^2/q_T^2} dq \ . \tag{6.17}$$

m is the projection of the angular momentum onto the axis normal to the plane of 2D motion (m is an integer), $\delta_m(q)$ is the 2D scattering phase shift dependent on the relative-motion momentum q [98, 85], $q_T^2 = 2\mu k_B T/\hbar^2$, μ being the reduced mass, and the double sum ranges only over bound states which energies are given by $E_{m,\nu}$ (the index ν enumerates bound states with given m).

Integrating by parts the scattering term in Eq. (6.17) and using the expression Eq.(6.16) of the 2D Levinson's theorem leads to the following expression of the two-body interaction part of the 2D interacting Boltzmann particles:

$$Z_{int} = \sum_m \sum_\nu \left(e^{-\beta E_{m,\nu}} - 1 \right) + \frac{2}{\pi q_T^2} \int_0^\infty \left(\sum_{m=-\infty}^{\infty} \delta_m(q) \right) \, e^{-q^2/q_T^2} dq \ . \qquad (6.18)$$

The zero-energy part of the phase shift integral exactly cancels the zero-energy part of the bound-state sum, removing the discontinuities in the partition function. Thus, the thermodynamic properties of the system do not exhibit singularities anymore [97].

Another aspect of the problem is that electrons and holes are Fermions. For a Fermion system, the symmetric spin states have to be multiplied by antisymmetric spatial states, for which we have odd values for m, and the antisymmetric spin states have to be multiplied by symmetric spatial states for which we have even values for m. So, to calculate the partition functions we have to consider the Pauli exclusion principle for identical particles. A direct consequence will be the change of the expression in the sum over m. In the case of repulsive fermions (spin 1/2 for electrons and holes) which do not form bound states, the electron-electron and hole-hole parts of the partition functions Z_{ee} and Z_{hh} contain the scattering term only. The "a-a" (a = electron or hole) part of the partition function is then deduced from Eq. (6.18) [83]:

$$Z_{aa} = \frac{1}{2\pi} \sum_{m=-\infty}^{\infty} \left(2 - (-1)^m \right) \int_0^\infty \frac{d\delta_m(q)}{dq} \, e^{-\beta\hbar^2 q^2/m_a} dq \ , \qquad (6.19)$$

where m_a is the effective mass of the particle a. Here we assume that both electron states in quantum wells are two-fold degenerate (the spin degeneracy being given by $2s+1$). The only difference between Z_{hh} and Z_{ee} comes from the difference between electron and hole effective masses.

The partition functions being calculated, we can derive the expression of the degree of ionization. In the low-density limit the total density of particles of type a is given by [83]:

$$N_a \approx \frac{g_a}{\lambda_{m_a}^2}\ z_a \pm \frac{1}{2}\frac{g_a}{\lambda_{m_a}^2}\ z_a^2 + \lambda_{\mu_{aa}}^2 \left(\frac{g_a}{\lambda_{m_a}^2}\right)^2 Z_{aa} z_a^2 + \lambda_{\mu_{ab}}^2 \frac{g_a}{\lambda_{m_a}^2}\frac{g_b}{\lambda_{m_b}^2}\ Z_{ab} z_a z_b \tag{6.20}$$

where z_a and z_b are the fugacities, $z = e^{\beta\mu}$, of the particles of types a and b respectively with effective masses m_a and m_b, and spin degeneracy g_a and g_b. The reduced masses are noted μ_{aa} and μ_{ab}. As mentioned in Eq. (6.2), the total density n_a is split into two contributions:

$\Rightarrow$ **the uncorrelated density** N_a^0

$$N_a^0 = \frac{g_a}{\lambda_{m_a}^2}\ z_a - \frac{1}{2}\frac{g_a}{\lambda_{m_a}^2}\ z_a^2\ , \tag{6.21}$$

which corresponds to the low-density expansion of the density of the noninteracting Fermi gas:

$$N_a^0 = \frac{g_a}{\lambda_{m_a}^2}\ \ln\ (1 + z_a)\ . \tag{6.22}$$

$\Rightarrow$ **the interaction-dependent correlated density** N_a^{corr}

$$N_a^{corr} \approx \sum_b N_a^0 N_b^0 \lambda_{\mu_{ab}}^2 Z_{ab}\ . \tag{6.23}$$

Eq. (6.23) constitutes the modified law of mass action in 2D [82] and allows a

proper description of the screening of excitons by the 2D electron-hole plasma and strong scattering of particles within the plasma which both play a crucial role in the properties of wide-gap semiconductors.

For a two-component electron-hole plasma the 2D screening wavenumber appearing in Eq. (6.4) is given in the Boltzmann limit by [99]:

$$q_s a_B = \frac{2\pi\hbar^2}{\mu_{eh} k_B T}\left(N_h^0 + N_e^0\right) = 4\pi \frac{R_y}{k_B T}\left(N_e^0 a_B^2 + N_h^0 a_B^2\right) \ , \tag{6.24}$$

where a_B is the exciton Bohr radius and R_y is the excitonic Rydberg. In Eq. (6.24), it is assumed that the screening by the correlated carriers (excitons) is much smaller then the free carrier screening when correlated and uncorrelated densities are of the same order. The use of the model semiconductor allows to go further in the calculations: having $N_h^0 = N_e^0 = \alpha N$, we can rewrite Eq. (6.24) as follows:

$$q_s a^* = 8\pi\alpha \frac{R_y^*}{k_B T}\ N a^{*2} \ . \tag{6.25}$$

The role of the degree of ionization α appears now more clearly: there is a direct link between the behaviour of α and the values of the screening wavenumber q_s which determines the strength of the interaction between charged particles in the plasma. For the model semiconductor the modified law of mass action, Eq. (6.23), can be rewritten as

$$N_e^{corr} a^{*2} = 4\pi \left(N_e^0 a^{*2}\right)^2 \frac{R_y^*}{k_B T}\ \left(Z_{eh} + Z_{ee}\right) \ , \tag{6.26}$$

and the degree of ionization has the explicit form [83]:

$$\alpha = \left[1 + \frac{q_s a^*}{2}\left(Z_{eh} + Z_{ee}\right)\right]^{-1} \ , \tag{6.27}$$

considering Eqs. (6.25) and (6.26). The ionization degree, α, is shown in Fig. 6.2 as a function of the 2D plasma density, for $ZnSe$ and $GaAs$. The degree of ionization of the electron-hole plasma in a $ZnSe$ quantum well is significantly lower than in

a $GaAs$ quantum well with the same carrier density and temperature. This is due to the strong Coulomb forces in $ZnSe$ quantum wells that are the source of correlations even at room temperature. Moreover, the qualitative behaviour is different as α exhibits a minimum for $ZnSe$ at low density, whereas it is a monotonically decreasing function of the 2D plasma density for $GaAs$. This has the following explanation: at low density, the correlated density is proportional to the square of the total plasma density (see Eq. 6.26), as at low density and high temperature, the electron/hole plasma behaves as an ideal gas with α close to 1 (see Eq. 6.3). Hence the degree of ionization decreases with increasing plasma density. However, with a further increase in the total density, plasma screening becomes important and the inter-particle correlations caused by the Coulomb interaction start to decrease. Correspondingly, the degree of ionization changes the character of its density dependence. In $GaAs$, the Coulomb forces are small compared to $ZnSe$ even at low density, so their influence on the density-dependence of α is not as important as it is in $ZnSe$. Further detail and discussion can be found in Ref. [83].

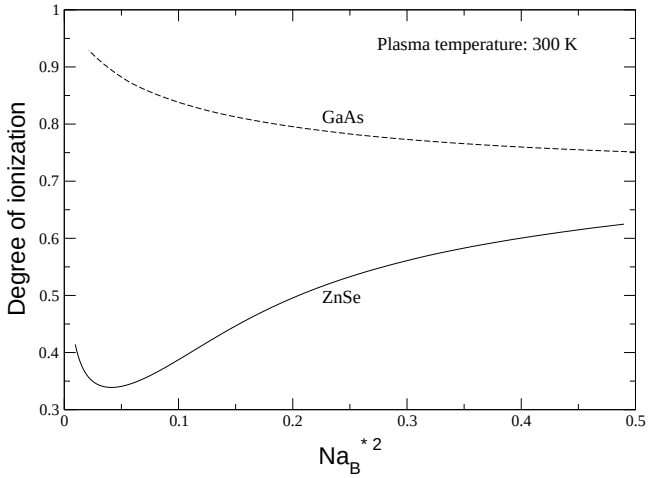

Figure 6.2: Ionization degree evaluated for $GaAs$ and $ZnSe$ in the Boltzmann regime for $T = 300K$, as a function of the 2D plasma density (from M. E. Portnoi and I. Galbraith's calculations in Ref. [83]).

One of the main results of the application of the variable phase method to scattering and bound states in a 2D screened Coulomb potential is that it leads to a strong deviation [83] from the standard law of mass action whose weakness is that

we cannot use it to treat the screening of excitons by the electron-hole plasma and the strong scattering of particles within the plasma which both play a crucial role in its properties.

6.4.2 The 2D exciton wave function

To calculate the matrix elements in Eq. (6.7), we must obtain an explicit expression of the 2D exciton wave function. Work based on a varational calculation has already been done in Ref. [99], but for our purposes, we make use of the results of the scattering theory with the variable phase method, neglecting the intrinsic spin effects. As we suppose that the interaction between the two particles just depends on the relative distance, we can split the problem into two parts: the study of the relative motion of the two particles and the study of the motion of the center of mass which does not depend on the interaction. Then the total Hamiltonian can be written in the following way: $\hat{H}_{tot} = \hat{H}_{cm} + \hat{H}_{rel}$.

First, let us study the relative in-plane motion of an electron interacting with a hole via the symmetric 2D screened Coulomb potential $V_s(\rho)$, where ρ is the relative distance between both particles. The energy of the relative motion is E. It is possible to picture this situation as the motion of a particle with energy E and which mass is given by the reduced mass of the electron and hole, μ_{eh}, in an external central potential $V_s(\rho)$. This motion is described by the wave function satisfying the stationary Schrödinger equation. Since we deal with a central potential, the angular momentum $\mathbf{L}$ is a constant of the motion. It is then possible to find stationary states with a defined momentum. As we are working in a 2D situation, these states are eigenstates common to the Hamiltonian $\hat{H}_{rel}$, and the angular momentum $\mathbf{L}$ which can be identified to its only component L_z perpendicular to the plane of the motion. The wave functions associated to these eigenstates are the partial waves.

We can use the radial symmetry to separate the variables in the expression for the wavefunction: $\psi_m(\rho, \varphi) = R_m(\rho)e^{im\varphi}$ where $R_m(\rho)$ is the radial wave function and m the value of the projection of the angular momentum onto the symmetry axis

of the potential. The angular dependence is contained in $e^{im\varphi}$ which is an eigenstate of L_z, and the radial dependence in $R_m(\rho)$ on which $V_s(\rho)$ acts. We just need then a couple of numbers: the principal quantum number, n, and the projection of the angular momentum onto the symmetry axis of the potential, m, to characterize these eigenstates. We readily obtain the following radial Schrödinger equation:

$$\frac{d^2}{d\rho^2}\ R_m(\rho) + \frac{1}{\rho}\frac{d}{d\rho}\ R_m(\rho) + \left(\kappa^2 - U(\rho) - \frac{m^2}{\rho^2}\right)\ R_m(\rho) = 0\ , \tag{6.28}$$

for a given value of m and where $k^2 = 2\mu_{eh}E/\hbar^2$ and $U(\rho) = 2\mu_{eh}V_s(\rho)/\hbar^2$.

Considering Eq. (6.28), we can see that $R_{-m}(\rho) = R_m(\rho)$; so, we just need to take into account the positive values of m ($m \geq 0$).

For the bound states, the energy E is negative. We introduce then the imaginary wavenumber $k = i\kappa$. As we chose a potential vanishing at large distances, the solution of the radial equation Eq. (6.28) can be approximated for large ρ by the solution of the free Bessel equation, a linear combination of the modified Bessel functions of the first and second kind. Then, the solution of the radial Schrödinger, Eq. (6.28), can be written as follows [83]:

$$R_m(\rho) = A_m\ \left(I_m(\kappa\rho)\cos\eta_m + \frac{2}{\pi}\ K_m(\kappa\rho)\sin\eta_m\right)\ , \tag{6.29}$$

where A_m and η_m are the amplitude and the scattering phase shift; $I_m(\kappa\rho)$ and $K_m(\kappa\rho)$ are the modified Bessel functions of the first and second kinds respectively. $I_m(\kappa\rho)$ and $K_m(\kappa\rho)$ are two linearly independent solutions of the free Bessel equation for the negative value of k^2 and are respectively the diverging and the converging contributions of the free radial wave function whose weights are characterized by $\cot\eta_m$.

Let us picture our problem speaking in terms of incoming and outgoing waves. If we compare both of the situations for which we consider and do not consider respectively the central potential, we can say that even if the incoming wave is obviously the same, the outgoing wave of the stationary scattering state differs from

that of the plane wave by the presence of a phase factor $e^{2i\eta_m}$. In other words, the effect of the scattering potential is to shift the phase of each outgoing partial wave.

To solve the problem for all ρ, not just $\rho \longrightarrow \infty$, the scattering phase shift η_m and the amplitude A_m are both considered not as constants but as explicit functions of ρ and κ in the variable phase method. With Eqs. (6.28) and (6.29) it is possible to find a condition on $\eta_m(\rho,\kappa)$ so as to have $R_m(\rho)$ satisfying Eq. (6.28) within the framework of the variable phase method. This condition will also help us in finding an equation from which we shall be able to obtain the amplitude $A_m(\rho,\kappa)$.

The scattering phase shift satisfies the following first order, non-linear differential equation of the Ricatti type [83]:

$$\frac{d}{d\rho}\,\eta_m(\rho,\kappa) = -\frac{\pi}{2}\,\rho\,U(\rho)\times\left(I_m(\kappa\rho)\cos\eta_m(\rho,\kappa)+\frac{2}{\pi}\,K_m(\kappa\rho)\sin\eta_m(\rho,\kappa)\right)^2\,, \tag{6.30}$$

provided that we consider the following definition for the first derivative of $R_m(\rho)$ which is just a condition we are free to choose to treat our problem:

$$\frac{d}{d\rho}\,R_m(\rho) = A_m(\rho,\kappa)\left(\frac{d}{d\rho}\,I_m(\kappa\rho)\cos\eta_m(\rho,\kappa)+\frac{2}{\pi}\,\frac{d}{d\rho}\,K_m(\kappa\rho)\sin\eta_m(\rho,\kappa)\right)\,, \tag{6.31}$$

and we use the Wronskian of the modified Bessel functions:

$$W\{I_m(x),K_m(x)\} = I_m(x)\,\frac{d}{dx}\,K_m(x) - K_m(x)\,\frac{d}{dx}\,I_m(x) = -\frac{1}{x}\,. \tag{6.32}$$

Eq. (6.30) is called the phase equation and must be solved with the following boundary condition:

$$\eta_m(0,\kappa) = 0\,, \tag{6.33}$$

thus ensuring that the radial function does not diverge at $\rho = 0$. The phase equation

is a self-consistent calculated constraint on $\eta_m(\rho,\kappa)$ which allows to use Eq. (6.29) as a solution of the radial Schrödinger Eq. (6.28).

The following differential equation defines the amplitude $A_m(\rho,\kappa)$:

$$\frac{d}{d\rho}A_m(\rho,\kappa) = -\frac{\pi}{2}\,\rho U(\rho)A_m(\rho,\kappa)$$

$$\times\left(\left(I_m^2(\kappa\rho) - \frac{4}{\pi^2}\,K_m^2(\kappa\rho)\right)\frac{\sin 2\eta_m(\rho,\kappa)}{2} + \frac{2}{\pi}\,I_m(\kappa\rho)K_m(\kappa\rho)\left(1-2\cos^2\eta_m(\rho,\kappa)\right)\right)\,. \tag{6.34}$$

Eq. (6.34) is obtained from the radial Schrödinger equation, Eq. (6.28), whose solution is given in Eq. (6.29). Differentiating Eq. (6.31) and comparing the resulting expression with Eq. (6.29) we obtain:

$$\left(I_m(\kappa\rho)\cos\eta_m(\rho,\kappa) + \frac{2}{\pi}\,K_m(\kappa\rho)\sin\eta_m(\rho,\kappa)\right)\,\frac{d}{d\rho}\,A_m(\rho,\kappa)$$

$$= A_m(\rho,\kappa)\left(I_m(\kappa\rho)\sin\eta_m(\rho,\kappa) - \frac{2}{\pi}\,K_m(\kappa\rho)\cos\eta_m(\rho,\kappa)\right)\,\frac{d}{d\rho}\,\eta_m(\rho,\kappa)\,. \tag{6.35}$$

To solve Eq. (6.35), one needs to first calculate the scattering phase shift by solving Eq. (6.30) and this is done numerically.

Hence, the final expression of the relative wave function $\psi_m(\rho,\varphi)$ is:

$$\psi_m(\rho,\varphi) = A_m(\rho,\kappa)\left(I_m(\kappa\rho)\cos\eta_m(\rho,\kappa) + \frac{2}{\pi}\,K_m(\kappa\rho)\sin\eta_m(\rho,\kappa)\right)e^{im\varphi}\,. \tag{6.36}$$

where $\eta_m(\rho,\kappa)$ is defined by the phase equation, Eq. (6.35), and the boundary condition given by Eq. (6.33), and the amplitude $A_m(\rho,\kappa)$ by Eq. (6.34).

For the bound states the diverging solution vanishes, thus implying the asymptotic condition:

$$\lim_{\rho\to\infty}\eta(\rho,\kappa) = (\nu - 1/2)\pi\,, \tag{6.37}$$

where ν enumerates the bound states for a given m. The number of non-zero nodes

of the radial wave function is given by $\nu - 1$.

The total exciton wave function is simply given by the product of the wave function of the center of mass of the two particles {electron;hole} by the relative wave function calculated above. The motion of the center of mass is only characterized by the kinetic energy E_{cm} which can be identified to the Hamiltonian $\hat{H}_{cm}$. Then the plane wave $\phi_{\mathbf{k}_{cm}}(\mathbf{R})$ has to satisfy the stationary Schrödinger equation:

$$\hat{H}_{cm}\phi_{\mathbf{k}_{cm}}(\mathbf{R}) = -\frac{\hbar^2}{2M}\ \overrightarrow{\nabla}_R^2\ \phi_{\mathbf{k}_{cm}}(\mathbf{R}) = E_{cm}\phi_{\mathbf{k}_{cm}}(\mathbf{R})\ , \tag{6.38}$$

where $\mathbf{R}$ is defined by $\mathbf{R} = (m_e\mathbf{r}_e + m_h\mathbf{r}_h)/(m_e + m_h)$ and $M = m_e + m_h$.

The solution of Eq. (6.38) is simply a plane wave:

$$\phi_{\mathbf{k}_{cm}}(\mathbf{R}) = \frac{1}{\sqrt{\mathcal{A}}}\ \exp(-i\mathbf{k}_{cm}\cdot\mathbf{R})\ , \tag{6.39}$$

where $\mathcal{A}$ is the area of the 2D system and $k_{cm} = \sqrt{2ME_{cm}}/\hbar$.

Considering Eqs. (6.29) and (6.39) the exciton wave function reads:

$$\Psi^{ex}_{m,\kappa,\mathbf{k}_{cm}}(\mathbf{R},\rho,\varphi) = \phi_{\mathbf{k}_{cm}}(\mathbf{R}) \times \psi_m(\rho,\varphi) =$$

$$\frac{1}{\sqrt{\mathcal{A}}}\ \exp(-i\mathbf{k}_{cm}\cdot\mathbf{R}) \times A_m(\rho,\kappa)\left(I_m(\kappa\rho)\cos\eta_m(\rho,\kappa) + \frac{2}{\pi}\ K_m(\kappa\rho)\sin\eta_m(\rho,\kappa)\right)e^{im\varphi}\ . \tag{6.40}$$

6.4.3 The scattering matrix elements

Knowing the explicit expression of the exciton (bound state) wave function given by Eq. (6.40), it is possible to evaluate the influence of the correlated part of the total plasma density on the spontaneous emission. We only consider the scattering of an electron of the continuum with a $1s$ exciton which will transfer its momentum to reach the photon line. Both Coulomb attraction and repulsion between the free electron in the continuum and the hole and the electron of the exciton have to be taken into account. They respectively interact via the screened potentials defined in Eq. (6.4) which can be explicitly written as follows in the Fourier space [96]:

$$\widetilde{V}_s^{\mp}(q) = \mp \frac{e^2}{2\epsilon \mathcal{A}} \frac{1}{q+q_s} \ , \tag{6.41}$$

where the upper sign is for the electron-hole attraction and the lower sign is for the electron-electron or hole-hole repulsion.

In the Boltzmann limit, the screening wavenumber q_s for a 2D electron gas is:

$$q_s = \frac{e^2 N_e^0}{2\epsilon_0 k_B T} \ . \tag{6.42}$$

This result is known as the 2D Debye-Hückel screening wavenumber.

In this work we are concerned with the scattering of a $1s$ exciton with a free electron. The population of $1s$ excitons being the most important at room temperature, it is very likely that they can scatter with a free carrier in the plasma. The exciton has to transfer its momentum to the free electron to reach the photon line to be able to ionize and emit photons.

The general form of the scattering matrix element V_{scat} can be written as follows:

$$\begin{aligned} V_{scat} \ = \ & \iiint \phi^{\dagger e_2,f}_{\mathbf{k}_{e_2}+\mathbf{k}_{cm}}(\mathbf{r}_{e_2}) \Psi^{\dagger ex,f}_{0,\kappa,\vec{0}}(\rho) \ V_s(\rho_-) \ \Psi^{ex,i}_{0,\kappa,\mathbf{k}_{cm}}(\mathbf{R},\rho) \phi^{e_2,i}_{\mathbf{k}_{e_2}}(\mathbf{r}_{e_2}) d\mathbf{r}_{e_1} d\mathbf{r}_{e_2} d\mathbf{r}_h \\ & + \iiint \phi^{\dagger e_2,f}_{\mathbf{k}_{e_2}+\mathbf{k}_{cm}}(\mathbf{r}_{e_2}) \Psi^{\dagger ex,f}_{0,\kappa,\vec{0}}(\rho) \ V_s(\rho_+) \ \Psi^{ex,i}_{0,\kappa,\mathbf{k}_{cm}}(\mathbf{R},\rho) \phi^{e_2,i}_{\mathbf{k}_{e_2}}(\mathbf{r}_{e_2}) d\mathbf{r}_{e_1} d\mathbf{r}_{e_2} d\mathbf{r}_h \ , \end{aligned} \tag{6.43}$$

where $\mathbf{R}$ and ρ are defined as above and ρ_+ and ρ_- are respectively the distances between the free electron and the one forming the exciton, and between the hole and the electron in the exciton: $\rho_- = \| \mathbf{r}_h - \mathbf{r}_{e_2} \|$ and $\rho_+ = \| \mathbf{r}_{e_2} - \mathbf{r}_{e_1} \|$. The signs $-$ and $+$ characterize the nature of the potentials V_s between the particles: attractive and repulsive respectively. The upper indices i and f indicate the initial and final states of the particles.

It is possible to rearrange the above equation so as to obtain a simpler expression of V_{scat}. This is shown now with the calculation of the attractive part of the scattering matrix element, V^-_{scat}:

$$V_{scat}^{-} = \iiint \phi^{\dagger e_2,f}_{\mathbf{k}_{e_2}+\mathbf{k}_{cm}}(\mathbf{r}_{e_2}) \Psi^{\dagger ex,f}_{0,\kappa,\vec{0}}(\rho)\ V_s(\rho_-)\ \Psi^{ex,i}_{0,\kappa,\mathbf{k}_{cm}}(\mathbf{R},\rho) \phi^{e_2,i}_{\mathbf{k}_{e_2}}(\mathbf{r}_{e_2}) d\mathbf{r}_{e_1} d\mathbf{r}_{e_2} d\mathbf{r}_h\ . \tag{6.44}$$

The definition of the wave function $\Psi^{ex}_{m,\mathbf{k}_{cm},\kappa}(\mathbf{R},\rho,\varphi)$ given by Eq. (6.40) combined with Eq. (6.44) leads to:

$$\begin{aligned} V_{scat}^{-} \;=\; & \frac{1}{\mathcal{A}^2} \iiint e^{i(\mathbf{k}_{e_2}+\mathbf{k}_{cm})\cdot\mathbf{r}_{e_2}} R_0(\rho,\kappa)\ V_s(\rho_-)\ e^{-i\mathbf{k}_{cm}\cdot(m_e\mathbf{r}_{e_1}+m_h\mathbf{r}_h)/M} \\ & \times R_0(\rho,\kappa) e^{-i\mathbf{k}_{e_2}\cdot\mathbf{r}_{e_2}} d\mathbf{r}_{e_1} d\mathbf{r}_{e_2} d\mathbf{r}_h\ , \end{aligned} \tag{6.45}$$

which gives:

$$\begin{aligned} V_{scat}^{-} = \frac{1}{\mathcal{A}^2} \iiiiint & d\mathbf{r}_{e_1} d\mathbf{r}_{e_2} d\mathbf{r}_h\ d\mathbf{q} d\mathbf{q}_-\ \exp[i(\mathbf{k}_{e_2}+\mathbf{k}_{cm})\cdot\mathbf{r}_{e_2}]\ \widetilde{R_0^2}(\mathbf{q},\kappa)\ \exp[i\mathbf{q}\cdot(\mathbf{r}_h-\mathbf{r}_{e_1})] \\ & \times \widetilde{V_s}(\mathbf{q}_-)\ \exp[i\mathbf{q}_-\cdot(\mathbf{r}_h-\mathbf{r}_{e_2})]\ \exp[-i\mathbf{k}_{cm}\cdot(m_e\mathbf{r}_{e_1}+m_h\mathbf{r}_h)/M]\ \widetilde{R_0^2}(\mathbf{q},\kappa)\ \exp[-i\mathbf{k}_{e_2}\cdot\mathbf{r}_{e_2}], \end{aligned} \tag{6.46}$$

considering the following definitions of the Fourier transform for the square of the relative motion part of the excitonic wave function Eq. (6.29) and the scattering potential $V_s(\rho_-)$ Eq. (6.4):

$$\begin{cases} R_0^2(\rho,\kappa) = \int \widetilde{R_0^2}(\mathbf{q},\kappa)\ e^{i\mathbf{q}\cdot(\mathbf{r}_h-\mathbf{r}_{e_1})} d\mathbf{q} \\ \\ V_s(\rho_-) = \int \widetilde{V_s}(\mathbf{q}_-,\kappa)\ e^{i\mathbf{q}_-\cdot(\mathbf{r}_h-\mathbf{r}_{e_2})} d\mathbf{q} \end{cases} \tag{6.47}$$

The 10-dimensional integral Eq. (6.46) can be simplified using the identity: $\int e^{iq.x} dq = \delta(x)$, and doing the same calculations with V_{scat}^{+}, Eq. (6.43) can be reduced to the following expression in the Fourier space:

$$V_{scat}(\mathbf{k}_{cm},\kappa) = \frac{1}{\mathcal{A}} \left(\widetilde{R_0^2}(-\frac{m_e}{M}\mathbf{k}_{cm},\kappa) \widetilde{V_s}^{-}(\mathbf{k}_{cm}) + \widetilde{R_0^2}(\frac{m_h}{M}\mathbf{k}_{cm},\kappa) \widetilde{V_s}^{+}(\mathbf{k}_{cm}) \right)\ . \tag{6.48}$$

Eq. (6.48) combined with Eq. (6.41) can finally be written as follows:

$$V_{scat}(\mathbf{k}_{cm},\kappa) = \frac{e^2}{2\epsilon\mathcal{A}}\frac{1}{k_{cm}+q_s}\left(\widetilde{R_0^2}(-\frac{m_h}{M}\mathbf{k}_{cm},\kappa) - \widetilde{R_0^2}(\frac{m_e}{M}\mathbf{k}_{cm},\kappa)\right) . \tag{6.49}$$

Since the scattering phase shift and the amplitude of the wave function have to be evaluated solving numerically the phase and the amplitude equations, Eqs. (6.30) and (6.34), $V_{scat}(\mathbf{k}_{cm},\kappa)$ in Eq. (6.49) has to be also evaluated numerically.

6.4.4 Fermi's golden rule

The scattering matrix element describing how the free carriers scatter with the $1s$ excitons being calculated, the next step consists of evaluating the spontaneous emission rate due to the correlated particles in the plasma.

The distributions of correlated particles, $N_{\mathbf{K}}$, and free carriers, $N_{\mathbf{k}_2}$, are given by (see Appendix E):

$$\begin{cases} N_{\mathbf{K}} = \dfrac{2\pi\beta\hbar^2}{M}\ (1-\alpha)N\ \exp\left(-\beta\ \dfrac{\hbar^2K^2}{2M}\right) \\ \\ N_{\mathbf{k}_2} = \dfrac{2\pi\beta\hbar^2}{m_e}\ \alpha N\ \exp\left(-\beta\ \dfrac{\hbar^2k_2^2}{2m_e}\right) \end{cases} \tag{6.50}$$

$N_{\mathbf{K}}$ is the approximated distribution of the $1s$ excitons for a wide-gap semiconductor at room temperature.

The contribution of the correlated particles in the plasma, R_{sp}^{corr}, is calculated combining Eqs. (6.6), (6.7) and (6.50):

$$\begin{aligned} R_{sp}^{corr}(\hbar\Omega) &= \frac{2\pi}{\hbar}\left(\frac{4\pi\beta_1\Omega/\omega_0}{(1-\Omega^2/\omega_0^2)^2+4\pi\beta_1}\right) \\ &\times\sum_{\mathbf{K}}\left[\frac{2\pi\beta\hbar^2}{M}\ (1-\alpha)N\ \exp\left(-\beta\ \frac{\hbar^2K^2}{2M}\right)\ |V_{scat}(K)|^2\right. \\ &\left.\times\sum_{\mathbf{k}_2}\frac{2\pi\beta\hbar^2}{m_e}\ \alpha N\ \exp\left(-\beta\frac{\hbar^2k_2^2}{2m_e}\right)\ \delta\left(E_g-E_b^{ex}+\frac{\hbar^2K^2}{2M}-\hbar\Omega-\frac{\hbar^2}{2m_e}(K^2+2\mathbf{K}.\mathbf{k}_2)\right)\right] , \end{aligned} \tag{6.51}$$

where N is the plasma density. The first step of the calculation of Eq. (6.51) is the evaluation of the discrete sum over all the vectors $\mathbf{k}_2$. To do so, one can approximate the sum S:

$$S = \sum_{\mathbf{k}_2} \exp\left(-\beta \frac{\hbar^2 k_2^2}{2m_e}\right) \delta\left(E_g - E_b^{ex} + \frac{\hbar^2 K^2}{2M} - \hbar\Omega - \frac{\hbar^2}{2m_e}(K^2 + 2\mathbf{K}.\mathbf{k}_2)\right) , \quad (6.52)$$

by a 2D integral:

$$\begin{aligned} S &= \frac{\mathcal{A}}{4\pi^2} \int_{k_2^{min}}^{k_2^{max}} \int_0^{2\pi} k_2 \ \exp\left(-\beta \frac{\hbar^2 k_2^2}{2m_e}\right) \\ &\quad \times \delta\left(E_g - E_b^{ex} + \frac{\hbar^2 K^2}{2M} - \hbar\Omega - \frac{\hbar^2}{2m_e}(K^2 + 2Kk_2\cos\theta)\right) \ dk_2 d\theta \ . \quad (6.53) \end{aligned}$$

The integral over θ can be calculated:

$$\int_0^{2\pi} \delta(X - Y\cos\theta) d\theta = \frac{2}{|Y \sin[\cos^{-1} X/Y]|} \quad (6.54)$$

if $|X| < |Y|$.

Defining $X = E_X - \hbar\Omega - \hbar^2 K^2/2m_e$ and $Y = \hbar^2 K k_2/m_e$, and with the above condition on X and Y, the limits of the integral Eq. (6.53) are:

$$\begin{cases} k_2^{min} = \dfrac{m_e}{\hbar^2 K}\left(E_X - \hbar\Omega - \dfrac{\hbar^2}{2m_e}K^2\right) \\ \\ k_2^{max} \to \infty \end{cases} \quad (6.55)$$

Thus

$$\begin{aligned} &\int_0^{2\pi} \delta\left(E_g - E_b^{ex} + \frac{\hbar^2 K^2}{2M} - \hbar\Omega - \frac{\hbar^2}{2m_e}K^2 - \frac{\hbar^2}{m_e}Kk_2\cos\theta\right) d\theta \\ &= \frac{2}{\left|\dfrac{\hbar^2}{m_e}Kk_2 \sin\left[cos^{-1}\left(\dfrac{E_X - \hbar\Omega - \hbar^2K^2/2m_e}{\hbar^2 K k_2/m_e}\right)\right]\right|} \ . \quad (6.56) \end{aligned}$$

Considering the identity $|\sin[\cos^{-1}\Theta]| = \sqrt{1 - \cos^2[\cos^{-1}\Theta]} = \sqrt{1 - \Theta^2}$ and

combining Eqs. (6.53) and (6.56) lead to:

$$S = \frac{\mathcal{A}}{2\pi^2} \int_{k_2^{min}}^{\infty} \frac{k_2 \ \exp\left(-\beta \ \dfrac{\hbar^2 k_2^2}{2m_e}\right) dk_2}{\left(\hbar^4 K^2 k_2^2/m_e^2 - (E_X - \hbar\Omega - \hbar^2 K^2/2m_e)^2\right)^{1/2}} \ . \tag{6.57}$$

With two successive changes of variables: $K_2 = k_2^2$ and $K_2' = K_2/k_2^{min^2}$, Eq. (6.57) becomes:

$$S = \frac{\mathcal{A} m_e k_2^{min}}{4\pi^2\hbar^2 K} \int_1^{\infty} \frac{\exp\left(-\beta \dfrac{\hbar^2 k_2^{min^2}}{2m_e} K_2'\right)}{\left(K_2' - 1\right)^{1/2}} \ dK_2' \ . \tag{6.58}$$

Eq. (6.58) can be easily calculated if one considers the following identity:

$$\int_1^{\infty} \frac{e^{-\mu x}}{(x-1)^{1/2}} \ dx = \sqrt{\frac{\pi}{\mu}} \ e^{-\mu} \ .$$

Indeed, we find:

$$S = \frac{\mathcal{A} m_e k_2^{min}}{4\pi^2\hbar^2 K} \left(\frac{2\pi m_e}{\beta\hbar^2 k_2^{min^2}}\right)^{1/2} \exp\left(-\beta \ \frac{\hbar^2 k_2^{min^2}}{2m_e}\right) \ . \tag{6.59}$$

Finally, approximating the discrete sum over all the vectors $\mathbf{K}$ by an integral and inserting Eq. (6.59) into Eq. (6.51) lead to the following expression of the spontaneous emission rate, $R_{sp}^{corr}(\hbar\Omega)$, due to the scattering of free electrons with $1s$ excitons:

$$\begin{aligned} R_{sp}^{corr}(\hbar\Omega) \ &= \ \sqrt{\frac{2\pi m_e \beta^3}{M^2}} \left(\frac{4\pi\beta_1\Omega/\omega_0}{(1-\Omega^2/\omega_0^2)^2 + 4\pi\beta_1}\right) \alpha(1-\alpha)N^2 \\ \times \int_0^{\infty} e^{-\beta\dfrac{\hbar^2 K^2}{2M}} |V_{scat}(K)|^2 e^{-\beta\dfrac{m_e}{2\hbar^2 K^2}\left(E_g - E_b^{ex} - \hbar\Omega - \dfrac{m_h}{m_e}\dfrac{\hbar^2 K^2}{2M}\right)^2} dK \ . \end{aligned} \tag{6.60}$$

The contribution of the correlated particles in the exciton/electron-hole plasma to the spontaneous emission rate appears explicitly: both the degree of ionization α

and the scattering matrix element V_{scat} in Eq. (6.49) give the information we need. $R_{sp}^{corr}(\hbar\Omega)$ has to be evaluated numerically.

6.5 Numerical results

The wavefunctions are evaluated for various plasma densities. In the table given below, we give the values of the corresponding screening parameter and degree of ionization (taken from Ref. [83]).

$GaAs$					
$q_s a_B^*$	2.5	1.25	1.0	0.32	0.10
$N(10^{11}\text{cm}^{-2})$	4.27	2.06	1.62	0.48	0.14
$\alpha(N)$	0.741935	0.769433	0.781595	0.856583	0.928092
$ZnSe$					
$q_s a_B^*$	2.5	1.25	1.0	0.32	0.10
$N(10^{11}\text{cm}^{-2})$	13.31	8.0	6.78	2.51	0.66
$\alpha(N)$	0.49682	0.412371	0.389361	0.339291	0.410779

6.5.1 The 2D exciton wavefunction

In this section we show the solution of Eqs. (6.34) and (6.30) computed for two values of the plasma densities. The radial wavefunctions, $R_0(\rho)$, shown in Fig. 6.3, are the $1s$ 2D exciton wavefunctions.

At low density, i.e. $q_s a_B = 0.1$, the screening effect is small and the binding energy high (about a 2D Rydberg). Hence, the probability of having a bound electron/hole pair is high when their relative distance is small, i.e. $\leq a_B$. However, at very low density, it is not very likely that an electron and hole will meet and form a bound state. This explains the fast decay of the wavefunction as the relative distance increases (over a_B). At high density, i.e. $q_s a_B = 2.5$, it is more likely that electrons and holes will form bound states. Thus, the wavefunction has a slower decay. But with increasing the plasma density, the plasma screening becomes more important. A consequence of high plasma screening is a very low exciton binding

energy. This explains why the wavefunction is lower when $q_s a_B = 2.5$ than when $q_s a_B = 0.1$ for small relative distances.

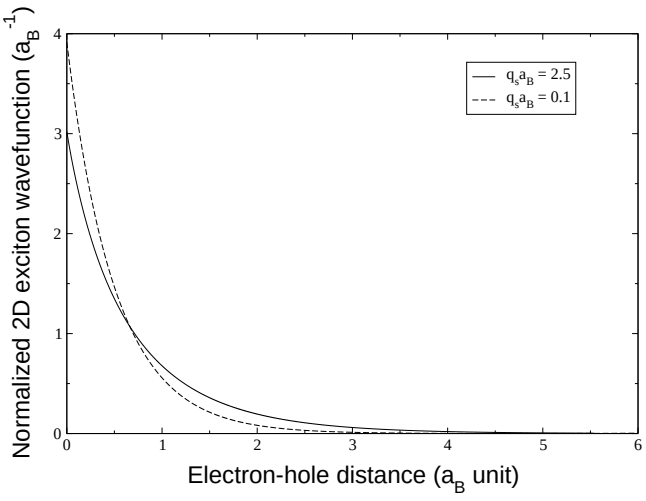

Figure 6.3: Normalized 2D exciton wavefunction as a function of the distance between the electron and the hole, in exciton Bohr radius unit.

6.5.2 The scattering matrix

In Fig. 6.4 we show the behaviour of the scattering matrix versus k_{cm}, for the same two values of the plasma screening: $q_s a_B = 0.1$ and $q_s a_B = 2.5$.

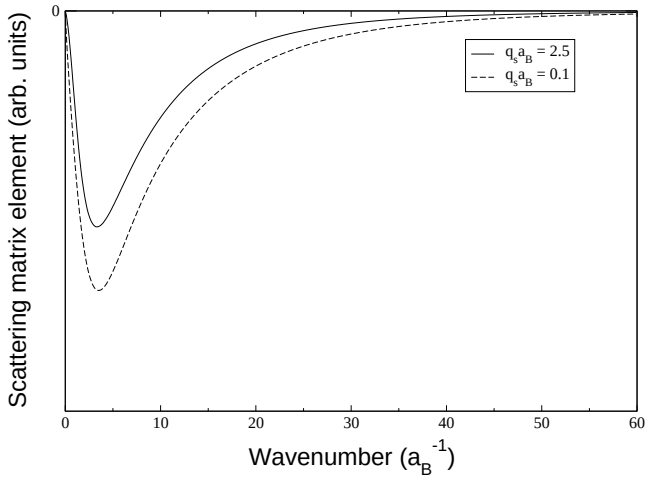

Figure 6.4: Scattering matrix element as function of wavenumber, describing the $1s$ exciton-electron scattering with a screened Coulomb potential.

In both cases, the qualitative behaviour of V_{scat} is the same: for low values of

the wavenumber (up to about 3 a_B^{-1}), V_{scat} is a decreasing function which reaches a minimum for the same value of k_{cm}. Then, for values greater than 3 a_B^{-1}, V_{scat} is an increasing function of k_{cm}. The main difference between V_{scat} calculated for $q_s a_B$ = 0.1 and for $q_s a_B$ = 2.5 is the amplitude: it is greater for low screening. This is due to the fact that the Coulomb potential is smaller for high plasma screening. In this case, the scattering potential being small, the scattering matrix is small too. For large values of $k_{cm} \geq 30\ a_B^{-1}$, the distance between the electron and the hole forming the exciton is very small and the free electron would see this bound system as a neutral quasi-particle that it cannot scatter with.

6.5.3 The free carrier contribution to the spontaneous emission rate

In section 6.3, we stopped our calculations when we obtained $R_{sp}^{fc}(\hbar\Omega)$ as a function of the fugacities $z_e = e^{\beta\mu_e}$ and $z_h = e^{\beta\mu_h}$, in Eq. (6.15). In section 6.4.1, we obtained the expression of the uncorrelated density, N_a^0, in the low density limit, in Eq. (6.21). As N_a^0 is an explicit function of the fugacity $z_a = e^{\beta\mu_a}$, it is possible to modify the expression of $R_{sp}^{fc}(\hbar\Omega)$ in Eq. (6.21) to obtain the free carrier spontaneous emission rate as a function of the plasma density.

From Eq. (6.21) we obtain:

$$z_a = e^{\beta\mu_a} = 1 - \sqrt{1 - 2\frac{\lambda_{m_a}^2}{g_a}\ N_a^0}\ . \tag{6.61}$$

Then, from Eqs. (6.3), (6.15) and (6.61) we deduce the final expression for the spontaneous emission rate in a 2D noninteracting electron-hole plasma:

$$\begin{aligned} R_{sp}^{fc}(\hbar\Omega) \ &= \ \frac{\hbar^2}{m_r \tau_R}\left(1 - \sqrt{1 - \lambda_{m_e}^2 \alpha_e(N) N}\ \right)\left(1 - \sqrt{1 - \lambda_{m_h}^2 \alpha_h(N) N}\ \right) \\ &\quad \times \lim_{\eta \to 0} \int_0^\infty k\ \exp\left(-\beta\ \frac{\hbar^2 k^2}{2m_r}\right) \frac{\eta}{(E_g + \dfrac{\hbar^2 k^2}{2m_r} - \hbar\Omega)^2 + \eta^2}\ dk, \end{aligned} \tag{6.62}$$

where the broadening in the spectrum is modeled taking the limit of a Lorentzian

function for the delta function in Eq. (6.5).

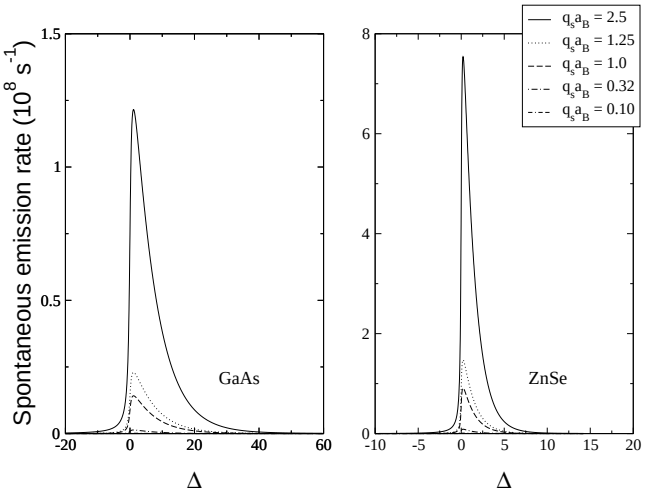

Figure 6.5: Spontaneous emission rate evaluated for $GaAs$ and $ZnSe$ in the Boltzmann regime for $T = 300K$. The corresponding values of the densities for the screening parameters are given in Tab.(6.1). Note that the spontaneous emssion rate in $ZnSe$ is much bigger than it is for $GaAs$.

The free carrier spontaneous emission rate, $R_{sp}^{fc}(\hbar\Omega)$, decreases with decreasing the plasma density at a given temperature. $R_{sp}^{fc}(\hbar\Omega)$ also depends on the material parameters such as the bandgap and the dielectric constant, through the presence of the radiative lifetime τ_{rad}. For $ZnSe$, τ_{rad} is bigger than for $GaAs$. Hence, it is more likely to observe photoluminescence with $ZnSe$-based materials than with $GaAs$. The PL spectra shows that for the same scaled density, and at a given temperature, the PL spectra are greater for $ZnSe$ than they are for $GaAs$.

6.5.4 The exciton contribution to the spontaneous emission rate

The numerical evaluation of Eq. (6.60) gives the exciton contribution to the spontaneous emission rate, due to exciton-electron scattering as shown in Fig. 6.6. The behaviour of $R_{sp}^{corr}(\hbar\Omega)$ reflects the behaviour of the scattering matrix: at high density, V_{scat} is small, then it is not likely that an exciton will find a partner to scatter with to reach the photon line. Comparing results obtained for $ZnSe$ and $GaAs$, it appears clearly that the exciton contribution to the spontaneous emission rate at room temperature is much more important in $Znse$ than it is in $GaAs$. This is due

to the fact that with a smaller dielectric constant the Coulomb forces are greater in $ZnSe$ which makes V_{scat} bigger.

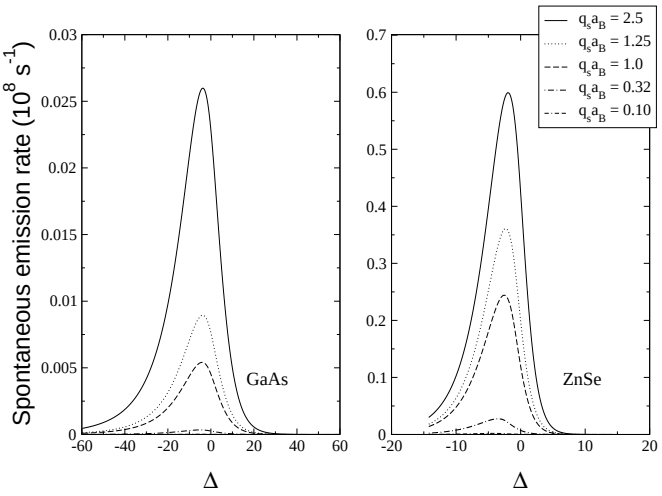

Figure 6.6: Contribution of the $1s$ exciton-electron scattering to the spontaneous emission rate evaluated for $GaAs$ and $ZnSe$ in the Boltzmann regime for $T = 300K$. The corresponding values of the densities for the screening parameters are given in Tab. 6.1. Note that the contribution of the correlations to the spontaneous emssion rate in $ZnSe$ is much more important for $ZnSe$ than it is for $GaAs$.

Also, because of the large exciton binding energy, the exciton contribution to the spontaneous emission rate is much more important for $ZnSe$ than it is for $GaAs$ (about 20 times), as at room temperature there is barely no exciton in a $GaAs$ electron/hole plasma.

6.5.5 The total spontaneous emission rate

In Fig. 6.7, we obtain the total luminescence spectra by simply adding both contributions. Here, the spontaneous emission rates are shown normalized in order to compare the relative importance of the contribution of the $1s$ exciton-electron scattering contribution for various densities.

A significant peak appears below the band edge only for $ZnSe$. As mentioned earlier, this is due to the more important exciton population at room temperature because of the large binding energy and greater scattering matrix. Hence, $GaAs$ and $ZnSe$ have different qualitative behaviours at room temperature: excitonic processes

have to be taken into account for $ZnSe$. The lower the density is, the lower the plasma screening is and the stronger the Coulomb interaction is; moreover, the free-carrier spontaneous emission rate rapidly decreases with a decreasing density. This explains why one sees an exciton peak becoming relatively more important at low density. However, if one looks carefully, one can see that the exciton peak is more important for $q_s a_B^* = 0.32$ than it is for $q_s a_B^* = 0.10$. This reflects the nonmonotonical behaviour of the ionization degree as a function of density for $ZnSe$: one can see clearly in Fig. 6.2, the presence of a minimum at low density.

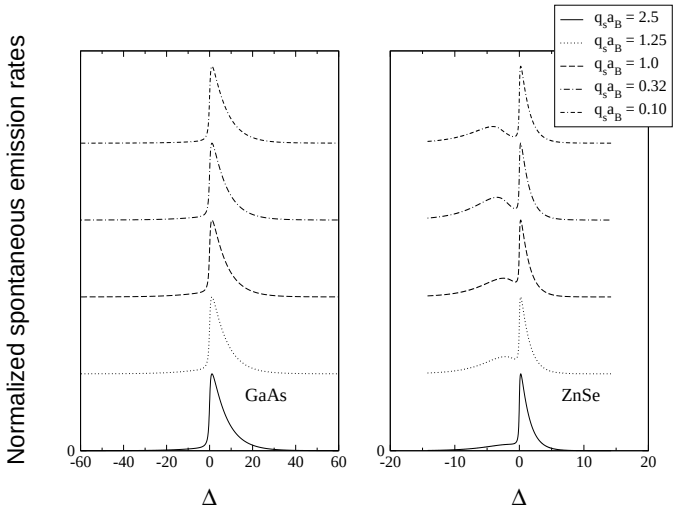

Figure 6.7: Total spontaneous emission rate evaluated for $GaAs$ and $ZnSe$ in the Boltzmann regime for $T = 300K$. The corresponding values of the densities for the screening parameters are given in Tab.(6.1). Note that the excitonic contribution at 300 K is only significant for $ZnSe$ because of the large exciton binding energy for this material.

6.6 Discussion and conclusion

Our approach was based on an accurate study of the thermodynamical properties of a 2D exciton/electron-hole plasma in which two types of densities are defined: correlated and uncorrelated, Eqs. (6.21) and (6.23). Some analytical results were quickly found in the case of a free carrier plasma. Eq. (6.62) giving the spontaneous emission rate as a function of the products of the total density and the ionisation degrees showed that even if the behaviour of the ionization degree is qualitatively

different from $GaAs$ for $ZnSe$, spectra are qualitatively the same for both types of semiconductors. This could be expected since we only dealt with the contribution of the free carrier plasma. Nevertheless, we could evaluate the separation of the quasi-Fermi levels which is now directly known from the calculation of the degrees of ionization, Eq. (6.27), for which the modified law of mass action, Eq. (6.23), was used.

Concerning the contribution of the correlated quasiparticles in the plasma, most of the attention was paid to the $1s$ exciton-free electron scattering process for mainly two reasons: on the one hand, this is the most likely process leading to the photoluminescence due to correlated quasiparticles at room temperature, and on the other hand, it is really convenient for analytical calculations and numerical work. The exciton distribution was approximated by taking the distribution of all the correlated quasiparticles given by Eq. (6.50) into account. It obviously gives an overestimation of the number of the bound states in the plasma, but it is reasonable to think that it is a good approximation for a wide-gap semiconductor. Indeed, in this case the scattering part of the partition function is small compared to the bound state part [83] and at room temperature the exciton population remains important.

The function, V_{scat}, representing the scattering matrix describing the $1s$ exciton-hole scattering was found to be the exact opposite of the one for the 1s exciton-electron scattering. But, because of the conservation of energy, the domain of definition of this function in the Fourier space is restricted to the small values of the wavenumber which clearly gives very small values for the scattering element. A simple way to picture this result is to consider that because of its heavy effective mass, it is less likely that a hole will meet a partner to scatter with in the low-density exciton/electron-hole plasma. Thus, this process was not taken into account in this work.

When the correlated part is added to the free carrier PL spectra a significant peak appears below the band edge for $ZnSe$ whereas we do not observe any significant change for $GaAs$. So, the simple model proposed in Ref. [40] clearly needed to

be extended to account for excitons and hence to describe PL spectra for wide-gap materials such as $ZnSe$. The relative height of the excitonic peak is not a simple function of the plasma density as it depends on the value of the ionization degree which is not a monotonic function of the density.

Chapter 7

Conclusion

In this thesis, we developed a model to describe the many-body effects in semiconductor quantum wells and the role they play in the absorption phenomenon. The optical properties of semiconductors and their connections to the thermodynamic properties of the quasi-2D electron-hole plasma were studied in both nonequilibrium and equilibrium regimes.

We began in chapter 2 by giving an overview of the electronic and thermodynamic properties of semiconductor quantum wells in the quasi-equilibrium regime. We considered the finite width of the quantum wells, introducing a form factor to account for the alteration of the Coulomb potential energy in real heterostructures. However, we assumed the 2D formulas to be valid to compute the chemical potentials. We also made the assumption that the electron gas and heavy hole gas densities, as well as their temperatures, were the same. Using the static plasmon-pole approximation to account for the screening in the electron/hole plasma allowed analytical calculations which simplified the numerical work in the next chapters. We showed the main steps for the derivation of the semiconductor Bloch equations assuming that the screened Hartree-Fock approximation was sufficient to describe the connection between the thermodynamics of the electron/hole plasma and its optical properties.

In chapter 3, we illustrated in detail the calculations presented in chapter 2. We studied the interplay between the Fermionic nature of the carriers and the Coulombic forces that acts on them, and saw how the Coulomb many-body effects as well as the Pauli blocking strongly influence the shape of the absorption spectra. Comparing the numerical results for two different type of material, mid-gap $GaAs$ and wide-gap $ZnSe$, we obtained further insight on the role played by the Coulomb

interaction on the optical properties of semiconductor: Coulomb enhancement and bandgap renormalization are more important in $ZnSe$ than they are in $GaAs$. The effect of a finite well width was also taken into account and we showed that the strength of the 2D Coulomb interaction is smaller in real heterostructures than it is in an ideal 2D electron/hole system. Hence, the exciton binding energy is not exactly four times the value of the Rydberg energy, but a decreasing function of the well width. The introduction of the non-degenerate valence bands in the calculations was necessary to account for the light hole exciton resonance that one can observe on experimental absorption spectra. We saw that the static plasmon-pole approximation yields an overestimation of the bandgap shrinkage as numerical results exhibits a slight redshift of the exciton resonances (see also Ref. [42]). All the calculations and numerical results presented in this chapter were done assuming a quasi-equilibrium situation defined by $\mu_{lh} = \mu_{hh} \neq \mu_e$ and $T_e = T_{hh}$, i.e. $N_{lh} \approx 0$ and $N_e = N_{hh}$: the intraband scattering has led to a fast equilibration of the initial carriers distributions within the bands and the plasma cooling has led to a cooling of the carriers temperatures down to the lattice temperature. We chose the lattice temperature to be $T = 77$ K to avoid the unphysical behaviour of the numerical solutions of the SBE in order to explore the high density regime.

In chapter 4, we constructed a simple model to describe the time evolution of the quasi-2D electron/hole plasma. Several dynamical effects were included: relaxation of the carrier distributions, thermalization, plasma cooling, carrier spin-flip, recombination (radiative and nonradiative) and light hole scattering into heavy holes. A full microscopic treatment of all these effects being computationally prohibitive, we chose a phenomenological approach using rate equations. We considered spin-selective excitations via optical pumping. Some of the scattering times, such as the spin-flip times, were taken from available experimental data presented in chapter 5. The time dependence of the density, energy and temperature of each spin-polarised gas was described, and we obtained insight in the interplay between the processes mentioned above. In particular, we saw that the light hole gases do not reach ther-

modynamical equilibrium with the other carrier gases, nor with the lattice: the light hole density decay being very fast compared to the other processes, the light hole gases effective temperatures keep increasing far beyond the lattice temperature. We also found that we could address the problem of the time dependence of the plasma screening in a simple fashion, using quasi-equilibrium formulas in the long wavelength limit.

The results found in chapter 4 were used to study the time evolution of the absorption spectra in chapter 5. We focused on the heavy and light hole excitons bleaching and shift dynamics. By comparing our numerical results with available experimental data, we attempted to extract a time scale for the carrier spin-flip times. Except for the energy shift of the OCP heavy hole exciton, the numerical results are in good qualitative agreement with the experiment. According to our calculations, the spin populations equilibrate on a much longer time scale (30 ps) than the thermalization of the electron/hole plasma (1 ps). The plasma cooling enhances the plasma screening and together with the relaxation of the distributions also enhances the Pauli blocking effect. These processes are amongst the fastest and we can observe their influence on the early behaviour of the exciton peaks bleaching and energy shift. The spin-flip process leads to opposite qualitative behaviours of the bleaching dynamics, depending on the initial polarisation configurations. The exciton peaks bleaching and shift can either increase or decrease because of the spin-flip process depending on the type of exciton (heavy or light) and the polarisations OCP or SCP. The radiative recombination occurs on a time scale that is too large (about 1.6 ns in $ZnSe$) to have any effect on the fast bleaching and energy shift dynamics (below 100 ps). However, the nonradiative recombination is fast enough to observe an overall decay on a time scale shorter than 100 ps. As far as the energy shift is concerned, the screening model that we used for this work seems to be not good enough to describe at least qualitatively the OCP energy shift. The static plasmon-pole approximation leads to an overestimation of the bandgap shrinkage [42], which in turn leads to an important OCP heavy hole exciton peak redshift that

is not observed on experimental data. As far as the SCP heavy hole exciton peak is concerned, the evaluated exciton binding energy for finite densities is too small because of the screening model we use. This explains, the initial large blueshift despite the important bandgap renormalisation in the SCP case. As for the SLP configuration, the static plasmon-pole approximation is good enough to describe the balance between the bandgap shrinkage and the exciton binding energy for finite plasma densities.

In this thesis, we essentially focused our efforts on computing absorption spectra in $ZnSe$-based quantum wells. However, the computer codes we developped can also be used to produce refractive index spectra in both equilibrium and nonequilibrium regimes. Moreover, as we saw in chapter 3 with $GaAs$, we can also feed the codes with material parameters other than those of $ZnSe$, and it is possible to explore a wide domain in density and temperature. With our model, it is possible to control the values of the phenomenological parameters in order to obtain more understanding in the interplay between various dynamical processes and/or fit experimental data. More experiments need to be carried out to obtain reliable data for the light hole exciton dynamics. At the present time, we cannot produce more conclusive results for the light hole exciton dynamics as we cannot compare numerical data with experiments.

As we saw in chapter 3, the evaluation of the Coulomb matrix elements is difficult and hence time consuming. In the case of the nonequilibrium regime, they need to be computed at each time step, which make the execution time for the codes very long. This is the reason why we chose to work with a statically screened Coulomb potential which can be treated analytically, whereas the dynamical screening is much more complicated and more demanding numerically. However, if one wishes to avoid the problem of the large redshift of the exciton peak leading to the results described in chapter 5, one would need to use a dynamically screened Coulomb potential in the calculations [42]. Another time consuming process, is the numerical treatment of the nonequilibrium problem. We chose in this work the simplest approach possible

to account for various dynamical processes, but the approximation for the light holes scattering into the heavy hole band is too simple and would require some improvement.

In chapter 6, we constructed a simple model to study the influence of Coulomb correlations on the photoluminscence phenomenon. We computed the spontaneous emission rate taking into account the $1s$ exciton-free electron scattering at room temperature. We found that the contribution of the excitons to the PL spectra is negligible for low- and mid-gap materials such as $GaAs$, whereas it is significant in the case of a wide-gap semiconductor such as $ZnSe$, because of the strong exciton binding energy comparable to k_BT at room temperature. The calculation of the $1s$ exciton-free electron scattering included direct terms only, so a suggestion for further work would be to account for the exchange terms. To evaluate the exciton and the free carriers populations, we used the ionization degree calculated with the modified law of mass action. The $1s$ exciton population was overestimated, but it remained a good approximation for our purposes. It is possible to calculate the wavefunctions of the exciton states (bound and unbound) other than the $1s$ in order to account for most of the correlations in the electron-hole plasma, but calculating their populations remains to be done. Working at room temperature the vibrations in the lattice are important, i.e. the phonon population is important. It is then very likely that the correlations between the carriers in the plasma are affected by the scattering with the phonons which is really faster compared to the time taken for the other processes such as exciton-free carrier scattering. Clearly, we have to deal with two different time scales. This means that we can consider the processes involving phonons as a noise affecting the correlations between the charged particles. A stochastic equation of the Langevin type could be derived in order to evaluate the effect of the phonons at room temperature on the correlations. Finally, if one is interested in the low temperature regime with a simple model, one should extend the calculations presented above to the degenerate limit.

Appendix A

Plasma screening in the static plasmon-pole approximation

In chapters 3 and 5 we solved numerically the semiconductor Bloch equations in the screened Hartree-Fock approximation. For reasons already mentioned in the main text we chose to use a rather simple model for the plasma screening: we simplify the Lindhard formula using the static plasmon-pole approximation. In this appendix we give physical and mathematical detail that was omitted in the main text. We want to evaluate the effect of a test charge whose location defines the origin in an electron gas, i.e. how it affects the carrier distribution $n(\mathbf{r}) = \delta^3(\mathbf{r})$ which in turn modifies the electrostatic potential $U(r)$. The approach presented here uses a self-consistent quantum theory of plasma screening involving arguments from classical electrodynamics and quantum mechanics (see Refs. [11, 44]).

A.1 Derivation of the Lindhard formula

The screened density distribution operator in an electron gas is given by the product of two electron field operators:

$$\hat{n}^s(\mathbf{r}) = \hat{\psi}^\dagger(\mathbf{r})\hat{\psi}(\mathbf{r}) = \frac{1}{\mathcal{V}} \sum_{\mathbf{k},\mathbf{k}'} e^{i(\mathbf{k}-\mathbf{k}').\mathbf{r}} a^\dagger_{\mathbf{k}'} a_{\mathbf{k}} = \sum_{\mathbf{q}} \hat{n}^s_{\mathbf{q}} e^{i\mathbf{q}.\mathbf{r}} \ , \tag{A.1}$$

where

$$\hat{n}^s_{\mathbf{q}} = \frac{1}{\mathcal{V}} \sum_{\mathbf{k}} a^\dagger_{\mathbf{k}-\mathbf{q}} a_{\mathbf{k}} \tag{A.2}$$

is the Fourier amplitude of the density distribution operator and $\mathcal{V}$ the volume of the semiconductor medium. The sums $\sum_{\mathbf{k}}$ contain the summation over the spin-states to avoid onerous notations.

The determination of the density distribution $n^s_{\mathbf{q}}$ involves the solution of the equation of motion for $\hat{n}^s_{\mathbf{q}}$. The effective single-particle Hamiltonian is:

$$H_{eff} = \sum_{\mathbf{k}} \epsilon_{\mathbf{k}} a^\dagger_{\mathbf{k}} a_{\mathbf{k}} + \mathcal{V} \sum_{\mathbf{q}} V^s_q \hat{n}^s_{-\mathbf{q}} \ , \tag{A.3}$$

where

$$V^s_q = \frac{1}{\mathcal{V}} \int d^3 r V^s(r) e^{-i\mathbf{q}.\mathbf{r}} \ . \tag{A.4}$$

The screened Coulomb potential energy $V^s(r)$ is simply given by:

$$V^s(r) = eU^s(r) \ , \tag{A.5}$$

where $U^s(r)$ is the screened electrostatic potential that describes the the electrostatic potential modified by the presence of a test charge in an electron gas taking into account the background dielectric constant of the semiconductor medium. One can calculate $U^s(r)$ from Poisson's equation as we shall see. First, we need to calculate $n^s_{\mathbf{q}} = \langle \hat{n}^s_{\mathbf{q}} \rangle$. We start from Heisenberg equation for each product $a^\dagger_{\mathbf{k-q}} a_{\mathbf{k}}$:

$$\begin{aligned} i\hbar \frac{d}{dt} \, a^\dagger_{\mathbf{k-q}} a_{\mathbf{k}} &= [a^\dagger_{\mathbf{k-q}} a_{\mathbf{k}}, H_{eff}] \\ &= (\epsilon_{\mathbf{k}} - \epsilon_{\mathbf{k-q}}) \, a^\dagger_{\mathbf{k-q}} a_{\mathbf{k}} + \sum_{\mathbf{q'}} V^s_{q'} \left(a^\dagger_{\mathbf{k-q}} a_{\mathbf{k+q'}} - a^\dagger_{\mathbf{k-q-q'}} a_{\mathbf{k}} \right) \ . \end{aligned} \tag{A.6}$$

Because of the product of $V^s_{q'}$ with terms like $a^\dagger a$, products of four operators appear. The simplest treatment of this problem as we have already seen in the main text is to use the RPA (see the derivation of the SBE in section 2.3.1 and Eq. (2.49) in particular). So, taking the expectation value and only keeping the slowly varying term, i.e. those with $\mathbf{q'} = -\mathbf{q}$ leads to:

$$i\hbar \frac{d}{dt} \, \langle a^\dagger_{\mathbf{k-q}} a_{\mathbf{k}} \rangle = (\epsilon_{\mathbf{k}} - \epsilon_{\mathbf{k-q}}) \, \langle a^\dagger_{\mathbf{k-q}} a_{\mathbf{k}} \rangle + V^s_q (n_{\mathbf{k-q}} - n_{\mathbf{k}}) \ . \tag{A.7}$$

To go further we make the following assumption: $\langle a^\dagger_{\mathbf{k-q}} a_{\mathbf{k}} \rangle$ varies like $e^{(\delta - i\omega)t}$.

The infinitesimal quantity δ indicates an adiabatic switch-on of the test charge potential. We also assume that the induced charge distribution has the same time dependence. So, from Eq. (A.7) we obtain:

$$n^s_{\mathbf{q}} = \langle a^\dagger_{\mathbf{k}-\mathbf{q}} a_{\mathbf{k}} \rangle = V^s_q \, \frac{n_{\mathbf{k}-\mathbf{q}} - n_{\mathbf{k}}}{\hbar(\omega + i\delta) + \epsilon_{\mathbf{k}-\mathbf{q}} - \epsilon_{\mathbf{k}}} \; . \tag{A.8}$$

Now that we know $n^s_{\mathbf{q}}$ we can solve Poisson's equation which reads:

$$\nabla^2 U^s(r) = -\frac{e}{\epsilon} \left(n(\mathbf{r}) + n^s(\mathbf{r}) \right) \; , \tag{A.9}$$

in real space. In Fourier space Eq. (A.9) becomes:

$$U^s_q = \frac{e}{\epsilon q^2} \left(\frac{1}{\mathcal{V}} + n^s_{\mathbf{q}} \right) \; , \tag{A.10}$$

as

$$n_{\mathbf{q}} = \frac{1}{\mathcal{V}} \int d^3r \; \delta^3(\mathbf{r}) e^{-i\mathbf{q}.\mathbf{r}} = \frac{1}{\mathcal{V}} \; . \tag{A.11}$$

As $V^s_q = eU^s_q$, we can insert Eq. (A.8) into Eq. (A.10) and solve for V^s_q to find:

$$V^s_q(\omega) = V_q \left[1 - V_q \sum_{\mathbf{k}} \; \frac{n_{\mathbf{k}-\mathbf{q}} - n_{\mathbf{k}}}{\hbar(\omega + i\delta) + \epsilon_{\mathbf{k}-\mathbf{q}} - \epsilon_{\mathbf{k}}} \right]^{-1} \; , \tag{A.12}$$

where V_q is the Fourier transform of the unscreened Coulomb potential $V(\mathbf{r})$. One has to note that here, $V^s_q(\omega)$ is the dynamically screened Coulomb potential as it is also function of ω. This ω dependence comes from the the dynamic dielectric function $\epsilon_q(\omega)$:

$$\epsilon_q(\omega) = 1 - V_q \sum_{\mathbf{k}} \; \frac{n_{\mathbf{k}-\mathbf{q}} - n_{\mathbf{k}}}{\hbar(\omega + i\delta) + \epsilon_{\mathbf{k}-\mathbf{q}} - \epsilon_{\mathbf{k}}} \; . \tag{A.13}$$

Eq. (A.13) is the full RPA dielectric function also known as the Lindhard formula that is described in chapter 2, section 2.1.3. In the more general case of an electron-hole plasma, one can simplify the problem by assuming that the total screening is given by the sum of the effects resulting from the separate electron and holes

plasmas[1]. As such we also neglect the excitonic screening which at high enough plasma density is a good approximation. Eq. (A.13) then becomes:

$$\epsilon_q(\omega) = 1 - V_q \sum_{\mathbf{k}} \sum_{c} \frac{n_{c,\mathbf{k-q}} - n_{c,\mathbf{k}}}{\hbar(\omega + i\delta) + \epsilon_{c,\mathbf{k-q}} - \epsilon_{c,\mathbf{k}}} , \tag{A.14}$$

where $c = e, lh$ and hh.

In Eq. (A.13) or Eq. (A.14) one sees that the Lindhard formula exhibits a continuum of poles which makes the numerical evaluation of the screened Coulomb potential from the Lindhard formula rather difficult. To avoid such difficulties, it is possible to modify this formula using appropriate approximations.

A.2 The static plasmon-pole approximation

A.2.1 The long wavelength limit

To simplify the Lindhard formula we explore first the long wavelength limit: $q \to 0$. We expand the terms in Eq. (A.13) which are functions of q dropping the higher-order corrections. Then, letting $\delta \to 0$, the denominator and numerator in Eq. (A.13) become:

$$\epsilon_{\mathbf{k-q}} - \epsilon_{\mathbf{k}} = \frac{\hbar^2}{2m} (k^2 - 2\mathbf{k}.\mathbf{q} + q^2) - \frac{\hbar^2 k^2}{2m} \simeq - \frac{\hbar^2 \mathbf{k}.\mathbf{q}}{m} , \tag{A.15}$$

and

$$n_{\mathbf{k-q}} - n_{\mathbf{k}} = n_{\mathbf{k}} - \mathbf{q}.\nabla_{\mathbf{k}} n_{\mathbf{k}} + \cdots - n_{\mathbf{k}} \simeq - \mathbf{q}.\nabla_{\mathbf{k}} n_{\mathbf{k}} . \tag{A.16}$$

Then inserting Eqs. (A.15) and (A.16) in Eq. (A.14) leads to:

$$\epsilon(q \to 0, \omega) = 1 + V_q \sum_{\mathbf{k}} \sum_{i} \frac{q_i \dfrac{\partial n}{\partial k_i}}{\hbar\omega - \dfrac{\hbar^2}{m} \mathbf{k}.\mathbf{q}} . \tag{A.17}$$

We can further simplify the above expression, noting that in the limit $q \to 0$,

[1] In this work we deal with both light and heavy holes

the denominator can also be expanded to the first order:

$$\epsilon(q \to 0, \omega) = 1 + \frac{V_q}{\hbar\omega} \sum_{\mathbf{k}} \sum_i \; q_i \; \frac{\partial n}{\partial k_i} \left(1 + \; \frac{\hbar}{m\omega} \; \mathbf{k}.\mathbf{q} \right) \; . \tag{A.18}$$

The term proportional to $\sum \partial n/\partial k$ vanishes because it yields the distribution function for $k \to \infty$; so Eq. (A.18) becomes:

$$\epsilon(q \to 0, \omega) = 1 + \frac{V_q}{m\omega^2} \sum_{\mathbf{k}} \sum_i \; q_i \; \frac{\partial n}{\partial k_i} \; \mathbf{k}.\mathbf{q} \; . \tag{A.19}$$

Replacing the discrete sum $\sum_{\mathbf{k}}$ by a 2D integral and integrating by parts yields:

$$\epsilon(q \to 0, \omega) = 1 - \frac{V_q}{m\omega^2} \sum_i \sum_j \; q_i q_j \; \int \frac{d^2k}{4\pi^2} \; n_{\mathbf{k}} \frac{\partial k_i}{\partial k_j} \; , \tag{A.20}$$

which simply gives:

$$\epsilon(q \to 0, \omega) = 1 - \frac{V_q}{m\omega^2} \sum_i \sum_j \; q_i q_j \; N\delta_{i,j} \; , \tag{A.21}$$

where N is the 2D electron density. Performing the sums over i and j leads to:

$$\epsilon(q \to 0, \omega) = 1 - V_q \; \frac{q^2}{m\omega^2} \; N \; , \tag{A.22}$$

thanks to the Kronecker symbol $\delta_{i,j}$. Eq. (A.22) is nothing else but the classical Drude dielectric function:

$$\epsilon(q \to 0, \omega) = 1 - \frac{\omega_{pl}^2}{\omega^2} \; , \tag{A.23}$$

where the plasma frequency is defined as in Eq. (2.12)

A.2.2 The static plasmon-pole approximation

For many practical applications, one ignores the damped response of the screening represented by $\omega + i\delta$ in Eq. (A.13). In the long wavelength limit, the inverse dielectric function can be written as

$$\epsilon(q \to 0, \omega)^{-1} = 1 + \frac{\omega_{pl}^2}{(\omega + i\delta)^2 - \omega_{pl}^2} \ . \tag{A.24}$$

The above expression exhibits just one pole. We can use this observation to construct an approximation for the full RPA dielectric function $\epsilon_q(\omega)$ which replaces the continuum of poles contained in the Lindhard formula by one effective plasmon pole at ω_q:

$$\epsilon(q \to 0, \omega)^{-1} = 1 + \frac{\omega_{pl}^2}{(\omega + i\delta)^2 - \omega_q^2} \ . \tag{A.25}$$

The effective plasmon frequency for a two-dimensional electron gas is:

$$\omega_q^2 = \omega_{pl}^2(q) \left(1 + \frac{q}{\kappa}\right) \ + \nu_q^2, \tag{A.26}$$

where κ and ν_q are defined as in chapter 2, section 2.2.1. In the static limit $\omega + i\delta \to 0$, the above expression simply becomes:

$$\epsilon(q \to 0, \omega)^{-1} = 1 - \frac{\omega_{pl}^2}{\omega_q^2} \ . \tag{A.27}$$

Practical applications show that it is often sufficient to use the much simpler plasmon-pole approximation instead of the full RPA dielectric function to obtain good qualitative results. Finally, generalization of the above formulas to a multi-component plasma can be easily obtained as seen in chapters 2 and 3.

Appendix B

The form factor

In chapter 2, section 2, we saw that the Coulomb potential in a quantum well is not purely two-dimensional because of the finite well width. Therefore, to account for the finite carrier wavefunction extent in the growth direction, we introduce a quasi-two-dimensional effective Coulomb potential defined as:

$$V(\mathbf{r}_{||}) = \frac{-e^2}{4\pi\epsilon} \int_0^w dz \int_0^w dz' \, \frac{|u_n(z)|^2 |u_n(z')|^2}{\sqrt{(z-z')^2 + \mathbf{r}_{||}^2}} \, , \tag{B.1}$$

where $u(z)$ is the envelope function of an infinitely deep well extended from 0 to w:

$$u_n(z) = \sqrt{\frac{2}{w}} \, \sin\left(\frac{n\pi z}{w}\right) \tag{B.2}$$

The wavefunction $u(z)$ can be calculated from the Schrödinger equation given in Eq. (2.18) with an infinite confinement potential. Performing the 2D Fourier transform of Eq. (B.1) leads to:

$$V_{\mathbf{k}_{||},\mathbf{k'}_{||}} = \frac{-e^2}{2\epsilon|\mathbf{k}_{||} - \mathbf{k'}_{||}|} \int_0^w dz \int_0^w dz' \, |u_n(z)|^2 |u_n(z')|^2 \, e^{-|\mathbf{k}_{||} - \mathbf{k'}_{||}||z-z'|} \, . \tag{B.3}$$

Defining the wavevector $\mathbf{q}$ as $\mathbf{q} = \mathbf{k}_{||} - \mathbf{k'}_{||}$, Eq. (B.3) can be rewritten as follows:

$$V_{\mathbf{q}} = f_q \, V_{\mathbf{q}}^{2D} \, , \tag{B.4}$$

f_q being the form factor defined as:

$$f_q = \int_{-\infty}^{\infty} dz \int_{-\infty}^{\infty} dz' |u_n(z)|^2 |u_n(z')|^2 \, e^{q|z-z'|} \, , \tag{B.5}$$

Using the above definition for the function $u_n(z)$ is a good approximation which

makes the computation of f_q easier; indeed, choosing the eigenfunctions for a finite well depth to define $u_n(z)$ leads to complications which have no significant effect on the final result [44].

By inserting Eq. (B.2) into Eq. (B.5) one obtains:

$$f_q = \frac{4}{w^2} \int_0^w dz \ \sin^2\left(\frac{n\pi z}{w}\right) \ F(z) \ , \tag{B.6}$$

with

$$F(z) = q^{-qz} \int_0^z \ \sin^2\left(\frac{n\pi z'}{w}\right) \ e^{qz'} + \int_z^w \ \sin^2\left(\frac{n\pi z'}{w}\right) \ e^{-qz'} \ dz'. \tag{B.7}$$

The calculation of the integrals gives:

$$F(z) = \frac{1}{q} - \frac{qw^2}{q^2w^2 + 4n^2\pi^2} \ \cos\left(\frac{2\pi n z'}{w}\right) - \frac{q}{2}\left(\frac{1}{q^2} - \frac{w^2}{q^2w^2 + 4n^2\pi^2}\right) \ (e^{-qz} + e^{-q|w-z|}) \ . \tag{B.8}$$

Inserting Eq. (B.8) into Eq. (B.6) and performing the integration leads to:

$$f_q = \frac{2}{w} \ \left[\frac{1}{q} + \frac{1}{2} \ \frac{qw^2}{q^2w^2 + 4n^2\pi^2} + (e^{-qw} - 1)\frac{1}{w}\left(\frac{1}{q} - \frac{qw^2}{q^2w^2 + 4n^2\pi^2}\right)^2\right] \ . \tag{B.9}$$

Appendix C

Numerical evaluation of the Coulomb matrix elements

In chapter 3, the main difficulty of the numerical problem is the evaluation of the sum over the vectors $\mathbf{q}$ of the angle averaged potential

$$V^*(k,q) = \frac{e^2}{8\pi^2\epsilon}\, q \int_0^{2\pi} \frac{d\theta}{\sqrt{k^2+q^2-2kq\cos\theta}}\ , \tag{C.1}$$

at zero and low density as $V^*(k,q)$ becomes singular for $\mathbf{q}=\mathbf{k}$. This singularity has to be removed before leading further the calculations, but considerable care must be taken when integrating in the vincinity of the singularity. As already stated in chapter 3, a way to overcome this problem without wasting computing time using a dense mesh for the numerical integration, is to evaluate the difference between calculations which would be done with a dense mesh and calculations which would be done with a coarse mesh. This difference is regarded as the correction that has to be added to the result of the integration performed with a coarse mesh. The calculation of the correction is not very time consuming. This can only be done if $V^*(k,q)$ is a slow enough varying function far from the singularity. The function $V^*(k,q)$ is depicted on Fig. 3.1 which shows that its behaviour is suitable for the simple treatment of the numerical problem that follows.

We use the trapezoidal rule for the integration of $V^*(k,q)$. The k-vectors on the uniform coarse mesh are defined by the array whose components are k_i with $i = 0, 1, \ldots n_c - 1$. The lower and upper limits are $k_{min} = 0$ and $k_{max} = \sqrt{\mu_{eh}(\hbar\omega_{max} - E_g)}/\hbar$, where μ_{eh} is the reduced mass of the electron/hole system. The step dk is defined as $dk = (k_{max} - k_{min})/n_c$. The uniform dense mesh is defined as follows: between two consecutives k-points k_{i+1} and k_i, there are n_d k'-points

equally spaced, the step being $dk' = dk/(n_d - 1)$.

For a given value of q, the difference between the areas below the singular point $k[j] = q$, $\mathcal{A}_d^j$ and $\mathcal{A}_c^j$, evaluated with the trapezoidal rule on the dense and coarse meshes is:

$$\mathcal{A}_d^j - \mathcal{A}_c^j = X_j = dk' \sum_{l=1}^{n_d-2} k'_l \; V^*(k_j, k'_l) \; F(k_j, k'_l)$$

$$+\frac{dk'}{2} \; \left[k'_{l=0} V^*(k_j, k'_{l=0}) \; F(k_j, k'_{l=0}) + k'_{l=n_d-1} V^*(k_j, k'_{l=n_d-1}) \; F(k_j, k'_{l=n_d-1})\right]$$

$$-\frac{dk}{2} \; [k_{i=j-1} V^*(k_{i=j-1}, k_j) \; F(k_{i=j-1}, k_j) + k_{i=j+1} V^*(k_{i=j+1}, k_j) \; F_1(k_{i=j+1}, k_j)] \tag{C.2}$$

after removing the divergent contribution, $V^*(k_j, k_j)$. The function $F(k, q)$ is a smoothing function, chosen such that $F(k, k) = 1$ and that $\sum_q F(k, q) \; V^*(k, q)$ can be evaluated analytically. For our problem we take:

$$F(k, q) = \frac{4q^4}{(k^2 + q^2)^2} \; . \tag{C.3}$$

As stated before: far from the singularity, the difference between the areas calculated with the dense and coarse meshes is negligible. So, we just have to calculate the difference between the areas $\mathcal{A}_d^j$ and $\mathcal{A}_c^j$ between k_{j-1} and k_{j+1}, which is not very time consuming. To proceed with the calculations, we note that $k'_{l=0} = k_{i=j-1}$ and $k'_{l=n_d-1} = k_{i=j+1}$, so X_j can be rewritten as follows:

$$X_j = dk' \sum_{l=1}^{n_d-2} k'_l \; V^*(k_j, k'_l) \; F(k_j, k'_l)$$

$$+\frac{1}{2} \, (dk' - dk) \, [k_{i=j-1} V(k_{i=j-1}, k_j) \; F(k_{i=j-1}, k_j) + k_{i=j+1} V^*(k_{i=j+1}, k_j) \; F(k_{i=j+1}, k_j)] \, . \tag{C.4}$$

For $j = 1, \ldots, n_c - 2$, X_j is calculated, and we just have to add it to the result obtained integrating $V^*(k, q)$ using a coarse mesh.

Appendix D

Spontaneous emission and radiative lifetime in semiconductors

When atoms in a gas are excited, they can de-excite thanks to inelastic collisions. However, it is possible to observe that even in a very low pressured gas, where inelastic collisions are very unlikely, atoms de-excite in a very little time ($\sim \mu s$) compared to the scattering time of these dilute atoms. It is in fact an apparent paradox, and we can show that if we quantize both the energy levels of a system and the electromagnetic field it interacts with, the concept of spontaneous emission arises naturally. In this Appendix, we show derivations made for a two-level system which illustrates in a simple way the physics of the spontaneous emission phenomenon. This is not only convenient to avoid unecessary complicated calculations, but the results can be applied within the two-band model used in chapter 6.

The interaction Hamiltonian including the quantized electric field corresponding to the mode l has the following expression:

$$\widehat{W} = iq\mathcal{F}_l \left(\hat{a}_l e^{i\mathbf{k}_n \cdot \mathbf{r}} - \hat{a}_l^\dagger e^{-i\mathbf{k}_n \cdot \mathbf{r}} \right) \vec{\epsilon}_l \cdot \hat{\mathbf{r}} \ , \tag{D.1}$$

where $\hat{a}_l$ and $\hat{a}_l^\dagger$ are the annihilation and creation operators of photons in the mode l, $\vec{\epsilon}$ the polarization of the electric field. The quantity $\mathcal{F}_l$ is the vacuum fluctuation field of the mode l in a cavity with a volume V, given by:

$$\mathcal{F}_l = \sqrt{\frac{\hbar\Omega_l}{2\epsilon_0 V}} \ . \tag{D.2}$$

The Hamiltonian $\widehat{W}$ acts in the Hilbert space given by the tensorial product of the two Hilbert spaces corresponding to the photons and the charged system. To ease notations (and calculations), we consider just a single mode. Thus, we assume

that we have an optical transition between the two states $|1,n\rangle$ and $|2,n'\rangle$ where n and n' are the number of photons, and 1 and 2 the two levels of the quantum system.

We study the absorption mechanisms first. The initial state is described by $|1,n\rangle$ and the final state by $|2,n-1\rangle$. Fermi's golden rule gives the probability of absorption:

$$P_{1,2} = \frac{2\pi}{\hbar}\ |\langle 1,n|\widehat{W}|2,n-1\rangle|^2\ \delta(E_{final} - E_{initial})\ , \tag{D.3}$$

where

$$\begin{cases} E_{initial} = E_1 + \hbar\Omega(n + 1/2) \\ E_{final} = E_2 + \hbar\Omega\left((n-1) + 1/2\right) \end{cases} \tag{D.4}$$

Thus, the condition on conservation of energy is $\hbar\Omega = E_2 - E_1$. Considering Eq. (D.1), Eq. (D.3) can then be written as follows:

$$P_{1,2} = \frac{2\pi}{\hbar}\ q^2\mathcal{F}_l^2|\langle 1,n|\left(\hat{a}_l e^{i\mathbf{k}_n.\mathbf{r}} - \hat{a}_l^\dagger e^{-i\mathbf{k}_n.\mathbf{r}}\right)\vec{\epsilon}_l.\hat{\mathbf{r}}|2,n-1\rangle|^2\delta(\hbar\Omega - E_2 + E_1)\ . \tag{D.5}$$

As we suppose that the photonic states are independent of the states of the system, we can write Eq. (D.5) as follows:

$$P_{1,2} = \frac{2\pi}{\hbar}\ q^2\mathcal{F}_l^2|\langle n-1|\left(\hat{a}_l e^{i\mathbf{k}_n.\mathbf{r}} - \hat{a}_l^\dagger e^{-i\mathbf{k}_n.\mathbf{r}}\right)|n\rangle|^2|\langle 1|\vec{\epsilon}_l.\hat{\mathbf{r}}|2\rangle|^2\delta(\hbar\Omega - E_2 + E_1)\ . \tag{D.6}$$

As the annihilation operator has the following property: $\hat{a}|n\rangle = \sqrt{n}|n-1\rangle$, the only photonic term remaining from the above equation is n, and the probability of absorption becomes:

$$P_{1,2} = \frac{\pi}{\hbar}\ \frac{\hbar\Omega_l n}{\epsilon_0 V}\ |\langle 1|q\vec{\epsilon}_l.\hat{\mathbf{r}}|2\rangle|^2\ \delta(\hbar\Omega - E_2 + E_1)\ , \tag{D.7}$$

after having substituted for $\mathcal{F}_l$.

we consider now n photons in the mode l, but the initial state defined as the state $|2\rangle$. The emission is described as the transition from the state $|2,n\rangle$ to the state $|1,n+1\rangle$ and the transition probability is given by:

$$P_{1,2} = \frac{2\pi}{\hbar}\, q^2\mathcal{F}_l^2 |\langle n+1| \left(\hat{a}_l e^{i\mathbf{k}_n.\mathbf{r}} - \hat{a}_l^\dagger e^{-i\mathbf{k}_n.\mathbf{r}}\right)|n\rangle|^2 |\langle 1|\vec{\epsilon}_l.\hat{\mathbf{r}}|2\rangle|^2 \delta(\hbar\Omega - E_2 + E_1)\ . \quad \text{(D.8)}$$

This time, the only non zero photonic term is $n+1$ as we have $\hat{a}^\dagger|n\rangle = \sqrt{n+1}|n\rangle$, thus Eq.(D.8) leads to:

$$P_{em} = \frac{\pi\omega_l}{\epsilon_0 V}(n+1)|\langle 1|q\vec{\epsilon}_l.\hat{\mathbf{r}}|2\rangle|^2 \delta(\hbar\Omega - E_2 + E_1)\ . \quad \text{(D.9)}$$

The above equation is important because it shows that we deal with two distinct physical processes which both contribute to the emission:

1. an emission mechanism which transition rate P_{stim} is proportional to the number of photons present in the cavity: it is the *stimulated emission*.

2. an emission mechanism which exists even if the cavity is empty of any photon: it is the *spontaneous emission*.

The spontaneous emission rate in the mode l, P^l_{spon} is given by:

$$P^l_{spon} = \frac{\pi\Omega_l}{\epsilon_0 V}\ |\langle 1|q\vec{\epsilon}_l.\hat{\mathbf{r}}|2\rangle|^2 \delta(\hbar\omega - E_2 + E_1)\ . \quad \text{(D.10)}$$

It is also possible to interprete this term as an emission rate due to a stimulation because of the vacuum fluctuation $\mathcal{F}_l$. Under the influence of this vacuum fluctuation, the system can de-excite emiting a photon in a certain mode. The total rate of the spontaneous emission can be obtained with an integration over all the modes of the cavity with a frequency equal to $\Omega = (E_2 - E_1)/\hbar$:

$$\Gamma_{spon} = \iiint P^{l}_{spon} d^3\mathbf{k} \tag{D.11}$$

We can use the expression of the electromagnetic modes density:

$$\rho(\Omega) = \frac{2\Omega^2}{\pi c^3} \ , \tag{D.12}$$

to obtain the following expression of the spontaneous emission rate and the lifetime for a two-level system:

$$\Gamma_{spon} = \frac{q^2 r_{12}^2 \Omega^3 n_{op}}{3\pi c^3 \hbar \epsilon_0} = \frac{1}{\tau_{rad}} \ . \tag{D.13}$$

Let us emphasise on the fact that this expression is valid for an isotropic emission. Also note that for a constant dipole matrix element, the higher the energy transition is, the shorter the spontaneous lifetime is. This gives the reason why it is more difficult to obtain X-ray lasers rather than infrared lasers.

Appendix E

Calculation of the exciton and free electron distributions

In chapter 6, section 4, we need the knowledge of the $1s$ exciton and electron distributions, $N_{\mathbf{K}}$ and $N_{\mathbf{k}_2}$.

- The electron distribution

Keeping the same notations as in chapter 5, the probability of finding a free electron in the electron-hole plasma with energy $E_{k_2} = \hbar^2 k_2^2/2m_e$ is:

$$N_{\mathbf{k}_2} = \gamma\ \alpha\mathcal{N}\ \exp - \left[\beta\ \frac{\hbar^2 k_2^2}{2m_e}\ - \beta\mu_e\right]\ , \tag{E.1}$$

where $\alpha\mathcal{N}$ is the total number of free electrons, according to the definition of the degree of ionization α in Eq. (6.15). The normalization coefficient γ is evaluated from the following equation:

$$\sum_{\mathbf{k}_2} N_{\mathbf{k}_2} = \alpha\mathcal{N}\ . \tag{E.2}$$

Inserting Eq. (E.1) into Eq. (E.2) and approximating the discrete sum by a 2D integral yield:

$$\gamma\ e^{\beta\mu_e}\ \sum_{\mathbf{k}_2} \exp - \left(\beta\ \frac{\hbar^2 k_2^2}{2m_e}\right) = \frac{\mathcal{A}}{4\pi^2}\ \gamma\ e^{\beta\mu_e}\ \int_0^\infty\!\!\int_0^{2\pi} k_2\ \exp - \left[\beta\ \frac{\hbar^2 k_2^2}{2m_e}\right] dk_2\ d\theta = 1\ . \tag{E.3}$$

Performing the integration and rearranging the result give the normalization coefficient γ:

$$\gamma = \frac{2\pi\beta\hbar^2}{\mathcal{A}m_e}\, e^{-\beta\mu_e} \ . \tag{E.4}$$

Finally the electron distribution $N_{\mathbf{k}_2}$ is given by:

$$N_{\mathbf{k}_2} = \frac{2\pi\beta\hbar^2}{m_e}\, \alpha N\ \exp\left(-\beta\ \frac{\hbar^2 k_2^2}{2m_e}\right)\ , \tag{E.5}$$

N being the total electron density: $N = \mathcal{N}/\mathcal{A}$.

- The $1s$ exciton distribution

The total number of excitons in the electron-hole plasma is given by:

$$\sum_{\mathbf{K}} N_{\mathbf{K}} = (1-\alpha)\mathcal{N} = \sum_{\mathbf{K}} \gamma'(1-\alpha)\mathcal{N}\ \exp\left(-\beta\ \frac{\hbar^2 K^2}{2M}\right)\ . \tag{E.6}$$

In the same fashion as above we find:

$$\gamma' = \frac{2\pi\beta\hbar^2}{\mathcal{A}M}\ . \tag{E.7}$$

The exciton distribution reads:

$$N_{\mathbf{K}} = \frac{2\pi\beta\hbar^2}{M}\ (1-\alpha)N\ \exp\left(-\beta\ \frac{\hbar^2 K^2}{2M}\right)\ . \tag{E.8}$$

The degree of ionization α takes into account any type of correlation in the electron hole plasma. However, we make the simplifying assumption that the correlations are essentially excitonic at room temperature and that this is the $1s$ exciton population which is dominant in quasi-equilibrium.

Publications

1. H. Ouerdane, G. Papageorgiou, I. Galbraith, A.K. Kar and B.S. Wherrett. 'Ultrafast pump-probe dynamics in ZnSe-based semiconductor quantum-wells'. Submitted to Journal of the Optical Society of America B.

2. H. Ouerdane, I. Galbraith and M.E. Portnoi. 'Exciton-electron scattering in quantum wells'. In preparation for Physical Review B.

Bibliography

[1] R. Zimmermann. *Many-Particle Theory of Highly Excited Semiconductors*. Teubner, Berlin, 1988.

[2] K. Leo, M. Wegener, J. Shah, D. S. Chemla, E. O. Gbel, and T. C. Damen. *Phys. Rev. Lett* **65**, 1340 (1990).

[3] D. Kim, J. Shah, T. C. Damen, W. Schfer, F. Jahnke, S. Schmitt-Rink, and K. Köhler. *Phys. Rev. Lett* **69**, 2725 (1992).

[4] S. Weiss, M.-A. Mycek, J.-Y. Bigot, S. Schmitt-Rink, and D. S. Chemla. *Phys. Rev. Lett* **69**, 2685 (1992).

[5] H. Haug and A. P. Jauho. *Quantum Kinetics in Transport and Optics of Semiconductors*. Springer, Berlin, 1996.

[6] J. Shah, editor. *Hot Carriers in Semiconductors Nanostructures: Physics and Applications*. Academic Press, San Diego, 1992.

[7] D. S. Chemla and J. Shah. *Nature* **411**, 549 (2001).

[8] N. Peyghambarian, H. M. Gibbs, J. L. Jewell, A. Antonetti, A. Migus, D. Hulin, and A. Mysyrowicz. *Phys. Rev. Lett.* **53**, 2433 (1984).

[9] W. H. Knox, R. L. Fork, M. C. Downer, D. A. B. Miller, D. S. Chemla, C. V. Shank, A. C. Gossard, and W. Wiegmann. *Phys. Rev. Lett.* **54**, 1306 (1985).

[10] K. H. Schlaad, C. Weber, J. Cunningham, C. V. Hoof, G. Borghs, G. Weimann, W. Schlapp, H. Nickel, and C. Klingshirn. *Phys. Rev.* **B43**, 4268 (1991).

[11] H. Haug and S. W. Koch. *Quantum Theory of the Optial and Electronic Properties of Semiconductors*. World Scientific Publishing, Singapore, 1993.

[12] C. F. Klingshirn. *Semiconductor Optics*. Springer-Verlag, Berlin Heidelberg, 1997.

[13] M. Lindberg and S. Koch. *Phys. Rev.* **B38**, 3342 (1988).

[14] S. Schmitt-Rink, D. S. Chemla, and H. Haug. *Phys. Rev.* **B37**, 941 (1988).

[15] I. Balslev and A. Stahl. *Opt. Comm.* **65**, 137 (1988).

[16] I. Balslev, R. Zimmermann, and A. Stahl. *Phys. Rev.* **B40**, 4095 (1989).

[17] L. Allen and J. H. Eberly. *Optical Resonance and Two-level Atoms*. Wiley and Sons, New York, 1975.

[18] P. Meystre and M. S. III. *Elements of Quantum Optics*. Springer, Berlin, 1990.

[19] M. S. III, M. O. Scully, and W. E. Lamb. *Laser Physics*. Addison Wesley, New York, 1974.

[20] M. Joffre, D. Hulin, J. P. Foing, J. P. Chambaret, A. Migus, and A. Antonetti. *IEEE J. Quantum Electron.* **25**, 2505 (1989).

[21] A. N. D. Fröhlich and K. Reimann. *Phys. Rev. Lett.* **55**, 1335 (1985).

[22] A. Mysyrowicz, D. Hulin, A. Antonetti, A. Migus, W. T. Masselink, and H. Morkoc. *Phys. Rev. Lett.* **56**, 2748 (1986).

[23] A. von Lehmen, J. E. Zucker, J. P. Heritage, and D. S. Chemla. *Optics Lett.* **11**, 609 (1986).

[24] B. Fluegel, N. Peyghambarian, G. Olbright, M. Lindberg, S. W. Koch, M. Joffre, D. Hulin, A. Migus, and A. Antonetti. *Phys. Rev. Lett.* **59**, 2588 (1987).

[25] S. W. Koch, N. Peyghambarian, and M. Lindberg. *J. Phys.* **C21**, 5229 (1988).

[26] C. Ell, J. F. Müller, K. E. Sayed, and H. Haug. *Phys. Rev. Lett.* **62**, 306 (1989).

[27] M. Combescot and R. Combescot. *Phys. Rev.* **B40**, 3788 (1989).

[28] M. Combescot. *Phys. Rev.* **B41**, 3517 (1990).

[29] M. Combescot and R. Combescot. *Phys. Rev. Lett.* **61**, 117 (1988).

[30] D. Hulin and M. Joffre. *Phys. Rev. Lett.* **65**, 3425 (1990).

[31] C. Sieh, T. Meier, F. Jahnke, A. Knorr, S. W. Koch, P. Brick, M. Hübner, C. Ell, J. Prineas, G. Khitrova, and H. M. Gibbs. *Phys. Rev. Lett.* **82**, 3112 (1999).

[32] G. Brown, I. J. Blewett, I. Galbraith, A. K. Kar, and B. S. Wherrett. *Phys. Rev.* **B63**, 08201(R) (2001).

[33] C. Sieh, T. Meier, A. Knorr, F. Jahnke, P. Thomas, and S. W. Koch. *Eur. Phys. J.* **B11**, 407 (1999).

[34] T. Meier and S. W. Koch. *Phys. Rev.* **B59**, 13202 (1999).

[35] V. M. Axt, K. Victor, and A. Stahl. *Phys. Rev.* **B53**, 7244 (1994).

[36] G. Bartels, G. C. Cho, T. Dekorsy, H. Kurz, A. Stahl, and K. Köhler. *Phys. Rev.* **B55**, 16404 (1997).

[37] V. M. Axt and A. Stahl. *Z. Phys.* **B93**, 195 (1996).

[38] V. M. Axt and A. Stahl. *Z. Phys.* **B93**, 205 (1996).

[39] M. J. Snelling, P. Perozzo, D. C. Hutchings, I. Galbraith, and A. Miller. *Phys. Rev.* **B49**, 17160 (1994).

[40] C. H. Henry, R. A. Logan, and F. R. Merrit. *Journal of Applied Physics* **51**(6), 3042 (1980).

[41] P. Blood, A. I. Kucharska, J. P. Jacobs, and K. Griffiths. *Journal of Applied Physics* **70**(3), 1144 (1991).

[42] C. Ell, R. Blank, S. Benner, and H. Haug. *J. Opt. Soc. Am* **B6**, 2006 (1989).

[43] O. Madelung, editor. *Semiconductors - Basic Data.* Springer, 1992.

[44] W. W. Chow and S. W. Koch. *Semiconductor-Laser Fundamentals.* Springer-Verlag, Berlin, 1999.

[45] B. I. Lundquist. *Phys. Konden. Mat.* **6**, 193 and 206 (1967).

[46] H. Haug and S. Schmitt-Rink. *Prog. Quantum Electron.* **9**, 3 (1984).

[47] R. Binder, D. Scott, A. E. Paul, M. Lindberg, K. Henneberger, and S. W. Koch. *Phys. Rev.* **B45**, 1107 (1992).

[48] K. E. Sayed, T. Wicht, H. Haug, and L. Bányai. *Z. Physik* **B86**, 345 (1992).

[49] D. C. Scott, R. Binder, and S. W. Koch. *Phys. Rev. Lett* **69**, 347 (1992).

[50] F. Jahnke and S. W. Koch. *Appl. Phys. Lett.* **67**, 2278 (1995).

[51] F. Jahnke and S. W. Koch. *Phys. Rev.* **A52**, 1712 (1995).

[52] E. O. Kane. *J. Phys. Chem.* **1**, 249 (1957).

[53] J. M. Luttinger and M. Kohn. *Phys. Rev.* **97**, 869 (1955).

[54] J. M. Luttinger. *Phys. Rev.* **102**, 1030 (1956).

[55] W. W. Chow, S. W. Koch, and M. S. III. *Semiconductor-Laser Fundamentals*. Springer-Verlag, Berlin, 1997.

[56] H. M. Gibbs. *Optical Bistability: Controlling Light With Light*. Academic Press, 1985.

[57] R. J. Elliott. *Phys. Rev.* **96**, 266 (1954).

[58] Y. Yafet. *Solid State Physics*. Academic Press, New York, 1963.

[59] M. I. D'Yakonov and V. I. Perel. *Sov. Phys. JETP* **33**, 1053 (1971).

[60] T. C. Damen, L. Vina, J. E. Cunningham, and J. Shah. *Phys. Rev. Lett.* **67**, 3432 (1991).

[61] R. Ferreira and G. Bastard. *Phys. Rev.* **B43**, 9687 (1991).

[62] J. M. Kikkawa, I. P. Smorchkova, N. Samarth, and D. D. Awschalom. *Science* **277**, 1284 (1997).

[63] T. Amand, X. Marie, P. L. Jeune, M. Brousseau, D. Robart, J. Barrau, and R.Planel. *Phys. Rev. Lett.* **78**, 1355 (1997).

[64] J. M. Kikkawa and D. D. Awschalom. *Phys. Rev. Lett.* **80**, 4313 (1998).

[65] M. Potemski, E. Pérez, D. Martin, L. Vina, L. Gravier, A. Fisher, and K. Ploog. *Sol. State Com.* **110**, 163 (1999).

[66] J. Fabison and S. D. Sarma. *J. Vac. Sci. Technol.* **B17**, 1708 (1999).

[67] Y. Ohno, R. Terauchi, T. Adachi, F. Matsukura, and H. Ohno. *Phys. Rev. Lett.* **83**, 4196 (1999).

[68] I. V. Kukushkin, K. von Klitzing, K. Ploog, and V. B. Timofeev. *Phys. Rev.* **B40**, 7788 (1989).

[69] J. P. Bergman, Q. X. Zhao, P. O. Holtz, B. Monemar, M. Sundaram, J. L. Merz, and A. C. Gossard. *Phys. Rev.* **B43**, 4771 (1991).

[70] M. Kira, F. Jahnke, W. Hoyer, and S. W. Koch. *Prog. in Quantum Electron.* **23**, 189 (1999).

[71] E. Rosencher and B. Vinter. *Optoélectronique.* Thomson-CSF and Masson, Paris, 1998.

[72] H. W. Liu, C. Delalande, G. Bastard, M. Voos, G. Peter, R. Fischer, E. O. Göbel, J. A. Brum, G. Weimann, and W. Schlapp. *Phys. Rev.* **B39**, 13537 (1989).

[73] M. Gurioli, A. Vinattieri, M. Colocci, C. Deparis, J. Massies, G. Neu, A. Bosacchi, and S. Franchi. *Phys. Rev.* **B44**, 3115 (1991).

[74] A. Fujiwara, K. Muraki, S. Fukatsu, Y. Shiraki, and R. Ito. *Phys. Rev.* **B51**, 14324 (1995).

[75] A. Hangleiter and R. Häcker. *Phys. Rev. Lett.* **65**, 215 (1990).

[76] G. Bastard. *Wave Mechanics Applied to Semiconductor Heterostructures*. Les éditions de Physique, 1988.

[77] S. Taniguchi, T. Hino, S. Itoh, K. Nakano, A. Ishibashi, and M. Ikeda. *Electronics Letters* **32**, 552 (1996).

[78] S. Nakamura, M. Senoh, S. Nagahama, N. Iwasa, T. Yamada, T. Matsushita, and Y. Kiyoku. *Applied Physics Letters* **70**, 1417 (1997).

[79] E. Hanamura and H.Haug. *Physics Reports* **33C**, 209 (1977).

[80] M. Lindberg, Y. Z. Hu, R. Binder, and S. W. Koch. *Physical Review B* **50**, 18060 (1994).

[81] M. F. Pereira and K. Henneberger. *Physical Review B* , 2064 (1998).

[82] M. E. Portnoi and I. Galbraith. *Journal of Crystal Growth* **184/185**, 676 (1998).

[83] M. E. Portnoi and I. Galbraith. *Physical Review* **B60**, 5570 (1999).

[84] R. Zimmermann and H. Stolz. *Physica Status Solidi B* **131**, 151 (1985).

[85] F. Stern and W. E. Howard. *Physical Review* **163**, 816 (1967).

[86] I. S. Gradshteyn and I. M. Ryzhik. *Table of Integrals, Series, and Products*. Academic Press, New York, 1980.

[87] M. Abramovitz and I. A. Stegun. *Handbook of Mathematical Functions*. Dover Publication, New York, 1972.

[88] G. W. Fehrenbach, W. Schäfer, J. Treusch, and R. G. Ulbrich. *Physical Review Letters* **49**(17), 1281–1284 (Oct. 1982).

[89] F. Jahnke, M. Kira, S. W. Koch, G. Khitrova, E. K. Lindmark, T. R. N. Jr, D. V. Wick, J. D. Berger, O. Lyngnes, and H. M. Gibbs. *Physical Review Letters* **77**(26), 5257–5260 (Dec. 1996).

[90] I. Galbraith and S. W. Koch. *Journal of Crystal Growth* **159**, 667 (1996).

[91] C. B. à la Guillaume, J. M. Debever, and F. Salvan. *Phys. Rev.* **177**, 567 (1969).

[92] S. W. Koch. Zur Theorie der Stimulierten Emission in Dichten Exzitonensystemen. *Diploma thesis, J. W. Goethe University, Frankfurt, Germany* .

[93] S. W. Koch, H. Haug, G. Schmeider, W. Bohnert, and C. Klingshirn. *Phys. Status Solidi (b)* **89**, 431 (1978).

[94] H. Haug and S. W. Koch. *Phys. Status Solidi (b)* **82**, 531 (1977).

[95] H. Haug. *J. Appl. Phys.* **39**, 4687 (1968).

[96] M. E. Portnoi and I. Galbraith. *Solid State Communications* **103**(6), 325 (1997).

[97] M. E. Portnoi and I. Galbraith. *Physical Review* **B58**, 3963 (1998).

[98] E. Beth and G. E. Uhlenbeck. *Physica (Amsterdam)* **4**, 915 (1937).

[99] J. Lee, H. N. Spector, and P. Melman. *Journal of Applied Physics* **58**, 1893 (1985).